Unveiling dust and gas in Lyman–α emitters across cosmic time

Rahul Rana

Physics
Department of Physics
Lancaster University

September 8, 2025

A thesis submitted to Lancaster University for the degree of Doctor of Philosophy in the Faculty of Science and Technology

Supervised by Dr Julie Wardlow

Abstract

To understand the complete picture of galaxy evolution, it is important to investigate the total star formation, interstellar medium (ISM) conditions, and gas reservoirs of early galaxies. Since dust can absorb and scatter UV and optical light, it can heavily obscure regions of active star formation. This makes UV/optical measurements incomplete and they require corrections or alternative observations to reveal hidden star-forming activity. Furthermore, early galaxies are expected to be rich in gas, but estimating the amount of molecular hydrogen in these distant galaxies remains challenging due to the difficulty in detecting faint hydrogen tracers at high redshift. As a result, understanding the full picture of star formation and gas content in the early Universe requires alternative observations. In this thesis, we use far-infrared data to investigate the dust and gas content of early, star-forming galaxies selected from their Lyα emission, known as Lyα emitters (LAEs). Analysing the dust and gas emission enables the measurements of the obscured star formation rates, molecular gas content and ISM conditions in these young galaxies. In this thesis, we start by examining single-dish JCMT/SCUBA-2, *Herschel*/SPIRE and *Herschel*/PACS observations to investigate the far-infrared continuum emission from ∼4000 LAEs at $z = 2.2 - 6$ from SC4K and measure their Lyα escape fraction ($f_{\rm esc}({\rm Ly}\alpha)$). Five of the $\sim$ 4000 LAEs contain enough dust to be individually detected at 850 μm, with fluxes of $S_{850\mu{\rm m}} = 3.69$–5.50 mJy; all of these systems host AGN, suggesting AGN heating might be enhancing dust visibility. To probe the average dust emission from individually-undetected LAEs we use stacking to show that the average LAE has S_{100}, S_{160}, S_{250}, S_{350}, S_{500}

and S_{850} below the 0.24, 0.45, 0.27, 0.36, 0.36, and 0.09 mJy level (3σ), respectively. We also break the sample into bins of redshift, stellar mass, Lyα luminosity and AGN status. Most subsets are undetected, but stacks of the 298 LAEs with AGN, and the 669 most massive LAEs ($M_* = 10^{10-12}\,M_\odot$) are detected at most wavelengths, including with $S_{850} = 0.43 \pm 0.11\,\mathrm{mJy}$ and $S_{850} = 0.29 \pm 0.07\,\mathrm{mJy}$, respectively. Even when AGN are excluded the stack of most massive LAEs are still detected at the 4.5σ level at 250, 350 and 500 μm, indicating that the presence of dust in LAEs can be driven by stellar mass and not only AGN. The five individually-detected LAEs are found to have $f_{\rm esc}$(Lyα) = 1–7%, while detected stacks have $f_{\rm esc}$(Lyα) at the 4–5% level, and undetected stacks having higher limits (typically $f_{\rm esc}({\rm Ly}\alpha) \gtrsim 10\%$). The stack of all SC4K LAEs gives $f_{\rm esc}({\rm Ly}\alpha) > 21\%$ on average. We next utilize archival ALMA observations to probe deeper and detect faint SC4K LAEs that were missed by the single-dish observations. 375 SC4K LAEs were observed by ALMA and continuum emission is detected ($\geq 4.5\sigma$) in 15 of them, including 12 AGN. These LAEs have a wide range of $f_{\rm esc}$(Lyα), from 2% to 54%. Thus, deeper ALMA data are able to detect LAEs with higher $f_{\rm esc}$(Lyα) – i.e., LAEs with lower dust content compared to single-dish observations. Our results suggest that LAEs that contain AGN and those that are more massive, typically have lower $f_{\rm esc}$(Lyα) than the pure star-forming and lower mass systems. Examination of the relationship between infrared excess (IRX = $\mathrm{L_{IR}/L_{UV}}$) and the UV slope ($\beta_{\rm UV}$) for the LAEs using single-dish observations, limited by depth, suggests that LAEs have higher IRX than typical star-forming galaxies at similar redshifts, often above the Calzetti curve. However, deeper ALMA observations show that LAEs actually follow a similar IRX–$\beta_{\rm UV}$ relation to other star-forming galaxies like Lyman-break galaxies (LBGs). Furthermore, we examine the $\mathrm{SFR_{IR}}$–M_* relation for LAEs and find a potential offset of ~ 2 dex when compared to the $\mathrm{SFR_{Ly\alpha}}$–M_* relation. This suggests that significant amount of star formation in LAEs is obscured by the dust. To constrain the molecular gas content of LAEs, we use the ALMA archive to identify 34 LAEs that have ALMA observations at frequencies consistent with CO and [C I] 609 μm in their observed frame. Among these observations, we identify 12 potential line candidates, which result in six confirmed and two tentative detections of CO(3–2), CO(4–3), and CO(5–4) transitions in six LAEs. These detected LAEs have a median line luminosity of the order of $\sim 10^{10}\,\mathrm{K\,km\,s^{-1}\,pc^{2}}$, corresponding to molecular gas masses of $\sim 7 \times 10^{10}\,M_{\odot}$. We derive upper limits on molecular gas masses of $\sim (0.5\text{–}16) \times 10^{10}\,M_{\odot}$ for LAEs for which CO frequencies were observed but without being detected. The molecular gas fractions in LAEs are significantly higher than the other star-forming galaxies at similar redshifts, with a median of 0.92 ± 0.25 for detections. Moreover, we observe that LAE gas fraction decreases with increasing stellar mass, suggesting that LAEs may evolve into more typical star-forming galaxies as they grow.

Dedicated to my parents,
Mr Saijram Rana and Mrs Munni Devi,
for their continuous support and faith in my journey.

Acknowledgements

I would like to thank my supervisor, Julie Wardlow, for her constant support and encouragement throughout my PhD research. She not only listened to but also encouraged my ideas, motivated me to think creatively, helped me grow, and supported me in understanding basic concepts more clearly. This thesis would not have been possible without her continuous support and encouragement. I am specially thankful for her support in the early days, when there were complexities related to funding.

I want to thank Isobel Hook, John Stott, Brooke Simmons, Mathew Smith, Samantha Oates, David Sobral, Matt Pitkin, Young-Lo Kim, Klaas Wiersema, Chris Duffy, Lydia Makrygianni, Georgios Dimitriadis, Sonny Bailey and the entire observational astrophysics group at Lancaster University for providing a welcoming atmosphere that helped me adapt to a new culture and country. I am also grateful to every member of C45 office: Tom Cornish, Heather Wade, Pascale Desmet, Izzy Garland, Jamie Dumayne, David O'Ryan, Matt Thorne, Amy Hewitt, Nick Amos, Matthew Chan, Andrew Milligan, Harry Stephenson, Sam Shilling, Jason Shingirai Makechemu, Fergus Henstridge, Melzie Ghendrih and Alice Mead for creating a friendly and supportive environment throughout my time here. I am specially grateful to Julie's (Wardlow group) and David's group (XGAL group) for their valuable discussions and support, which helped me in making my research better. I will definitely miss being part of this wonderful department at Lancaster.

Thanks to my friends Arun Chauhan, Ashish Chauhan, Deewan Singh, Vikas Bisht, Vipin Chauhan and many more for always encouraging me. A special thanks to Gyanendra Yadav, Monika Chauhan and Rahul Rathi for long discussions on various topics and encouragement.

I am very thankful to my sisters, Sumitra and Seema for taking many responsibilities in my absence. Their support was invaluable in helping me complete this work.

Finally, I thank the National Overseas Scholarship (NOS) by the Indian Government for its financial support.

Declaration

This thesis is my own work and no portion of the work referred to in this thesis has been submitted in support of an application for another degree or qualification at this or any other institute of learning.

Data availability

In this thesis, we used data from the SC4K survey, as published in Sobral et al. (2018). The far-infrared data utilized in Chapter 2 were obtained from the S2COSMOS (Simpson et al., 2019), HerMES (Oliver et al., 2012), HELP (Shirley et al., 2021), and PEP (Lutz et al., 2011) surveys. In Chapter 3, we used data from the A^3COSMOS survey (Liu et al., 2019). Chapter 4 makes use of the following ALMA data that can be accessed from ALMA archive:

`ADS/JAO.ALMA#2016.1.00171.S`, `ADS/JAO.ALMA#2016.1.01001.S`, `ADS/JAO.ALMA#2016.1.01001.S`, `ADS/JAO.ALMA#2016.1.01001.S`, `ADS/JAO.ALMA#2016.1.01001.S`, `ADS/JAO.ALMA#2017.1.01359.S`, `ADS/JAO.ALMA#2018.1.01128.S`, `ADS/JAO.ALMA#2018.1.01225.S`, `ADS/JAO.ALMA#2018.1.01594.S`, `ADS/JAO.ALMA#2018.1.01594.S`, `ADS/JAO.ALMA#2018.1.01594.S`, `ADS/JAO.ALMA#2018.1.01673.S`, `ADS/JAO.ALMA#2018.1.01852.S`, `ADS/JAO.ALMA#2019.1.00459.S`, `ADS/JAO.ALMA#2019.1.01600.S`, `ADS/JAO.ALMA#2019.1.01600.S`, `ADS/JAO.ALMA#2019.1.01600.S`, `ADS/JAO.ALMA#2019.1.01600.S`, `ADS/JAO.ALMA#2019.1.01600.S`, `ADS/JAO.ALMA#2019.1.01600.S`, `ADS/JAO.ALMA#2021.1.00246.S`, `ADS/JAO.ALMA#2021.1.00246.S`, `ADS/JAO.ALMA#2021.1.00246.S`, `ADS/JAO.ALMA#2021.1.00246.S`, `ADS/JAO.ALMA#2021.1.00246.S`, `ADS/JAO.ALMA#2021.1.00246.S`, `ADS/JAO.ALMA#2021.1.00246.S`, `ADS/JAO.ALMA#2021.1.00246.S`,

`ADS/JAO.ALMA#2021.1.00705.S`, `ADS/JAO.ALMA#2021.1.01005.S`, `ADS/JAO.ALMA#2021.1.01005.S`, `ADS/JAO.ALMA#2021.1.01467.S`, `ADS/JAO.ALMA#2021.1.01467.S`, `ADS/JAO.ALMA#2022.1.00863.S`

ALMA is a partnership of ESO (representing its member states), NSF (USA), and NINS (Japan), together with NRC (Canada), NSTC and ASIAA (Taiwan), and KASI (Republic of Korea), in cooperation with the Republic of Chile. The Joint ALMA Observatory is operated by ESO, AUI/NRAO, and NAOJ.

“I seem to have been only like a boy playing on the seashore, and diverting myself in now and then finding a smoother pebble or a prettier shell than ordinary, whilst the great ocean of truth lay all undiscovered before me.”
– Sir Isaac Newton

Contents

1 Introduction **1**

List of Figures

List of Tables

Relevant Publications by the Author

Chapter 2

- “Constraining dust emission in Lyα emitters at $z = 2 - 6$ using far-infrared observations”; **Rana, R.** et al. (**in prep.**) to be submitted to MNRAS.

Chapter 3

- “Unveiling dust in Lyα emitters at $z = 2 - 6$ using ALMA observations”; **Rana, R.** et al. (**in prep.**) to be submitted to MNRAS.

Chapter 4

- “Constraining molecular gas content in Lyα emitters at $z = 2 - 6$ with ALMA observations”; **Rana, R.** et al. (**in prep.**) to be submitted to MNRAS.

Chapter 1

Introduction

1.1 Origin of the Universe: The Big Bang

As humans evolved and developed logical thinking, we became curious and started asking fundamental questions about the world around us. We started wondering about questions like, where we came from and how the Universe began. This curiosity keeps pushing us to explore and learn more. In pursuit of answers, we developed tools and scientific methods to investigate these mysteries. Over many years, we formed hypotheses, tested them with mathematics and observations, and gradually refined our understanding of the Universe. These combined efforts led to the development of the Big Bang theory, which is the best explanation we have for how the Universe began.

1.1.1 The standard model of cosmology

According to the Big Bang theory (proposed by Lemaître 1927), the Universe originated ~ 13.8 billion years ago from an extremely dense and hot singularity, which rapidly expanded, giving rise to all matter, energy, space, and time as we know today. The model which appears to explain much of this story, from the beginning to present, is the Λ–Cold Dark Matter (Λ–CDM) model, refined by numerous studies (e.g., Peebles, 1982; Perlmutter et al., 1998; Riess et al., 1998; Planck Collaboration et al., 2020) and which is currently our best model for understanding and predicting many of the physical properties of the Universe (e.g., Tegmark et al., 2004; Eisenstein et al., 2005; MacTavish et al., 2006).

The Λ–CDM model describes the composition of the Universe in terms of energy density, consisting of three key components. Ordinary or baryonic matter, which includes all atoms, stars and gas, makes up only $\sim 5\%$ of the total energy density. Dark matter, an invisible substance or force accounts for $\sim 27\%$ of energy density and plays a key role in cosmic structure formation (White & Rees, 1978; Blumenthal et al., 1984; Navarro et al., 1997; Springel et al., 2005). It is unique, because it interacts only gravitationally and does not emit or absorb light. The dominant component, dark energy, accounts for $\sim 68\%$ and it is believed to be responsible for the accelerated expansion of the Universe (see Perlmutter et al., 1998; Riess et al., 1998; Padmanabhan, 2005; Frieman et al., 2008, for more details), represented by the cosmological constant (Λ).

The mathematical background of the Λ–CDM model is based on the Friedmann equations, derived from Einstein's field equations of general relativity (Einstein, 1916; Friedmann, 1922). These equations describe the expansion of the Universe and are essential for modelling its evolution. The first Friedmann equation is:

$$H^2 = \left(\frac{\dot{a}}{a}\right)^2 = \frac{8\pi G}{3}\rho - \frac{kc^2}{a^2} + \frac{\Lambda c^2}{3} \tag{1.1}$$

where, H represents the Hubble parameter, indicating the current rate of expansion of the Universe; the size of the Universe at a given time is represented by the scale factor a; ρ is the total energy density (including ordinary and dark matter, radiation, and dark energy); k is the curvature parameter, indicating whether the Universe is open, closed, or flat; G is the gravitational constant; c is the speed of light; and Λ is the cosmological constant, linked to dark energy. The second Friedmann equation is:

$$\frac{\ddot{a}}{a} = -\frac{4\pi G}{3}\left(\rho + \frac{3p}{c^2}\right) + \frac{\Lambda c^2}{3} \tag{1.2}$$

which describes the acceleration of the expansion of the Universe, where $\ddot{a}$ is the second time derivative of the scale factor (acceleration), and p is the pressure, accounting for the effects of different components like radiation and dark energy. In the above equations, H, a, ρ and p are all functions of time.

The Λ–CDM model is consistent with observational evidence such as the relationship between a galaxy's distance from us and its recession velocity, observed by Slipher (1917) and Hubble (1929). The Λ–CDM model successfully incorporates and explains this observation. This support was followed by the detection of the Cosmic Microwave Background (CMB) radiation by Penzias & Wilson (1965). The CMB spectrum follows an almost perfect Planck blackbody curve, peaking at a wavelength of $\sim$1 mm corresponding to $\sim$2.7 K (e.g., Planck Collaboration et al., 2020). The ability of Λ–CDM to explain both the Hubble's law and the CMB blackbody spectrum and its anisotropy has solidified its robustness, even though mysteries like dark matter and dark energy still remain unsolved. Furthermore, the idea of dark energy in the Λ–CDM model gained strong support from the discovery of the accelerated expansion of the Universe in 1998 from observations of Type Ia supernovae (Perlmutter et al., 1998; Riess et al., 1998). The two teams found that distant Type Ia supernovae are fainter than expected, demonstrating that the Universe is not only expending but that its expansion is also speeding up. This finding further solidified the idea of dark energy, thus strengthening the Λ–CDM model.

To understand the importance and implications of these findings, we need to look back to the early Universe, when the cosmos was an extremely hot and dense plasma of quarks, gluons, and photons. In this state, photons were constantly interacting with free electrons and protons, scattering repeatedly and unable to travel freely. This phase ended when the Universe expanded and cooled sufficiently for electrons and protons to combine and form neutral atoms like hydrogen and helium. This transition enabled photons to decouple from matter and finally emerge as the CMB we observe today. These critical events, known as recombination and decoupling, occurred when the Universe was at a temperature of $\sim$ 3000 K at redshift z $\sim$1100 (Peebles, 1968; White et al., 1994; Planck Collaboration et al., 2020). After the Universe became transparent, a new era in cosmic history began, known as the cosmic dark ages. Although the Universe was now transparent to light, no stars or galaxies had yet formed to emit light. The

Universe was filled with neutral hydrogen and helium gas, along with dark matter. It was a period of complete darkness, waiting for the conditions to be right for the formation of the very first stars and galaxies (Rees, 1999; Miralda-Escudé, 2003; Stachniewicz & Kutschera, 2005).

1.1.2 Formation of the first stars and galaxies: cosmic dawn

During the dark ages, gas and dark matter are thought to have started evolving under gravity provided by the gravitational potential well of cold dark matter. This process is believed to have facilitated the formation of the first stars and galaxies (Abel et al., 2002; Bromm et al., 2002; Bromm, 2004). The high-density of cold dark matter in halos can create deep gravitational wells that can attract baryonic gas, allowing it to cool, condense, and collapse to form the first stars known as Population III stars (Bromm 2004; Stacy et al. 2016; for a recent review, see Klessen & Glover 2023). This event marked the beginning of cosmic dawn, a transition in the history of the Universe, ending the cosmic dark ages. Population III stars are expected to have been massive, short-lived, and composed mainly of hydrogen and helium (Bromm et al., 2002). The lack of metals and dust can result in inefficient cooling, which can reduce fragmentation and cause gas clouds to collapse into larger protostars. The Jeans mass, which is directly proportional to temperature ($\mathrm{M}_J \propto T^{3/2}$), is expected to be higher due to poor cooling mechanisms. These massive stars can burn their fuel quickly through multiple fusion mechanisms, which makes them short-lived (Jappsen et al., 2007; Clark et al., 2011; Jog, 2013).

About 200–400 million years after the Big Bang ($z \approx 20$–10), population III stars started clustering under the gravity of dark matter and gas which resulted in the birth of the first galaxies. Small, irregular galaxies formed first and they went through intense star-formation. The gravitational mergers of these galaxies eventually resulted in the formation of larger and more structured galaxies, such as spirals and ellipticals (Figure 1.1; Springel et al., 2005; Mori & Umemura, 2006). The early galaxies mainly hosted metal-poor stars, as their interstellar

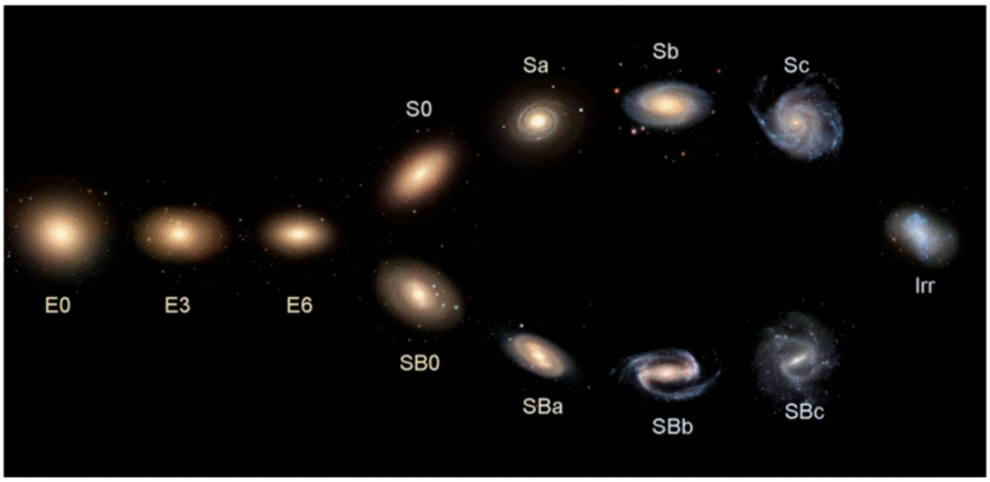

Figure 1.1: The Hubble tuning fork diagram illustrating the morphological classification of galaxies, starting with elliptical galaxies denoted E0 to E6, where E0 galaxies are nearly spherical and E6 galaxies are elliptical. Spirals are denoted by – SB0, Sa etc. The spiral lower branch shows spiral galaxies with central bars, where the letters from c to a indicate increasing tightness of spiral arms. The upper branch is similar for spirals without bars. The colour of galaxies changes from bluish on the right to reddish on the left, showing that spirals are typically blue, young and forming stars. Red galaxies contain older and more evolved stars. This image is from Cui et al. (2014).

medium (ISM) had not yet been significantly enriched. Supernovae from Population III stars enriched the gas with heavier elements (e.g., carbon, oxygen, iron), making the way for the next stellar generations (Population II and I; Woosley et al. 2002). Feedback from supernovae regulated star formation by heating and expelling gas (e.g., Hasegawa et al., 2009; Whalen et al., 2010; Sugimura et al., 2024) and intense ultraviolet radiation from these young galaxies began the epoch of reionization ($z \approx 20$), by ionizing the surrounding neutral hydrogen (Loeb & Barkana, 2001; Benson et al., 2006; Bunker et al., 2008; Wise, 2019). This process made the intergalactic medium (IGM) transparent to light and allowed photons to travel freely. It was a critical step especially for the short-wavelength light, like Lyα photons. The reionization process is thought to have completed about 1 billion years ($z \approx 6$) after the Big Bang (Becker et al., 2001; McGreer et al., 2015).

1.2 Properties of galaxies

Galaxies are the fundamental building blocks of the Universe. They are gravitationally bound systems of stars, gas, dust, and dark matter. To understand how they form and evolve over cosmic time, we classify them based on shapes, structures, and their different components.

1.2.1 Morphological classification

Galaxies have a wide range of properties. They are commonly classified by morphology using the Hubble sequence in the tuning fork diagram, introduced by Hubble (1926, Figure 1.1). This classification divides galaxies in the local Universe into three main types, namely ellipticals, spirals, and irregulars. Elliptical galaxies (E0–E6) range from nearly spherical (E0) to highly elliptical (E6). They are dominated by older, low-mass stars and appear reddish in colour. This suggests that their most massive stars have already completed their main sequence lifetimes and the galaxies are not forming many new stars (Djorgovski & Davis, 1987; Kormendy et al., 2009). On the other hand, spiral galaxies, which includes our own Milky Way, have two main categories, based on the presence and absence of a central bar. These categories are further divided into subcategories based on the tightness of their spiral arms. The tightness of spiral arms increases from type Sc to Sa, with S0 (lenticulars) appearing to be a transition between spirals and elliptical. Spiral galaxies have a central bar structure and are classified as barred spirals (e.g., SBa, SBb, SBc), following a similar pattern of arm tightness. Spiral galaxies are typically rich in gas which fuels star formation (Kennicutt, 1983; Kennicutt et al., 1994; McGaugh & de Blok, 1997), leading to their usual bluish colour. Their spiral arms contain young, massive stars, while their bulges/bars host relatively older stellar populations (Kennicutt, 1998b). Irregular galaxies (Irr), (e.g, the Large and Small Magellanic Clouds) generally lack defined structures. They are usually also rich in star formation fuel and actively form stars. They are young and likely to be evolve into spirals or ellipticals through gravitational interactions and/or mergers with nearby galaxies (Moore et al., 1996; Toomre, 1977).

1.2.2 Key components of galaxies

Apart from the dark matter, there are four key components of galaxies namely, stars, gas, dust, and supermassive black holes. These components interact to shape structure and evolution of a galaxy throughout its lifetime.

1.2.2.1 Stellar component

Stars are a fundamental part of galaxies. They make up most of their visible light and a large fraction of their mass. The Morgan–Keenan (MK) system (Morgan & Keenan, 1973), classifies stars into the spectral types O, B, A, F, G, K and M, based on their surface temperatures and colours. O & B-type stars are the hottest and most massive, with surface temperatures above 10,000 K and masses above 2 solar masses ($M_\odot$). These blue stars are short-lived and generally end their life through supernovae, forming neutron stars or stellar black holes. A, F & G–type stars are of intermediate masses, have white to yellow-white colours. Low mass ($\lesssim 0.08 M_\odot$) K and M types are red and longer lived.

Stars spend most of their life in the stable main sequence phase. As hydrogen runs out, stars expand into a red giant or supergiant, depending on their masses. The final stage of stellar evolution depends on a stars mass and is governed by the Chandrasekhar limit ($\approx 1.4 M_\odot$; Chandrasekhar, 1931). Low-mass stars (final core mass $\leq 1.4 M_\odot$) become white dwarfs, while more massive stars result in a core-collapse supernova, which leaves either a neutron star or (if massive enough) a black hole (Carroll & Ostlie, 2017; Karakas & Lattanzio, 2014). These supernovae explosions can spread the heavy elements into the surrounding gas (Woosley & Weaver, 1995; Thielemann et al., 1996; Heger & Woosley, 2010; Nomoto et al., 2013), an enrichment process that is essential for forming new stars and planets.

The fraction of stars of different masses formed in a stellar population is described by the Initial Mass Function (IMF; e.g., Salpeter, 1955; Kroupa, 2001; Chabrier, 2003). The IMF impacts the derivations of galaxy properties such as luminosity, stellar mass, star formation rate, and mass-to-light ratio. For instance, a top-heavy IMF (e.g., Chabrier, 2003), leads to more massive stars, elevating the UV luminosity and supernova feedback, while a bottom-heavy IMF (e.g., Salpeter, 1955) increases the number of faint, low-mass stars, enhancing the mass-to-light ratio. The IMF predicts that massive stars are rare, but their luminosity and blue colour dominate the light and colour of young, star-forming galaxies. These massive stars are short-lived, so when star formation stops these stars die off quickly. The galaxy's light then becomes dominated by long-lived, low-mass, red stars, shifting its colour toward red—an indicator of an older stellar population.

1.2.2.2 The Interstellar Medium

The interstellar medium (ISM) is the matter that fills the space between stars within a galaxy, consisting mostly of gas ($\sim 99\%$) and a small amount of dust ($\sim 1\%$). Although it typically constitutes only ~10–20% of baryonic mass of a galaxy (Draine, 2011), it serves as both the raw material for star formation and the dumping ground for matter expelled by old stars. While dust makes up only a small part of the ISM, it plays a critical role in shaping the physical and chemical evolution of galaxies. It is made of tiny solid particles, mainly silicates (e.g., olivine and pyroxene), carbon-based compounds such as graphite and amorphous carbon grains, and polycyclic aromatic hydrocarbons (PAHs) including naphthalene, anthracene, and phenanthrene (Dwek et al., 1997; Li & Draine, 2001; Draine & Li, 2007). The origin of interstellar dust is connected to the later evolutionary stages of stars. Evolved stars, mainly those on the asymptotic giant branch (AGB), and explosive events such as core-collapse supernovae are the primary producers of dust (Dunne et al., 2003; Inoue, 2011; Kemper, 2013; Zhukovska & Henning, 2013). As the hot debris from these stars cools, heavier elements like carbon, silicon, and oxygen combine to form dust grains (Asano et al., 2013a,b). These small dust grains range in size from ~1 nm to ~0.3 μm.

Despite their small size, interstellar dust grains have a significant effect on the radiative properties of galaxies. Smaller grains are efficient at absorbing high-energy UV light and re-emitting this energy in the infrared part of the spectrum. This infrared emission provides an alternative observational window into dusty galaxies which are difficult to observe in UV/optical light (Riguccini et al., 2011; Wild et al., 2011, Section 1.4.2). Moreover, dust plays a key role in the process of star formation. It acts as a shield, protecting dense molecular clouds from the destructive effects of UV photons by absorbing and scattering them. This process helps to preserve the cold, dense environments required for molecule formation and gravitational collapse. Dust grains also help in cooling gas clouds by absorbing starlight and releasing heat as infrared radiation (Arshutkin, 1980; Burke & Hollenbach, 1983; Montier & Giard, 2004; Vogelsberger et al., 2019). This cooling decreases the pressure inside the clouds, enabling gravitational collapse and the formation of stars. Therefore, interstellar dust is not just a by-product of stellar activity, it is an active component in regulating the stability and activity of star formation. Understanding the composition, origin, and the impact of dust on the various physical properties of galaxies are crucial for understanding the mechanisms of galaxy evolution.

The gas in galaxies is the other main component of the ISM. The gaseous components of hydrogen exist in different phases namely, neutral atomic hydrogen (HI), ionized hydrogen (HII), and molecular hydrogen (H_2). HI is usually found in cooler, less dense regions and it serves as a large source of raw material for future stars. On the other hand, HII regions are usually created when high-energy UV radiation from massive, young stars ionize the surrounding hydrogen, making HII regions good indicators of active star-forming regions (Hodge, 1986; Hester & Desch, 2005; Zavagno et al., 2010). Molecular hydrogen (H_2) is the phase from which stars form, via the gravitational collapse of cold, dense molecular clouds.

1.2.2.3 Supermassive black holes

Supermassive black holes (SMBHs) are found at the centres of most galaxies (Kormendy & Richstone, 1995; Magorrian et al., 1998; Genzel et al., 2010). When material falls toward these black holes, it heats up to form a bright, rotating accretion disk. Thus, when SMBHs accrete matter, they can become bright objects known as active galactic nuclei (AGN). SMBHs play a role in shaping the future of their host galaxies through AGN feedback, as suggested by the empirical correlation between black hole mass and the stellar mass of galaxies (Figure 1.2). AGN feedback can heat or expel surrounding gas, which helps regulate galaxy growth by slowing down or even stopping star formation in some regions (Schawinski et al., 2007; Fabian, 2012). Feedback processes can also trigger star formation by compressing nearby gas clouds (Ishibashi & Fabian, 2012; Liu et al., 2013; Zubovas et al., 2013). An example of the impact of an AGN on galaxy evolution is shown in Figure 1.3.

AGN can be identified via multi-wavelength observations, including in the X-ray, UV/optical, infrared, or radio. In the UV/optical, AGN emit strong emission lines such as Lyα, C IV 1549, [O III] 5007, Hα, and Hβ, originating from the surrounding gas ionized by their intense radiation (Osterbrock, 1989). Emission-line analysis, such as the BPT diagram (Baldwin et al., 1981), can help to separate AGN from star-forming galaxies. In the infrared, AGN-heated dust emits thermal radiation (Neugebauer et al., 1979), providing an alternative method of detection. This emission can contaminate thermal dust emission from star-forming regions, making it difficult to disentangle the contributions from AGN activity and star formation (Netzer et al., 2007; Kirkpatrick et al., 2015). X-ray observations provide a more direct probe of AGN activity, as they can penetrate dense obscuring material and reveal both unobscured and heavily obscured AGN (Brandt & Alexander, 2015). Radio emission, usually associated with relativistic jets, offers another extinction-free method of AGN detection (Miley & De Breuck, 2008; Padovani et al., 2017).

1.3 Galaxy Evolution

The Universe began with a hot, expanding plasma after the Big Bang. Structures are believed to have gradually emerged from initial perturbations, forming the first galaxies as discussed in Section 1.1.2. Over cosmic time, these early systems transformed through star formation, mergers, and feedback, giving rise to the morphological diversity (Baugh et al., 1996), highlighted in the Hubble sequence. Today, galaxies span a wide range of properties shaped by their environments. Spirals are more common in isolated or low-density regions, while massive ellipticals and lenticulars tend to reside in clusters (Einasto & Einasto, 1987; Zabludoff & Franx, 1993). This section introduces the broad picture of galaxy evolution, beginning with the evolution of the SFR, and how the ISM evolves over time.

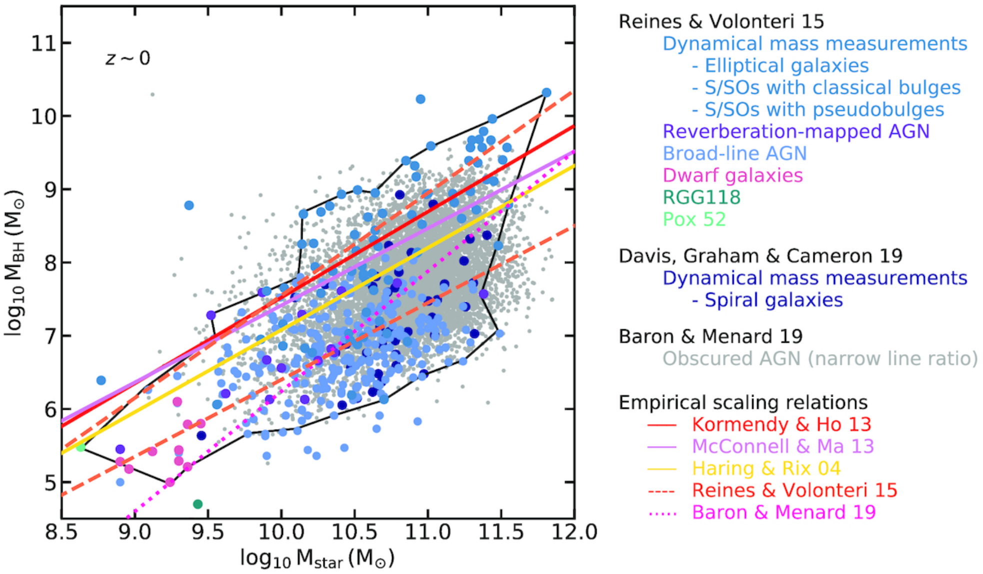

Figure 1.2: The correlation between supermassive black hole mass and the stellar mass of their host galaxies. Empirical scaling relations from the literature are shown for both $M_{\rm BH}$–$M_{\rm bulge}$ (solid lines) and $M_{\rm BH}$–$M_{\star}$ (dashed lines). Observations for ellipticals, spirals with classical and pseudobulges, broad-line AGN, dwarf galaxies, spiral galaxies, and obscured (narrow-line) AGN are shown in different colours. Figure from Habouzit et al. (2021).

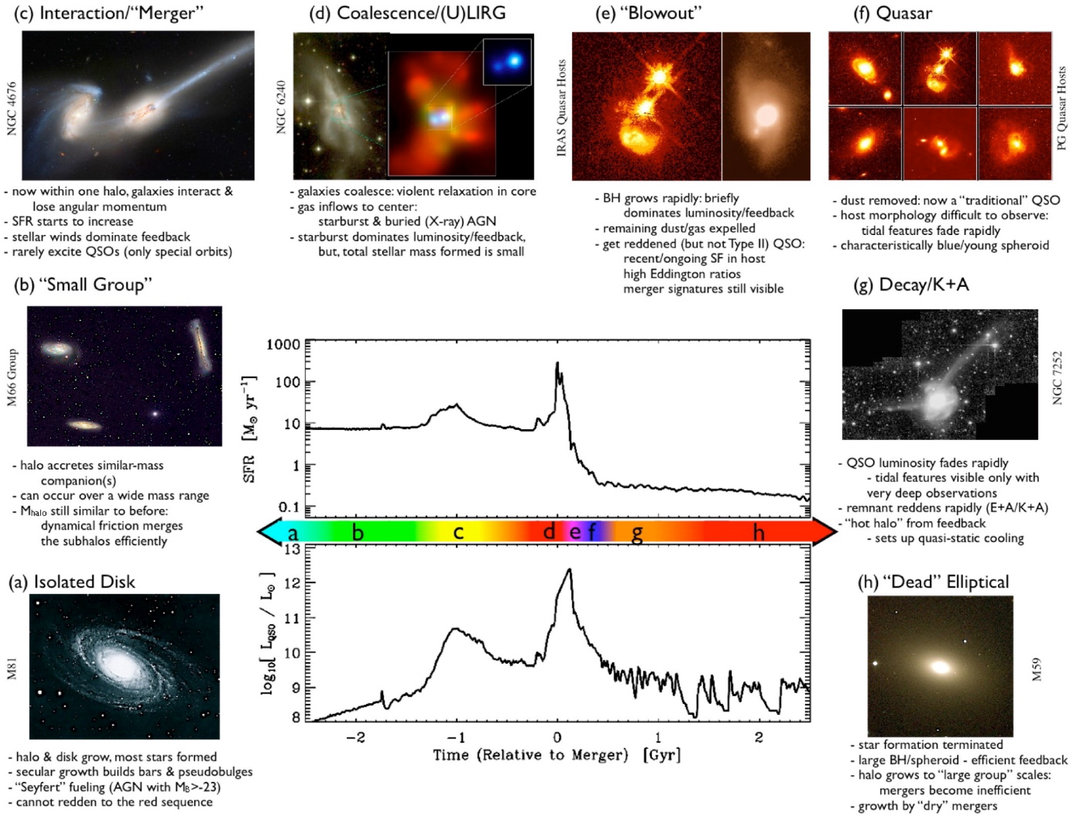

Figure 1.3: A proposed evolutionary pathway for a young spiral galaxy to transform into an elliptical galaxy. The middle panel shows the SFR (top) and the luminosity of the supermassive black hole (bottom) as a function of time relative to the merger. Panels (a) to (h) show the evolutionary stages of a galaxy, including: an isolated spiral galaxy, small group interactions, mergers, (U)LIRG phase, blowout phase, quasar activity, fading QSO luminosity, and the final quiescent elliptical galaxy. Figure from Hopkins et al. (2008).

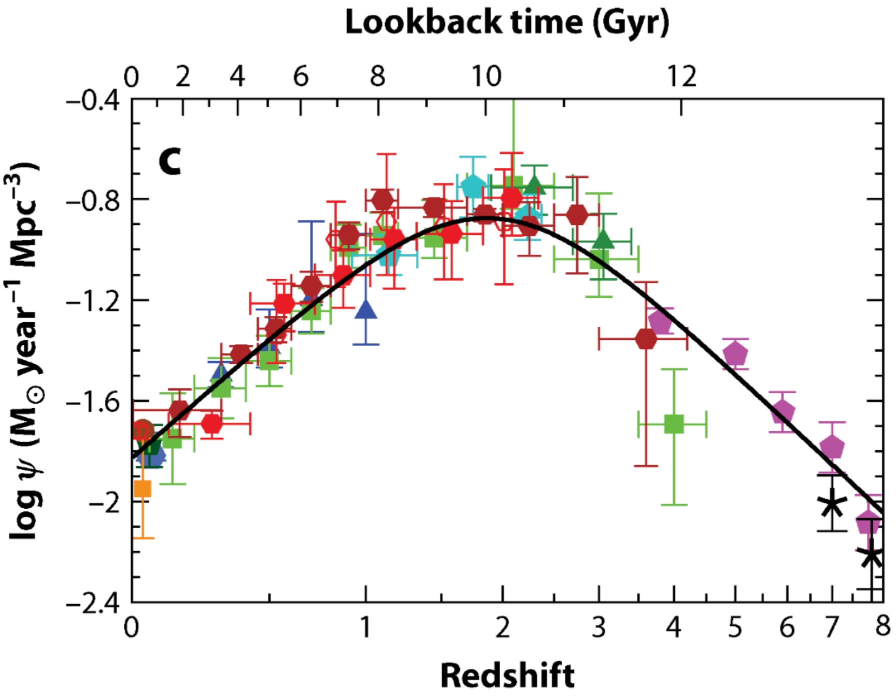

Figure 1.4: The cosmic star formation rate density as a function of redshift, from Madau & Dickinson (2014). UV-based measurements are shown in green, blue, cyan, and magenta; infrared-based measurements are shown in orange, red, and brown.

1.3.1 Evolution of SFR

The star formation rate (SFR) measures how fast a galaxy forms new stars. It reflects the growth and activity of a galaxy. The SFR of the Universe has evolved over cosmic time, reaching a peak at $z \sim 2$, then declined to current levels (Madau & Dickinson, 2014). This trend is expressed through the cosmic star formation rate density (SFRD), which describes the rate at which new stars form per unit volume, (e.g. Figure 1.4). It helps us understand when most stars form, how galaxies evolve, and how the Universe transitioned from more active star formation to its relatively more quiescent, current state.

On a smaller scale, this universal behaviour is reflected in the galaxy main sequence. The observed galaxy main sequence shows a correlation between SFR and stellar mass (Daddi et al., 2007; Elbaz et al., 2007; Noeske et al., 2007).

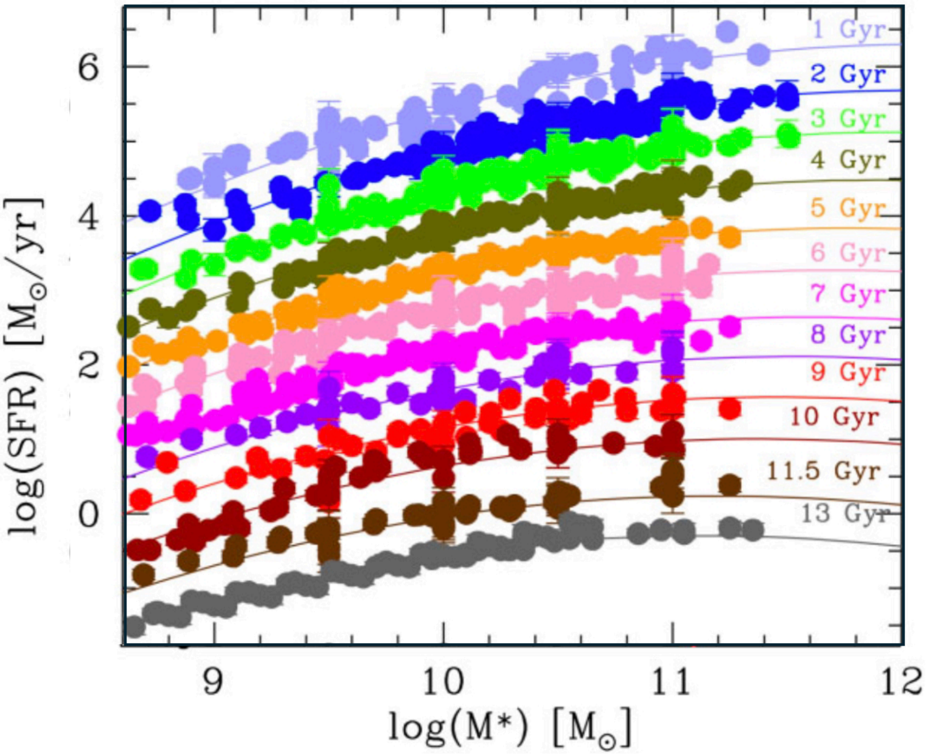

Figure 1.5: Evolution of the galaxy main sequence over cosmic time. This figure illustrates how the SFR of typical galaxies changes from earlier epochs to the present day. The different coloured lines indicate the age of the Universe, from 1 to 13 billion years, corresponding to redshift $z\sim 6$ to 0. Figure from Popesso et al. (2023).

This suggests that galaxies with higher stellar masses generally form stars at a higher rate. It has been observed across a wide range of redshifts, from the local Universe up to $z \sim 6$, suggesting that the main sequence is likely a fundamental feature of galaxy evolution (e.g., Figure 1.5, Speagle et al., 2014; Popesso et al., 2023). The normalisation of the main sequence evolves to higher SFRs at fixed stellar mass with increasing redshift. Galaxies above the main sequence are thought to be starbursts and may be triggered by galaxy mergers or interactions (Jogee et al., 2009). On the other hand, galaxies that are below this sequence are typically quenching or passive. Morphologically, main sequence galaxies are mainly disk-dominated systems with low Sérsic indices ($n \sim 1$), while galaxies below the main sequence tend to have more bulge-dominated structures with higher Sérsic indices (Schiminovich et al., 2007; Wuyts et al., 2011; Bruce et al., 2014). Furthermore, AGN hosts generally lie on or slightly below the galaxy main sequence, particularly at higher stellar masses. This trend, combined with their higher Sérsic indices, suggests that AGN feedback may play a role in regulating or quenching star formation, which can broaden the main sequence (Zhang et al., 2016; Cristello, 2024; Mountrichas et al., 2024).

1.3.2 Evolution of the ISM

Dust and gas are two key components of the ISM (Section 1.2.2.2) and play an important role in governing the evolution of galaxies. Despite being only ∼1% of the ISM, dust is closely linked to star formation and metal enrichment history of a galaxy. The local galaxies, like our own Milky Way, generally have more dust than more distant systems. Distant galaxies represent earlier stages of galaxy evolution and typically contain lower dust content, with masses ranging from $\sim 10^6$ to $10^7\,M_\odot$ (Hirashita et al., 2017). This lower dust content reflects their younger stellar populations, which have not yet produced enough metals to form significant amount of dust. Despite this, high-z galaxies upto $z \sim 7$ contain enough dust to be detected by advanced telescopes like Atacama Large Millimeter/Submillimetre Array (ALMA; e.g., Riechers et al., 2013; Watson et al., 2015; Strandet et al., 2017). However, the average dust density is expected to have peaked at $z \sim 1$ (e.g., Figure 1.6; Lewis et al., 2023; Beeston et al., 2024). For

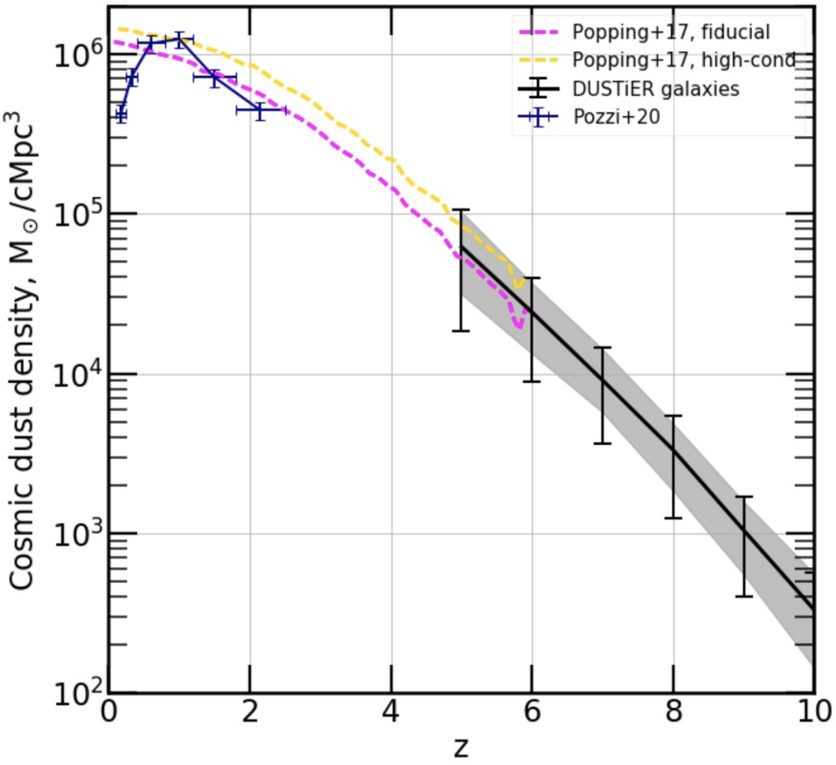

Figure 1.6: Evolution of comoving cosmic dust density as a function of redshift from the DUSTiER simulation (black solid line), compared with semi-analytic models (SAMs). This figure illustrates that dust density begins to decrease around redshift $z \sim 1$ and continues declining towards higher redshifts. The DUSTiER is a cosmological simulation based on a physical model for dust production to study dust evolution during the epoch of reionization. Figure from Lewis et al. (2023).

instance, the DUSTiER (DUST in the Epoch of Reionization) simulation from Lewis et al. (2023), models the physical processes responsible for dust production in galaxies and suggests that the comoving cosmic dust density increases up to $z \sim 1$ and starts to decline beyond $z \sim 1$ due to decline in cosmic star formation and dust production, while dust destruction in the ISM continues, leading to a drop in dust density.

Being a dominant component of the ISM (Section 1.2.2.2), gas plays a crucial role in galaxy evolution. As the Universe evolves from the early epoch to the present day, the gas content in galaxies is consumed by activities such as ongoing star formation, and accretion by the SMBH (Decarli et al., 2016; Tacconi et al.,

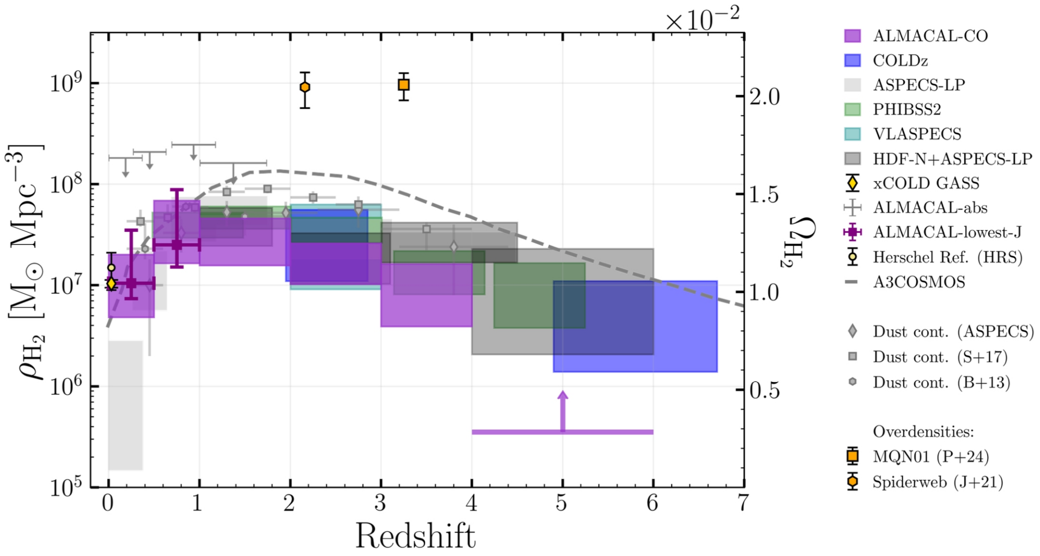

Figure 1.7: The global comoving molecular gas mass density as a function of redshift rises with increasing redshift from $z = 0$, reaching a peak at $z \approx 1.5$, then starts declining toward higher redshifts ($z \sim 6$). This Figure compares the observed trend with the predicted evolution shown by the grey dashed line, based on theoretical models. The right y-axis shows the unitless density parameter for molecular gas, $\Omega_{H_2} = \rho_{H_2}/\rho_{\mathrm{crit,\,z=0}}$, where $\rho_{\mathrm{crit,\,z=0}}$ is the critical density of the Universe today ($\sim 10^{-26}\,\mathrm{kg\,m^{-3}}$). It is a reference for the total mass–energy density required for a flat Universe. Figure from Bollo et al. (2025).

2020; Wang et al., 2022; Bollo et al., 2025). As early galaxies ($z \gtrsim 2$) have access to abundant gas reservoirs in the CGM and IGM (Genzel et al., 2010; Silverman et al., 2015), they can accrete the gas. As a result, these galaxies are expected to be more gas-rich compared to their local counterparts (Tacconi et al., 2010; Carilli & Walter, 2013). Furthermore, these galaxies have not had enough time to evolve and exhaust their gas content. The cosmic gas content is typically assessed through the global molecular gas mass density, defined as the total molecular gas mass per unit comoving volume. It shows a significant evolution with redshift (Figure 1.7) and may help to control the evolution of cosmic SFRD. Recent observations (e.g., Maeda et al., 2017; Garratt et al., 2021; Bollo et al., 2025) show that the cosmic gas density peak around $z \approx 1.5$, which roughly coincides with the peak of cosmic star formation rate density (Madau & Dickinson, 2014). Gas density starts declining at $z \approx 1.5$ which results in more quiescent and gas-poor galaxies in the local Universe (Bothwell et al., 2009; Gobat et al., 2020; Williams et al., 2021; Saintonge & Catinella, 2022).

1.4 Observing distant galaxies

Observing distant galaxies allows us to investigate the history of the Universe, enabling us to study the formation and evolution of cosmic structures that existed billions of years ago. To understand the complete picture of galaxy formation and evolution, we need to observe both the local and distant Universe. Some of the most distant galaxies observed to date have redshifts $z > 10$ (Castellano et al., 2022; Atek et al., 2023; Bunker et al., 2023; Curtis-Lake et al., 2023; Carniani et al., 2024). These observations provide crucial insights into the beginning of reionization ($z \approx 20$), when the first stars and galaxies formed and started reionizing the IGM (Loeb & Barkana, 2001; Muñoz et al., 2022; Umeda et al., 2025; Witstok et al., 2025). However, observing these distant galaxies is highly challenging. Their light is extremely faint and shifted into the infrared region of the electromagnetic spectrum due to the expansion of the Universe. Additionally, interstellar dust and gas (Section 1.2.2.2) can obscure this light, complicating observations. To overcome these challenges, we need advanced,

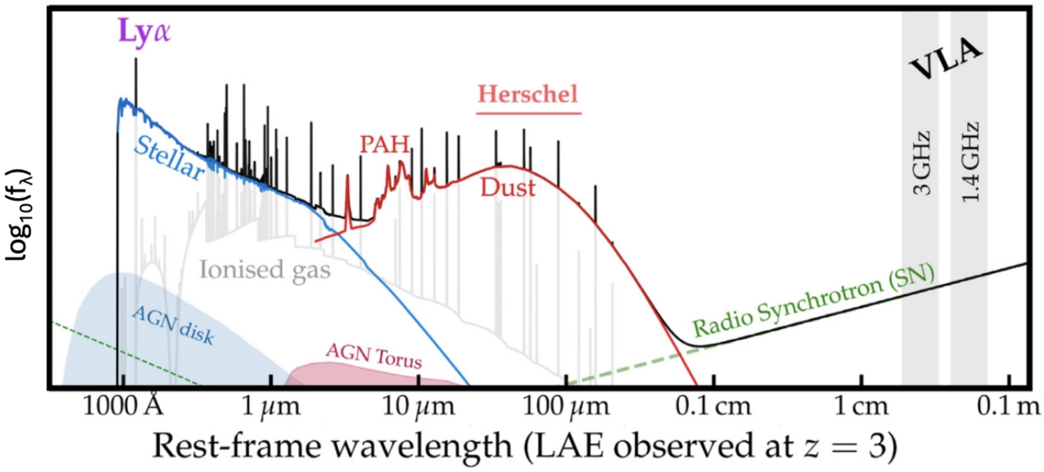

Figure 1.8: Typical spectral energy distribution (SED) of a star-forming galaxy from the UV to the radio wavelengths. The SED shows contributions from different components such as stellar light, ionized gas, and the accretion disk and dusty torus of an AGN. The UV-optical light absorbed by the dust is re-emitted at infrared wavelengths (red curve). The Lyα line is shown near the sharp Lyman break on the left (UV end), while the radio wavelengths on the right trace synchrotron emission. Figure adapted from Calhau et al. (2020).

sensitive instruments that detect faint signals at multiple wavelengths. Space telescopes like *Hubble* and *Herschel* have revealed galaxies in UV/optical, and far-infrared, while JWST (launched in 2021) offers high-resolution infrared views of early galaxies. On the ground, interferometers such as ALMA are crucial for studying the cold dust and molecular gas in early galaxies. This observatory provides high-resolution imaging and spectroscopy at submillimetre and millimetre wavelengths which helps us to observe dust-obscured star formation and gas in distant galaxies. By combining JWST, *Hubble*, and *Herschel* in space with ALMA and optical and near-infrared facilities on the ground, we can now overcome the challenges posed by cosmological redshift, atmosphere, and obscuration.

1.4.1 UV/optical continuum

The UV/optical continuum emission (rest-frame $\sim$ 100–750 nm) from galaxies is one of the most widely used tracers of recent star formation in distant galaxies.

This emission mainly traces active star-forming regions. UV/optical continuum is a crucial indicator of recent star formation and the younger stellar population of galaxies at high redshifts ($z > 2$). In the rest-frame of a galaxy, the UV continuum covers ∼100–300 nm, and the optical continuum ranges from ∼300–750 nm (Figure 1.8). However, due to cosmological redshift, this light shifts to longer wavelengths. For instance, in a galaxy at $z \sim 3$, the UV/optical light is observed in the optical to near-infrared range (∼400–3000 nm). This requires sensitive instruments like the *Hubble*, JWST, or large ground-based telescopes such as Keck or the Very Large Telescope (VLT).

The shape of the UV continuum is generally described using the UV slope, β_{UV}. It is defined by a power law of the form

$$F_\lambda \propto \lambda^{\beta_{\mathrm{UV}}}, \tag{1.3}$$

where F_λ indicates the flux density ($\mathrm{erg\,s^{-1}\,cm^{-2}\,\AA^{-1}}$), λ represents the rest-frame wavelength (Å), and β_{UV} is the dimensionless spectral slope of the continuum. This parameter is used to estimate properties such as the UV luminosity, star formation rate, dust extinction, and stellar metallicity (e.g., Meurer et al., 1999; Calzetti et al., 2000; Mondal & Saha, 2024). However, observing the UV/optical continuum in high-redshift galaxies presents significant observational challenges. One major issue is absorption by the IGM, mainly below the Lyman limit (912 Å), where neutral hydrogen blocks UV light (Gunn & Peterson, 1965). Furthermore, dust within galaxies can absorb and scatter UV photons, making the UV continuum appear redder and complicating the interpretation of the intrinsic properties.

1.4.2 Far-infrared continuum

Far-infrared continuum emission can penetrate through the dust that obscures galaxies' UV/optical light. This helps us to unveil dust-obscured star formation, providing an alternative window into the physical processes governing star formation and galaxy evolution (Casey et al., 2014a,b; Zhao & Furlanetto, 2024).

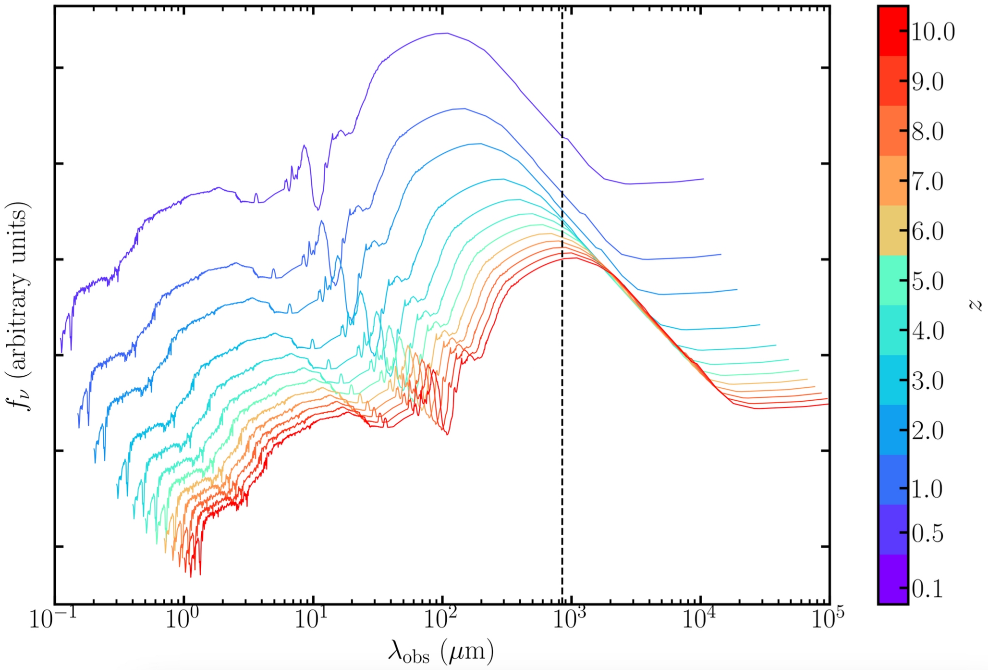

Figure 1.9: SED model of the nearby ULIRG Arp 220 (Silva et al., 1998) figure from Cornish (2023), shown at different redshifts, as indicated by the colourbar. The vertical dashed line at $\lambda \approx 850\mu$m shows where the flux density remains nearly constant from $z = 1$ to 10. This shows the effect of the negative K-correction, which allows dusty galaxies to be observed even at high redshifts.

This far-infrared emission arises from dust grains heated by young, massive stars and it captures reprocessed light from star-forming regions.

One advantage of the far-infrared is the "negative" K-correction, which, as shown in Figure 1.9 leads to the apparent far-infrared flux remaining constant for a fixed SED at $z \sim$ 1–10 (Silva et al., 1998). This phenomenon is useful for observing faint, high-redshift galaxies, enabling the study of their obscured star formation and the ISM (e.g., Maiolino et al., 2005; Lu et al., 2018; Wardlow et al., 2018; Birkin et al., 2021; Kolupuri et al., 2025). The shape of the dust continuum SED is presented in Figure 1.9, which peaks at rest-frame wavelengths of ∼100 μm, with the precise position of the peak depending on the dust temperature (typically $T_{\rm dust} \approx$ 20 − 100 K), which depends on the physical condition in a particular galaxy (Casey, 2012; Magnelli et al., 2014). The slope of the longer wavelength side of the SED, the Rayleigh-Jeans tail, predominantly depends upon the dust grain size distribution, and is governed by the dust emissivity index ($\beta_{\rm IR}$). This index shows how efficiently dust grains absorb and emit radiation (Draine, 2006; Shetty et al., 2009; Casey, 2012). On the other hand, the shorter wavelength side of the SED follows a power-law slope (α) which predominantly depends on dust temperature, particularly in AGN-host or starburst galaxies, where intense heating can steepen the mid-infrared power-law slope (Casey, 2012). Additionally, as dust and gas in the ISM correlate with each other (Leroy et al., 2011; Eales et al., 2012; Magdis et al., 2012; Scoville et al., 2016), the far-infrared continuum can be used as an indirect tracer of molecular gas mass by utilising empirical measurements of a dust-to-gas ratio. It offers an effective alternative to CO-line observations (see Section 1.4.3 for more details), which are more observationally expensive.

1.4.3 Spectroscopy

By dispersing light into its constituent wavelengths, spectroscopy reveals the unique fingerprints of elements and physical conditions. Bright emission lines such as Lyα (∼121.6 nm), Hα (∼656.3 nm), Hβ (∼486.1 nm), [O II] (372.7 nm), and [O III] (∼495.9 nm, ∼500.7 nm doublet) are key spectroscopic tools in the

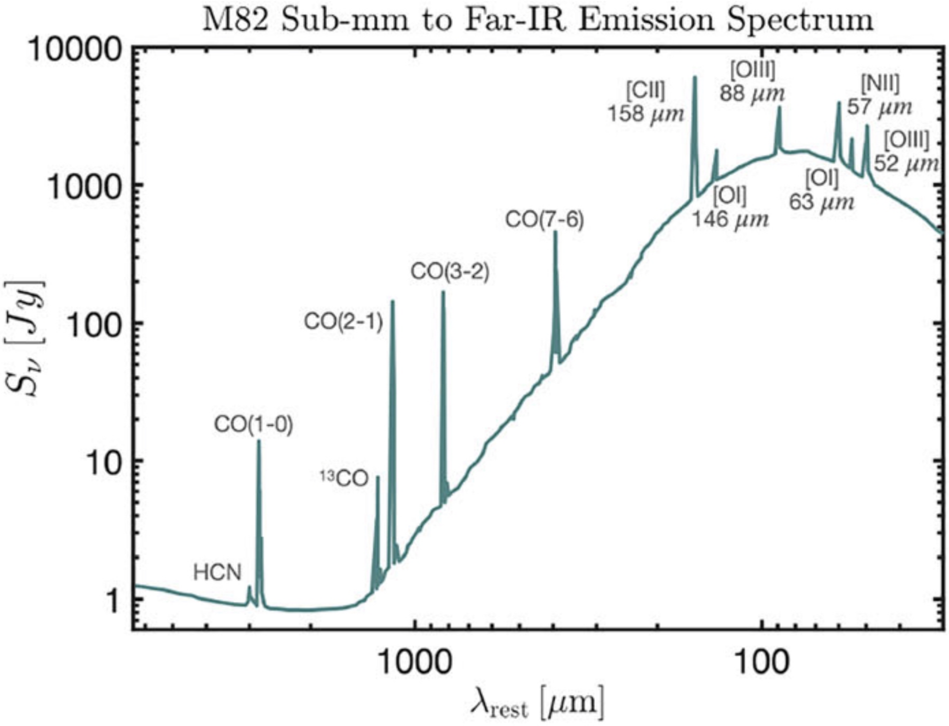

Figure 1.10: Model emission spectrum of the starburst galaxy M82 in the rest-frame far-infrared. Bright emission lines such as [C II], [N II] and various CO transitions are shown on the top of dust continuum. These lines are valuable for high-redshift observations, to trace the molecular gas and probe the ISM. Figure from Wilson et al. (2006).

UV/optical for exploring properties of distant galaxies. Each of these lines originates from unique species and conditions. For instance Lyα comes from neutral hydrogen; Hα and Hβ are hydrogen recombination lines, crucial for measuring star formation rates (Kennicutt, 1998b) and dust extinction. [O II] and [O III] are forbidden lines arising from ionized oxygen which are valuable for measuring gas density, metallicity, and identifying AGN (Baldwin et al., 1981; Kauffmann et al., 2003; Moustakas et al., 2006).

Far-infrared emission lines are a powerful probe of the ISM in high-redshift galaxies. They are crucial because the rest-frame UV/optical lines such as Hα, Hβ, [O III] λ4959, 5007Å, [O II] λ3726, 3729Å, and [N II] λ6548, 6584Å, commonly used to trace ISM conditions (Kennicutt, 1998a; Kewley & Dopita, 2002; Brinchmann et al., 2004; Tremonti et al., 2004; Moustakas et al., 2010), only probe ionised gas and are redshifted into the infrared. On the other hand, far-infrared lines such as those from carbon monoxide (CO), neutral atomic carbon ([C I]), ionized carbon ([C II]), and ionized nitrogen ([N II]) trace the neutral ISM and are within the observational capabilities of facilities like ALMA. These lines are less affected by dust extinction and sit on top of the thermal dust continuum (Figure 1.10).

Rotational transitions of CO trace molecular hydrogen (Young & Scoville, 1991; Solomon & Vanden Bout, 2005; Narayanan et al., 2012; Bolatto et al., 2013; Carilli & Walter, 2013), the fuel for star formation. Lower-J lines such as CO(1–0) (2601μm; 115 GHz) and CO(2–1) (1300μm; 230 GHz) probe cold, diffuse gas, while higher-J lines like CO(3–2) (867μm; 346 GHz) and CO(4–3) (650μm; 461 GHz) trace warmer, denser regions (Carilli & Walter, 2013; Hodge & da Cunha, 2020). Neutral atomic carbon lines, [CI] $^3P_1 \rightarrow {}^3P_0$ at 609μm and [CI] $^3P_2 \rightarrow {}^3P_1$ at 370μm, arise from photodissociation regions (PDRs) and trace the transition region between molecular and ionized gas. [C I] offers complementary insights to CO into molecular gas clouds and UV radiation fields in star-forming regions. The [C II] 158μm (singly ionized carbon) line is one of the brightest far-infrared lines and can originate from PDRs, HII regions, and diffuse ionized gas due to its low ionization potential. It is one of the key tracers of star formation and ISM dynamics, however its interpretation needs caution due to the [C II] deficit and changing ISM conditions in distant galaxies (Laporte et al., 2019; Carniani et al., 2020; Harikane et al., 2020). The [N II] (singly ionized nitrogen) lines at 122μm and 205μm complement [C II] by tracing ionized gas in HII regions, probing electron density and metallicity (Lee et al., 2019; Fudamoto et al., 2025; Kolupuri et al., 2025). [C II] and [N II] lines, along with other far-infrared lines, provide crucial insights into galaxy evolution over cosmic time. They enable detailed investigation of gas content, kinematics, star formation, and chemical composition, especially when UV-optical tracers are not accessible.

1.5 Lyα emitters

Lyα emission is produced when an electron in a hydrogen atom makes a transition from the $n = 2$ to $n = 1$ energy level, which results in the release of a photon at 1216 Å in the UV part of the spectrum. In galaxies, Lyα emission predominantly originates from the recombination of ionized hydrogen within HII (ionized hydrogen) regions. Here, intense UV radiation, arising from either young, massive O and B-type stellar populations or powerful emission from AGN, ionizes the surrounding neutral hydrogen gas. Subsequently, free electrons recombine with protons and cascade through energy levels to the ground state, resulting in the emission of Lyα (Dijkstra et al., 2006; Hummer & Storey, 1987). Another important way Lyα photons are produced is through collisional excitation (Fite & Brackmann, 1958; Fite et al., 1959). In this process neutral hydrogen atoms in warm gas (around 10^4 K) are excited by collisions with electrons or other particles, triggering electron transitions to the $n = 2$ level and subsequently Lyα emission. This process is dominant in star-forming regions and shocked gas, such as in outflows or supernova remnants.

The brightness of Lyα makes it an effective means of surveying the distant Universe and it is used in both spectroscopic (Dawson et al., 2004; Rhoads et al., 2004; Curtis-Lake et al., 2012; Liu & Jiang, 2023; Witstok et al., 2025) and narrowband photometric studies (e.g. Tilvi et al., 2010; Shibuya et al., 2012; Konno et al., 2014; Matthee et al., 2015; Santos et al., 2016; Ota et al., 2017; Sobral et al., 2018; Hu et al., 2019; Wold et al., 2022) to efficiently identify distant galaxies known as Lyα emitters (LAEs). LAEs are young, generally low-mass, star-forming galaxies characterised by their strong Lyα emission. With the introduction of JWST, LAEs have now been detected at redshifts beyond $z > 10$, e.g. Figure 1.11 shows an LAE observed at $z = 13.05$ (Witstok et al., 2025).

1.5.1 LAE sample used in this thesis

We utilise the sample of ∼4000 LAEs in the COSMOS field (∼2 deg^2) from the SC4K survey (Sobral et al., 2018). The SC4K survey used deep narrow- and medium-band imaging obtained from the Subaru and the Isaac Newton telescopes

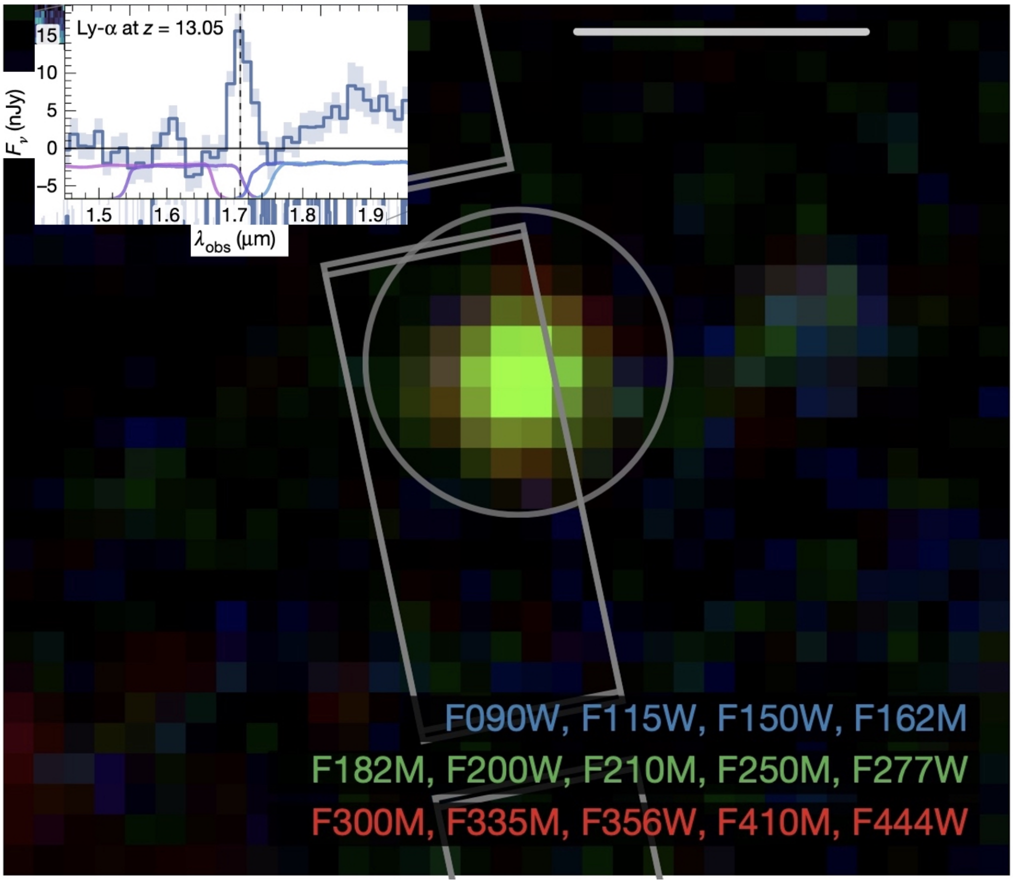

Figure 1.11: False-colour image of the LAE JADES-GS-z13-1-LA, observed at redshift $z = 13.05$ by Witstok et al. (2025) using JWST. This image is constructed by stacking different NIRCam filters and assigning them red, green and blue colours as shown. The scale bar indicates a physical size of 1kpc. This observation at such a high redshift demonstrates the importance of the Lyα emission line for observing distant galaxies. The overlay shows the Lyα spectrum of the LAE. Figure adapted from Witstok et al. (2025).

and identified LAEs based on their narrow-band excess, covering a Lyα luminosity range of $\log_{10}(L_{\mathrm{Ly}\alpha}/\mathrm{erg\,s^{-1}}) = 42.06$ to 44.54. This survey uses 12 medium and 4 narrow bands, spread across 16 redshift slices from $z = 2$ to 6. The LAE selection includes a cut in observed equivalent width (EW) EW $> 50 \times (1+z)$ Å and utilizes low-resolution ($R \sim 20$–80) observations of Lyα line emission. Starting with 40726 potential line emitters, SC4K's colour criteria (Lyman break blueward of the excess and rejection of very red Balmer-break interlopers) combined with visual inspection, remove artefacts, edge effects and halos, leaving a total of 3,908 LAEs. After this step, they identified and flagged AGN (314; $\sim 8\%$) by cross-matching with the Chandra X-ray and VLA radio catalogues. Their LAE selection criteria generally favours galaxies where Lyα emission dominates over the continuum, so galaxies with strong stellar continuum but weak Lyα are missed. Furthermore, AGN can enhance Lyα detectability by both producing additional Lyα beyond star-formation and facilitating the escape of Lyα by ionizing the surrounding neutral hydrogen. This introduces a selection bias favouring galaxies in which Lyα emission dominates over the continuum and AGN host LAEs. SC4K provides an insight into the LAEs from the end of the epoch of re-ionization ($z \sim 6$) to the peak of star formation history ($z \sim 2$). Santos et al. (2020) derived stellar masses for these LAEs using spectral energy distribution (SED) modelling, finding masses spanning a range of $\log_{10}(M_\star/M_\odot) = 7.84$ to 11.91, covering a diverse population of galaxies. The sample includes SED-driven properties such as UV absolute magnitude ($-20.28 > M_{\mathrm{UV}} > -24.84$) and UV continuum slope ($-1.93 > \beta_{\mathrm{UV}} > -2.44$) from Santos et al. (2020) derived using SED fitting. β_{UV} was estimated using MAGPHYS, which imposes a lower limit on the UV slope ($\beta_{\mathrm{UV}} = -2.44$). The M_{UV} is calculated by integrating over the rest frame UV range (λ_0=1400–1600 Å).

1.5.2 The Lyα escape fraction

The escape of Lyα photons from a galaxy is influenced by resonant scattering from neutral hydrogen in the interstellar medium (ISM; Neufeld, 1991; Hansen & Oh, 2006; Smith et al., 2022), and the proliferation of the photons to our telescopes is also affected by the circumgalactic and intergalactic mediums (Dijkstra et al., 2007; Jeeson-Daniel et al., 2012; Mesinger et al., 2015; Gurung-López et al., 2020), and Lyα is susceptible to absorption by dust grains, since the dust grain size is comparable to the Lyα wavelength (Atek et al., 2008; Hayes et al., 2011; Matthee et al., 2016). The Lyα line can also be energised by AGN (Miley & De Breuck, 2008), further complicating the interpretation of the detection of Lyα from distant systems. Multiwavelength studies are therefore used to characterise LAEs and provide insight into the subset of the population, which may only be easily detected in Lyα (e.g., Nilsson et al., 2007; Otí-Floranes et al., 2012).

A key parameter is the Lyα escape fraction, $f_{\text{esc}}(\text{Ly}\alpha)$ – the ratio of observed to intrinsic Lyα emission – which is required to determine the intrinsic properties of LAEs from the observed Lyα. $f_{\text{esc}}(\text{Ly}\alpha)$ can be determined by using other measurements to predict the intrinsic Lyα luminosity. For instance, the Lyα to Hα ratio is expected to be ~ 8.7 under case B recombination conditions (Baker & Menzel, 1938), so a lower observed ratio indicates the scattering or attenuation of Lyα photons. This method has been used in a number of studies (e.g. Sobral et al., 2018; Matthee et al., 2021; Melinder et al., 2023; Ning et al., 2023; Roy et al., 2023); for instance Matthee et al. (2016) used it to show that LAEs at $z \approx 2$, have a wide range of $f_{\text{esc}}(\text{Ly}\alpha)$ (2–30%), with a median of ∼1.6%, which decreased for galaxies with higher star formation rates and dust attenuation. A similar method uses the Lyα to Hβ ratio (e.g. Erb et al., 2019; Saxena et al., 2023), which is predicted to be ∼23 under case B recombination conditions. Using this method Weiss et al. (2021) observed mean $f_{\text{esc}}(\text{Ly}\alpha)$ ∼6% at $z \sim 2$, with values again decreasing with increasing stellar mass. There is also an observed correlation between Lyα equivalent width (EW) and $f_{\text{esc}}(\text{Ly}\alpha)$ (e.g. Verhamme et al., 2017; Harikane et al., 2018; Sobral & Matthee, 2019), which Sobral & Matthee (2019) utilized and found $f_{\text{esc}}(\text{Ly}\alpha) > 24\%$. To avoid the impact of dust attenuation, which can reduce the apparent Hα and Hβ fluxes (Vale Asari et al., 2020), Calhau et al. (2020) compared observed Lyα luminosities with radio-continuum derived SFRs for LAEs, finding median $f_{\text{esc}}(\text{Ly}\alpha) = 50 \pm 20\%$.

Whilst dust attenuation affects the derivation of $f_{\text{esc}}(\text{Ly}\alpha)$ from Hα, Hβ and Lyα lines, studies are also impacted by the intrinsic faintness of Hβ, which is difficult to detect. Furthermore, the correlation between Lyα EW and $f_{\text{esc}}(\text{Ly}\alpha)$ is only calibrated for $z \leq 2.6$ and EW ≤ 160 Å. In addition, the derivation of

$f_{\rm esc}({\rm Ly}\alpha)$ from radio emission depends on the calibration between radio continuum and SFR, which can be significantly affected by AGN contamination (Bourne et al., 2011; Delhaize et al., 2017; Molnár et al., 2018). Thus, $f_{\rm esc}({\rm Ly}\alpha)$ remains poorly constrained due to the combined effects of dust attenuation, resonant scattering by neutral hydrogen, and the complex radiative transfer processes within the ISM and CGM. Since, Lyα is predominantly generated in star-forming regions, an alternative is to calculate the total star-formation rate of a galaxy and use this to predict the intrinsic Lyα luminosity in the calculation of $f_{\rm esc}({\rm Ly}\alpha)$ (e.g. Wardlow et al., 2014). Far-infrared emission from dust provides insight into dust-obscured SFR. Combining this with UV-based SFR measurements provides a total SFR. These methods complement each other and eliminate the need to apply dust attenuation corrections to the UV-based SFR, which rely on assumptions that are not yet well-constrained for LAEs. By utilising this method, Wardlow et al. (2014) and Kusakabe et al. (2015) determined $f_{\rm esc}({\rm Ly}\alpha) \geq 10\%$, which is higher than the global $f_{\rm esc}({\rm Ly}\alpha)$ at the same epoch (Hayes et al., 2011; Konno et al., 2016).

1.5.3 Dust in LAEs

LAEs are expected to be dust-poor because their stellar populations are young, and therefore their stars have not had enough time to evolve and enrich the ISM with significant amounts of dust through supernovae or AGB evolutionary phases (Finkelstein et al., 2009). However, the ISM can be enriched by short lived O and B type massive stars (Hirashita et al., 2015), with the Lyα on some lines of sight being completely absorbed by dust, but others being free from dust allowing the Lyα photons to escape. Indeed, for intermediate to high redshift galaxy populations it is increasingly being shown that dust and Lyα emission can co-exist especially if the dust is clumpy or unevenly distributed (Haiman & Spaans, 1999; Scarlata et al., 2009; Oteo et al., 2012). Furthermore, spectroscopic follow-up of the first galaxies detected at submillimetre wavelengths with the Submillimetre Common-User Bolometer Array (SCUBA) on the James Clerk Maxwell Telescope (JCMT; e.g., Chapman et al., 2003), unexpectedly showed Lyα emission highlighting a potential connection between dust and Lyα. This

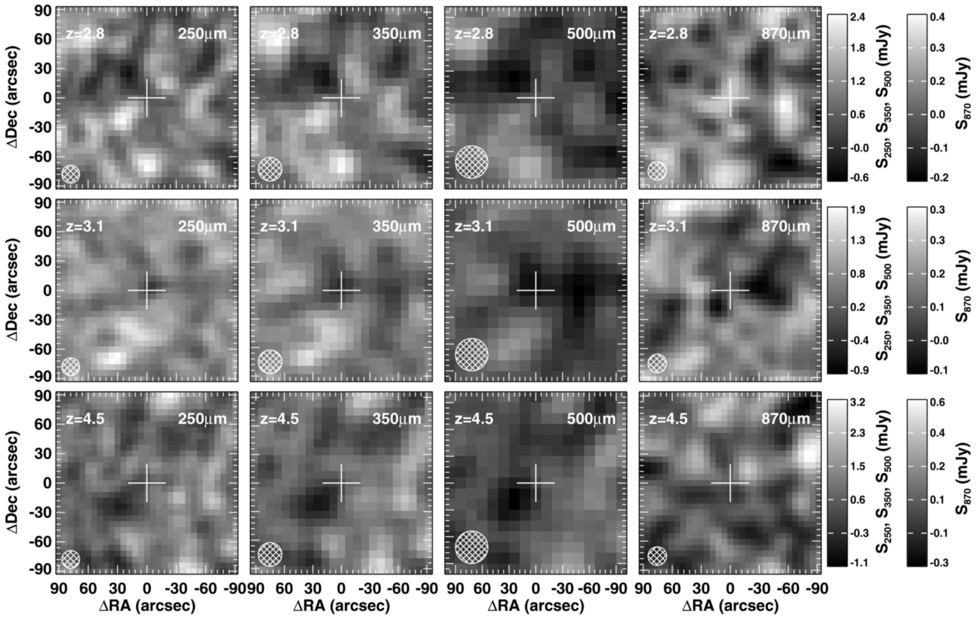

Figure 1.12: Stacks of *Herschel* 250, 350, and 500 μm data from the HerMES survey and 870 μm data from the LABOCA ECDFS Submillimeter Survey for 126, 280, and 92 LAEs at $z = 2.8$, 3.1, and 4.5, respectively. No $\geq 3\sigma$ detections are identified, in any of the stacks . Figure from Wardlow et al. (2014).

connection has been further strengthened by observations from Swinbank et al. (2005); Li et al. (2019). Therefore, to accurately estimate the dust correction and total SFR it is important to account for regions that are completely optically-thick at UV and optical wavelengths.

Until now, the limited availability of deep far-infrared data has led to a dearth of studies targeting far-infrared emission from LAEs. Single-dish far-infrared and submillimetre telescopes offer wide-field imaging capabilities but are hampered by high confusion limits due to their large beam sizes, e.g. the *Herschel*/SPIRE beam is $\sim 18''$ at 250 μm (Griffin et al., 2010) and at 850 μm JCMT/SCUBA-2 has a $\sim 14.6''$ beam (Holland et al., 2013). Interferometers like ALMA can deliver deeper data, but have narrow fields-of-view, which makes it observationally expensive to survey large samples of faint sources (e.g., Ota et al., 2014; Williams et al., 2014). Instead, stacking can be used. For example, Wardlow et al. (2014) attempted to detect dust emission to measure $f_{\rm esc}({\rm Ly}\alpha)$ from ~ 500 LAEs at $z = 2.8$–4.5 using

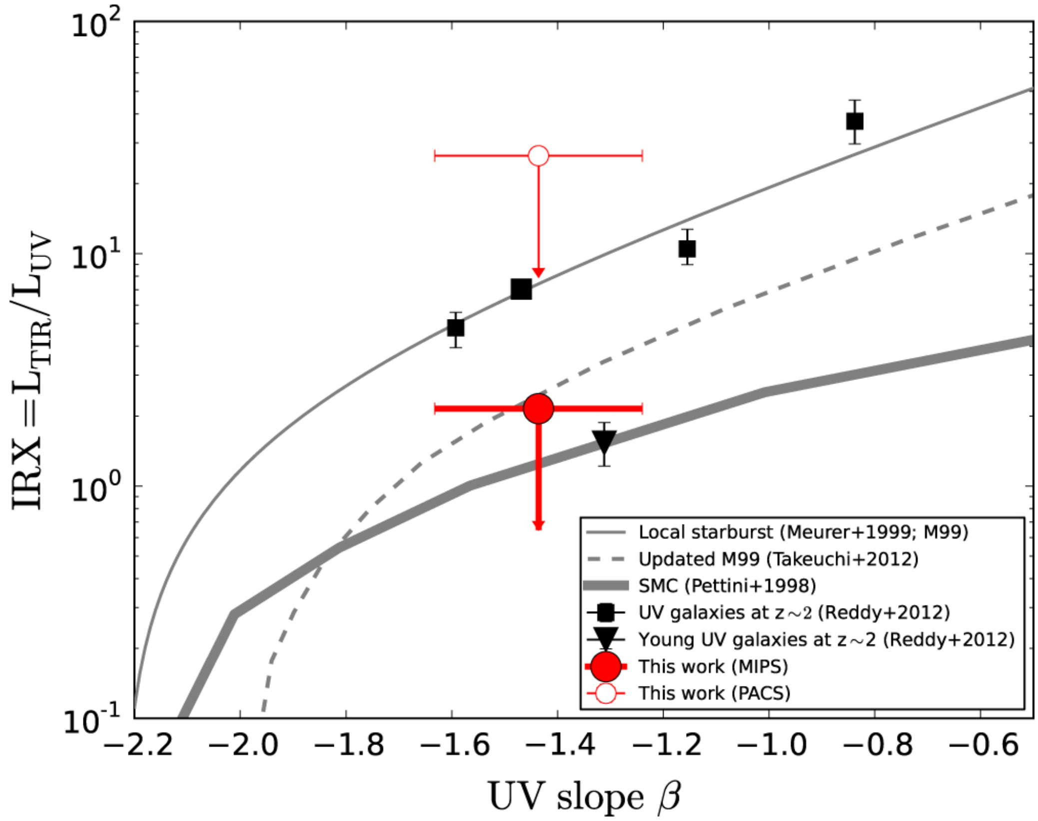

Figure 1.13: The IRX (L_{IR}/L_{UV}) as a function of the UV slope, β_{UV}. Red filled and open circles show limits from stacking 213 LAEs at $z \simeq 2.18$ in *Spitzer*/MIPS and *Herschel*/PACS data, respectively. Black symbols indicate UV-selected galaxies. Curves represent empirical dust attenuation laws for star-forming galaxies. Figure from Kusakabe et al. (2015).

Herschel and LABOCA data. They did not detect any individual galaxies and stacks of samples in three redshift bins reached a maximum of 2.8σ, leading to limits of $f_{\rm esc}({\rm Ly}\alpha) \gtrsim 10\%$: slightly higher than the global $f_{\rm esc}({\rm Ly}\alpha)$ evolution at the targeted redshifts. Similarly, Kusakabe et al. (2015) stacked *Spitzer*/MIPS and *Herschel*/PACS observations of 213 LAEs at $z \simeq 2.18$ in GOODS-South, leading to an estimate of the average $f_{\rm esc}({\rm Ly}\alpha)$ of 16–37%, which is also higher than the cosmic average at the same epoch.

1.5.4 The IRX–$\beta_{\rm UV}$ relation in LAEs

When infrared data is not directly available the most widely used method to correct galaxy measurements (e.g. UV luminosities, star formation rates, or stellar masses) for dust attenuation in the rest-frame UV/optical uses the relationship between the infrared excess (IRX=$\rm L_{IR}/L_{UV}$) and ultraviolet spectral slope ($\beta_{\rm UV}$; see e.g. Meurer et al. 1999; Calzetti et al. 2000; Gordon et al. 2003; Reddy et al. 2018). While the IRX-$\beta_{\rm UV}$ relation has been extensively studied in UV-selected galaxies such as Lyman Break Galaxies (LGBs; e.g., Capak et al., 2015; Álvarez-Márquez et al., 2016; Bouwens et al., 2016; Barisic et al., 2017; Bowler et al., 2018; Koprowski et al., 2018; Fudamoto et al., 2020), the placement of LAEs in this plot is still unclear. Since LAEs are faint in the far-infrared, direct measurements of the IRX are challenging. As a result, only upper limits on their infrared excess have been established (e.g., Kusakabe et al., 2015, Figure 1.13), leaving uncertainties in how dust affects the observed properties of LAEs and how they compare to other distant galaxy populations. Sensitive far-infrared telescopes such as ALMA and SCUBA-2 on the JCMT, provide the opportunity to directly observe dust emissions from LAEs. This enables testing of the applicability of the IRX–$\beta_{\rm UV}$ relation for LAEs.

1.6 This Thesis

This study explores the dust and gas content in $\sim$4000 Lyα emitters (LAEs) at redshift z = 2–6 from the SC4K survey in the COSMOS field (Sobral et al., 2018) utilizing observations from powerful far-infrared telescopes. We use 850μm observations from the JCMT, 100–500μm data from the *Herschel* space telescope, and various observations from ALMA to examine dust continuum emission and trace molecular gas through far-infrared spectral lines, including atomic and CO lines.

In Chapter 2, we present dust continuum detections in LAEs based on single-dish observations from *Herschel* and JCMT. We describe the stacking methodology developed to detect average dust emission from various LAE sub-samples. Furthermore, we perform SED fitting on individual detections and upper limits, providing a detailed characterization of their dust-inferred properties. To build on this, Chapter 3 describes our dust detections that are available with deeper, higher-resolution ALMA observations. We also present our results on constraining the IRX–β_{UV} relation for LAEs, facilitated by these deeper ALMA observations. Chapter 4 focuses on infrared spectroscopy which we use to estimate the molecular gas content in LAEs from far-infrared atomic and CO line observations from the ALMA archive. In Chapter 5, we summarize our key findings and discuss future research directions to better understand how dust, gas, and star formation are linked in these young, distant galaxies. Throughout this study, we assume a flat Universe with ΛCDM cosmology and utilize a Chabrier initial mass function (IMF; Chabrier, 2003).

Chapter 2

Measuring dust in LAEs using single-dish observations

2.1 Introduction

LAEs are young, star-forming galaxies identified by strong Lyα emission. Although they are typically observed in the UV/optical, which traces unobscured star formation, detecting their dust emission is important to understand a complete picture of their SFR, dust content, and overall evolution. While LAEs are generally considered dust-poor, as supported by previous non-detections (e.g., Wardlow et al., 2014; Kusakabe et al., 2015), this assumption needs to be tested with deeper, more sensitive observations from telescopes like JCMT/SCUBA-2 and *Herschel*. Observations from these single-dish far-infrared telescopes can play a valuable role in investigating the dust properties of LAEs. These facilities may enable statistical detections of dust emission via techniques like stacking due to their wide field of view and new, large samples of LAEs.

In this study, we use 100, 160, 250, 350, 500 and 850 μm continuum observations from *Herschel*/PACS, *Herschel*/SPIRE and JCMT/SCUBA-2 to investigate the dust emission from ~ 4000 LAEs at $z = 2.2$–6 from the SC4K survey (Sobral et al., 2018) of the COSMOS field. We search for dust emission from individual LAEs and use stacking analyses to measure the average infrared fluxes from LAEs that are too faint to be individually detected. These results are used to probe $f_{\rm esc}({\rm Ly}\alpha)$ and the IRX-$\beta_{\rm UV}$ relation for LAEs. We target this redshift range because the reionization process is believed to be complete at $z \sim 6$ (Becker et al., 2001; Mesinger, 2010; McGreer et al., 2015; Cain et al., 2021). Beyond redshift 6, the presence of neutral hydrogen in IGM is expected to rise, which can potentially affect Lyα observations. Additionally, the amount of dust is expected to decrease beyond redshift 6, which makes detection of LAEs at far-infrared wavelengths more challenging. Furthermore, the global star formation rate density (SFRD) peaks at $z \sim 2$ (Hopkins & Beacom, 2006; Schaye et al., 2010; Madau & Dickinson, 2014) and it correlates with the dust content (Santini et al., 2014; McKinnon et al., 2017; Magnelli et al., 2020) which implies that LAEs within our target redshift range are more likely to be detected in the far-infrared wavelength range.

The chapter is organized as follows: in Section 2.2, we discuss the LAE sample and the far-infrared data. Section 2.3 outlines the flux measurement and stacking methods employed in this analysis. Spectral energy distributions (SEDs), escape fractions and the IRX-$\beta_{\rm UV}$ relation are discussed in Section 2.4 and our conclusions are presented in Section 2.5. Throughout this work, we adopt ΛCDM cosmology with $H_0 = 69.3\,{\rm km s^{-1}\,Mpc^{-1}}$, $\Omega_{\rm M} = 0.29$, and $\Omega_\Lambda = 0.71$ (Hinshaw et al., 2013) and apply a Chabrier (Chabrier, 2003) initial mass function (IMF).

Table 2.1: Properties of LAEs that are individually detected in the submillimetre data.

Source ID[a]	z	S_{100}[b] (mJy)	S_{160}[b] (mJy)	S_{250}[b] (mJy)	S_{350}[b] (mJy)	S_{500}[b] (mJy)	S_{850}[b] (mJy)	$\log_{10}(L_{\rm IR})$[c] ($L_\odot$)	SFR$_{\rm FIR}$[c] ($M_\odot$ yr^{-1})	SFR$_{\rm UV}$[d] ($M_\odot$ yr^{-1})	SFR$_{\rm Ly\alpha}$[d] ($M_\odot$ yr^{-1})	$f_{\rm esc}({\rm Ly}\alpha)$[d]
SC4K-IA505-178627[g]	3.09[e]	1.2±0.5	3.6±1.2	7.0±1.6	10.4±2.8	11.1±3.2	3.7±1	$12.5^{+0.1}_{-0.1}$	360^{+40}_{-50}	35±4	$27.6^{+0.7}_{-0.7}$	$0.07^{+0.01}_{-0.01}$
SC4K-IA574-34828[g]	3.61	7.3±3.0	10.5±4.3	17.1±3.6	0.0±0.0[f]	15.6±8.3	5.5±1.4	$13.0^{+0.1}_{-0.1}$	1090^{+220}_{-220}	10±1	$7.1^{+1.0}_{-0.9}$	$0.01^{+0.00}_{-0.00}$
SC4K-IA484-28746[g]	2.98	3.1±1.8	16.7±2.2	18.5±3.5	0.00±7.5	6.1±4.8	3.7±0.9	$12.9^{+0.1}_{-0.1}$	970^{+120}_{-280}	11±1	$14.0^{+0.5}_{-0.6}$	$0.01^{+0.00}_{-0.00}$
SC4K-IA484-69327	2.92	6.4±2.1	13.4±9.5	0.8±5.0[f]	34.0±10.3	21.2±7.4	4.5±1.2	$13.0^{+0.1}_{-0.1}$	1110^{+260}_{-250}	106±12	$52.9^{+0.6}_{-0.6}$	$0.04^{+0.01}_{-0.01}$
SC4K-IA679-223923[g]	4.63[e]	2.4±1.7	14.3±4.1	7.4±1.8	12.4±2.1	16.1±3.4	3.9±1.2	$13.1^{+0.1}_{-0.1}$	1250^{+220}_{-200}	7±1	$10.9^{+1.4}_{-1.5}$	$0.01^{+0.00}_{-0.00}$

[a] Source IDs are from SC4K (Sobral et al., 2018). [b] Flux densities at 100–500 μm are from the *Herschel* PACS and SPIRE super-deblended catalogue (Jin et al., 2018) and for 850 μm are from the deblended Simpson et al. (2019) catalogue. [c] IR luminosities (L$_{\rm FIR}$) and SFRs (SFR$_{\rm FIR}$) are derived in Section 2.4.1. [d] UV and Lyα-derived SFRs and the calculation of $f_{\rm esc}({\rm Ly}\alpha)$ are described in Section 2.4.2. [e] LAEs with spectroscopic redshifts from Hasinger et al. (2018); DESI Collaboration et al. (2024); all other redshifts are from the detection of Lyα in medium- and narrow-band photometry (Sobral et al., 2018). [f] These values are excluded from SED fitting due to being inconsistent with the other photometry for the same source (Section 2.4.1). [g] The LAE is also detected with ALMA (Chapter 3) and the difference in $L_{\rm IR}$ value (up to ~0.6 dex) is likely due to the different SED fitting methods used.

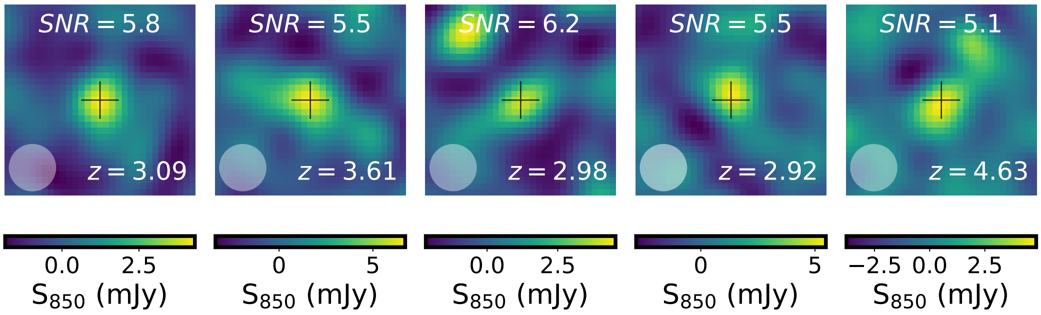

Figure 2.1: 62 × 62 arcsec SCUBA-2 850 μm cutouts at the positions of the five individually detected LAEs with the redshifts and SNR of each SCUBA-2 detection labelled. LAE positions are marked by black crosses and white circles indicate the size of the 14.6 arcsec SCUBA-2 beam.

2.2 Data

Since LAEs are expected to be faint at far-infrared wavelengths this work requires a large sample of LAEs in an area with deep submillimeter observations. We therefore focus on the Cosmic Evolution Survey (COSMOS; Scoville et al., 2007), the most extensive Hubble Space Telescope (HST) survey designed to probe galaxy formation and evolution across cosmic time.

2.2.1 LAE Sample

We begin by considering the 3908 LAEs identified by SC4K (Sobral et al., 2018) in deep narrow- and medium-band observations of $\sim 2\,\mathrm{deg}^2$ of COSMOS. SC4K identified LAEs at $z \sim 2.2$–6 in 16 redshift slices (based on the narrow- and medium-band filters) and with observed Lyα EW $> 50(1+z)$ Å. Our analyses require parameters derived from spectral energy distribution (SED) fitting, which was performed by Santos et al. (2020) using MAGPHYS (da Cunha et al., 2008). We exclude the 261 SC4K LAEs that are flagged as having "bad" SED fits (Santos et al., 2020), leaving a sample of 3674 LAEs that are studied here.

2.2.2 Far-infrared data

2.2.2.1 *Herschel* PACS and SPIRE

The whole COSMOS field was mapped by *Herschel* with both the PACS and SPIRE instruments. In this study we use *Herschel*/PACS 100 and 160 μm data from the public release of the PACS Evolutionary Probe (PEP, Lutz et al. 2011) and *Herschel*/SPIRE 250, 350 and 500 μm data from the Herschel Multi-tiered Extragalactic Survey (HerMES; Oliver et al. 2012) that has been reprocessed by the Herschel Extragalactic Legacy Project (HELP; Shirley et al. 2021).

The PACS maps have a pixel scales of 1.2 and 2.4 arcsec and point spread functions (PSFs) of 7.2 and 12 arcsec, respectively, and reach depths of $\sigma_{100} = 1.50$ and $\sigma_{160} = 3.27$ mJy. The SPIRE maps have pixel scales of 6, 8.3 and 12 arcsec and beams of 18.15, 25.15, and 36.30 arcsec at 250, 350 and 500 μm, respectively. The noise levels are $\sigma_{250} = 3.18$, $\sigma_{350} = 2.66$ and $\sigma_{500} = 3.82$ mJy in COSMOS (Oliver et al., 2012; Shirley et al., 2021).

Examination of the distribution of pixel values show that the median values of the SPIRE maps are slightly negatively offset, which would artificially decrease flux densities derived from stacking unless corrected. We thus correct flux measurement by adding the flux offsets of 1.62, 1.65 and 1.3 mJy to each pixel of 250, 350 and 500 μm maps respectively.

2.2.2.2 SCUBA-2 850 μm

To probe longer wavelengths we use JCMT/SCUBA-2 850 μm data from S2COSMOS (Simpson et al., 2019), which reaches a median noise level of $\sigma_{850} = 1.2$ mJy and has a pixel scale of 2 arcsec. The 14.6 arcsec resolution map is centred on the COSMOS field and covers $\sim 2.6\,\mathrm{deg}^2$.

The standard S2COSMOS map has been processed with a matched filter, which helps to detect individual sources, but introduces negative rings around bright sources (Simpson et al., 2019). Thus, LAEs that are situated in the negative regions in the match-filtered map would systematically add negative flux when stacking. To prevent these negative rings in the match-filtered map from artificially reducing any stack signals, we instead work from a version of the

S2COSMOS map that has not been match filtered (Simpson et al., 2019), which we process using 2D Gaussians to replicate the S2COSMOS match-filtering process but without the negative PSF wings. The map is first convolved with a 30 arcsec FWHM Gaussian and this convolved map is subtracted from the original in order to filter out large-scale residual noise. We then convolve the resulting map with a 9.6 arcsec FWHM 2D Gaussian such that the resulting image has the same 14.6 arcsec PSF as the instrument and the S2COSMOS match-filtered map. Finally, a flux conversion factor (FCF) is estimated by comparing the flux densities of bright sources in our Gaussian-smoothed map with the same sources in the match-filtered images. Applying this FCF leads to our final corrected map, which has the same PSF and source flux densities as the S2COSMOS match-filtered map but without the negative rings around bright sources.

2.3 Flux Measurement

2.3.1 Individual detections

To examine dust properties of individual LAEs, we begin by determining whether any of the SC4K LAEs are individually detected in the S2COSMOS data. To accomplish this, we cross-match the positions of SC4K sources to the S2COSMOS catalogue (Simpson et al., 2019) and find 31 matches within 7 arcsec (i.e. the radius of the SCUBA-2 850 μm beam). We visually inspect these 31 sources using archival imaging from *Hubble*, Subaru, UKIRT and *Spitzer* (e.g. *Hubble* (Scoville et al., 2007), Subaru (Taniguchi et al., 2015), UKIRT (Lawrence et al., 2007), *Spitzer* (Sanders et al., 2007)) to identify systems for which the multiwavelength data supports the probability that the 850 μm emission is associated to an LAE position. Of the 31 individual matches, we confirm five individual LAEs are detected in S2COSMOS, and there are an additional four LAEs that likely blended with nearby sources in 850 μm map. The five LAEs with 850 μm emission are all within 3 arcsec of the corresponding S2COSMOS source (Figure 2.1) and the four blended LAEs are matched to within 4.5 arcsec.

The five individually 850-μm detected LAEs are shown in Figure 2.1 and Table 2.1. They are at detected at 5.1–6.2σ and are at $z \sim 2.92$–4.63 and we take their 850 μm flux densities from the S2COSMOS catalogue (Simpson et al., 2019), which accounts for deboosting. For these five LAEs we use SC4K LAE positions to extract *Herschel* PACS and SPIRE fluxes from the publicly accessible super-deblended COSMOS catalogue (Jin et al., 2018), wherein the far-infrared emission has been deblended to align with optical-NIR coordinates. All five of these LAEs that are bright enough to be individually-detected in submillimetre data are X-ray and/or radio-detected AGN hosts (Calhau et al., 2020) with Lyα luminosities $> 10^{42.8}\,\mathrm{erg\,s^{-1}}$. Figure 2.2 shows that both the individual detections and three of four likely blended LAEs contain X-ray and/or radio AGN and that they are more luminous in Lyα than the SC4K sample as a whole. It is therefore possible that the Lyα and/or infrared emission from these systems may include a contribution from the AGN, though this is uncertain (see e.g. Calhau et al. 2020).

2.3.2 Stacking

Since most LAEs are not bright enough in the far-IR to be individually detected in the SCUBA-2 and *Herschel* observations, we next use stacking to probe the average dust emission from this population. Stacking a number of sources, N, reduces background noise by a factor of $\sqrt{N}$, so stacking the whole population of ~ 4000 SC4K LAEs enables the measurement of emission $\sim 60\times$ deeper than is possible for individual systems. We exclude the five individually detected and four blended LAEs (Section 2.3.1) from all stacks so as to avoid these potential outliers from biasing the results.

We write a bespoke Python stacking code, which produces cutouts of the PACS, SPIRE and SCUBA-2 maps described in Section 2.2.2 at the positions of the SC4K LAEs. These are then median combined to determine the median flux of the LAEs that are included in each stack. The size of the stacks is scaled to the beam size at each wavelengths, such that we produce median stacks that are $\sim 37'' \times 37''$, $74'' \times 74''$, $150'' \times 150''$, $208'' \times 208''$, $300'' \times 300''$ and $62'' \times 62''$ for the 100, 160, 250, 350, 500 and 850 μm median stacks, respectively.

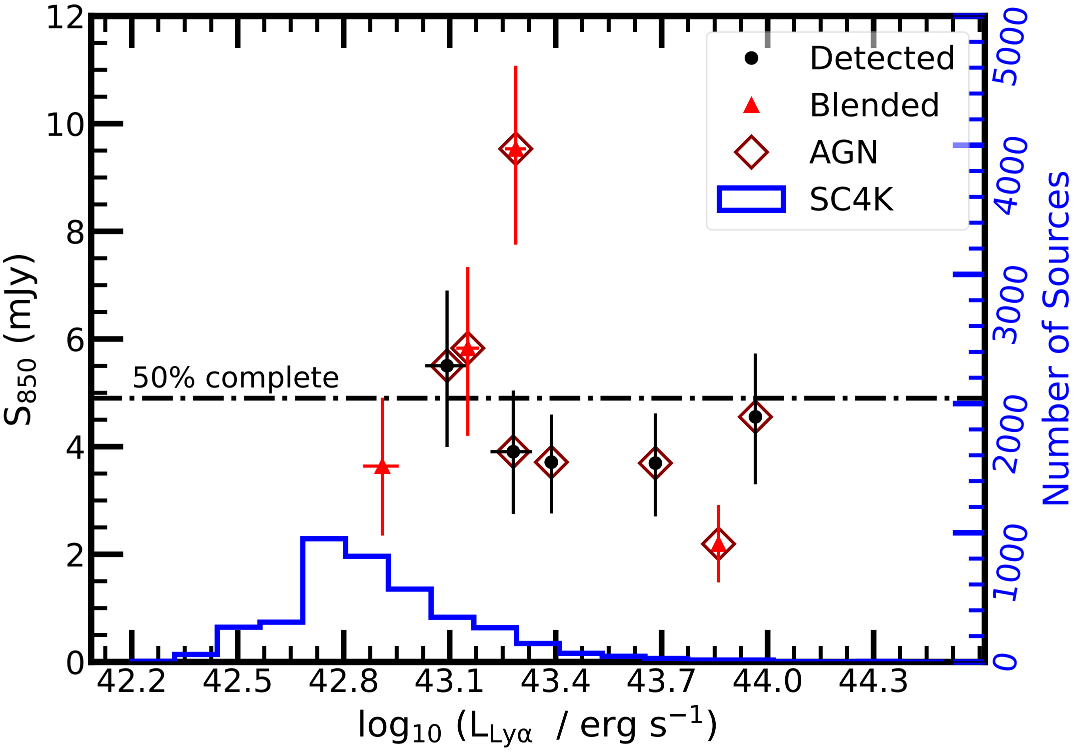

Figure 2.2: 850 μm flux densities and Lyα luminosities of the five LAEs that are individually-detected in the submillimetre, compared with the S2COSMOS 50% completeness limit and the distribution of Lyα luminosities of the whole SC4K catalogue (right-hand axis). The four blended sources are also shown and those with X-ray and/or radio detections indicative of AGN activity are highlighted. The LAEs that are bright enough in the far-IR to be individually-detected in S2COSMOS tend to be more Lyα luminous than the whole LAE population and they are more likely to host X-ray or radio AGN.

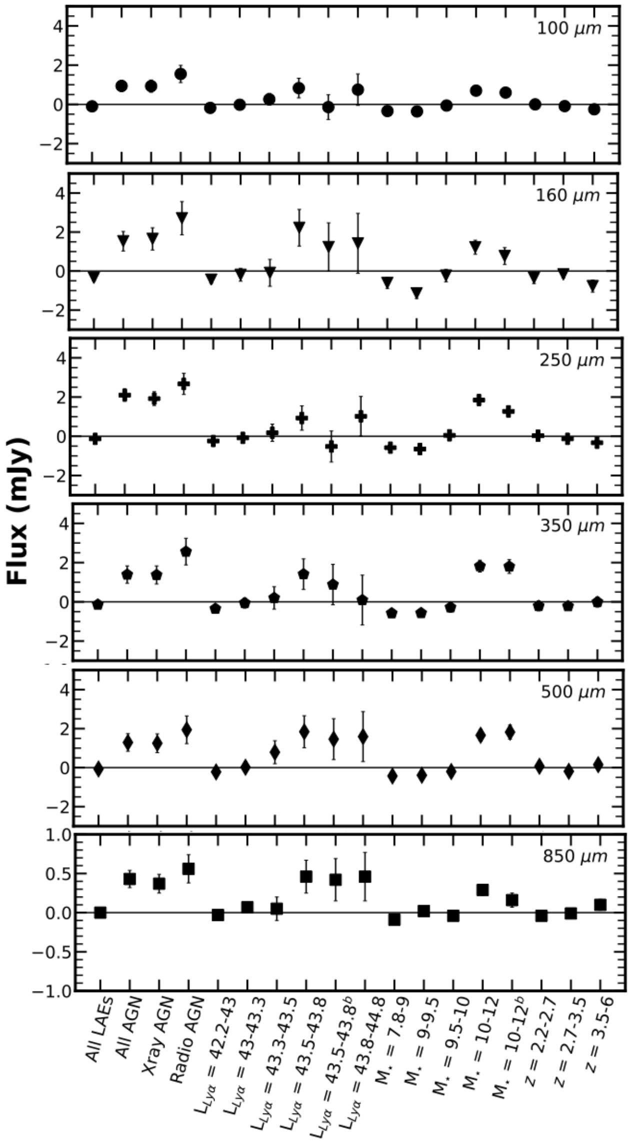

Figure 2.3: The far-infrared flux densities at 100, 160, 250, 350, 500 and 850 μm, measured from our stacks of all SC4K LAEs and different sub-samples. Each panel presents results from a different wavelength and with datapoints representing each stacked subset. 1σ uncertainties are indicated by the error bars, which demonstrates that at all wavelengths the stacks of all LAEs, and the samples split by Lyα luminosity and redshift are undetected at the 3σ level. However $\geq 3\sigma$ signals are observed in the stacks of all AGN, X-ray AGN, radio AGN and high stellar mass ($M_\star = 10^{10-12}\ M_\odot$) populations at most wavelengths. Even when AGN are excluded stacks of the most massive LAEs (i.e. $M_\star = 10^{10-12}\ M_\odot$, excluding AGN) have a 2.9σ signal at 100 μm and are detected at $\geq 4\sigma$ signals at 250, 350 and 500 μm. Lyα luminosities and stellar mass ranges are given in log format and the superscript ^{b} indicates subsets from which AGN are excluded. All stacks exclude the five individually detected and four blended LAEs (Section 2.3.1).

To verify the astrometric alignment between the far-infrared datasets we first stack the *Herschel* and SCUBA-2 maps at the positions of publicly available *Spitzer*/MIPS (Frayer et al., 2009) and VLA 3 GHz (Smolčić et al., 2017) selected sources, which are expected to be bright in the far-infrared (e.g., Ivison et al., 2008; Lee et al., 2010; Biggs et al., 2011). These *Spitzer* and VLA stacks reveal robustly detected signals that are centered in the 62×62 arcsec^2 cutouts in all six *Herschel* and SCUBA-2 datasets, which demonstrates the power of stacking and confirms astrometric alignment between the datasets.

2.3.2.1 Stacked photometry

The *Herschel*/PACS maps are in units of Jy/pixel and we therefore use PSF aperture photometry as described in Santos et al. (2020) and Lutz et al. (2011) and centred at the centre of each stack. Apertures that match the PSF size i.e. 7.2 and 12 arcsec at 100 and 160 μm, respectively are used, with background annuli extending from 2 to 3× further than this. To ensure accuracy in flux measurement, an aperture correction of a factor of 1.49 is applied to both measurements, along with a filter correction factor of 1.2 for 100 μm and 1.1 for 160 μm stacks (Popesso et al., 2012; Balog et al., 2014).

SPIRE maps are instead in units of mJy/beam, wherein for unresolved sources (as expected for high redshift galaxies), the brightest pixel gives the total flux. Therefore, to determine the flux from 250, 350 and 500 μm stacks, we verify that the brightest pixel is at the centre of the maps and use the value of this pixel as the stacked flux.

The S2COSMOS maps are also in units of mJy/beam and therefore the brightest pixel contains all the flux for a point source. However, in this case the brightest pixel is not always the central pixel – likely due to small uncertainties between the Lyα and dust emission regions combined with SCUBA-2 pixel scale and beam size. We visually inspect the individual LAE cutouts that contribute to the stack and verify that the offsets are not driven by a bias in a directional offset of a some bright sources, but are instead due to randomisation amongst all LAEs.

Extracting robust flux densities from the SCUBA-2 maps requires first identifying the brightest pixel within the central stacked pseudo-source i.e. excluding noisy pixels near the edges of the stack cutout. For this we use a two step process to identify the brightest pixel within a SCUBA-2 beam size centre of the stack that is driven by emission from within (and not outside of) this region. This two step process is required to ensure that the outskirts of non-central noise peaks are not inadvertently selected in cases where there is no significant LAE detection. Having first identified the brightest pixel within a beam size of the centre (p_1) we next identify the brightest pixel within a beam size of this first pixel (p_2). If both $p_1 = p_2$ then we can be confident that any flux at p_1 is driven by the overlapping LAEs in the stack, and p_1 therefore provides the stacked flux density. If $p_1 \neq p_2$ then we take the value of the pixel at the centre of the stack as the measure of the flux density, though in this case the stack is likely undetected (i.e. SNR < 3). This procedure is repeated in the process of measuring photometric uncertainties. To calculate the uncertainty in the flux density of the far-infrared stacks we select random positions in the SC4K coverage region, with masking to avoid bright stars and artefacts. The number of random positions used is set equal to the number of LAEs included in each stack (Table 2.2). We then stack the far-IR data at these random positions and measure the flux densities for each dataset as described above. This random stacking process is repeated 1000 times for each stacked dataset and the standard deviation of the flux density of these 1000 random stacks provides the uncertainty on the corresponding LAE stack. We have confirmed that the medians of these distributions are consistent with 0 mJy, as expected for random positions.

Table 2.2: 100–850 μm flux densities (mJy) measured for stacks of different subsets of SC4K LAEs.

Sample	# Sources^{a}	Median z	$S_{100}{}^{c}$	$S_{160}{}^{c}$	$S_{250}{}^{c}$	$S_{350}{}^{c}$	$S_{500}{}^{c}$	$S_{850}{}^{c}$
All LAEs	3674	2.99	-0.1±0.08	-0.35±0.15	-0.13±0.09	-0.14±0.12	-0.07±0.12	0.0±0.03
All AGN	298	2.99	0.94±0.28	1.53±0.5	2.1±0.32	1.39±0.44	1.29±0.45	0.43±0.11
X-ray AGN	240	2.99	0.93±0.31	1.65±0.57	1.92±0.35	1.37±0.46	1.25±0.48	0.37±0.12
Radio AGN	108	2.99	1.55±0.44	2.71±0.85	2.67±0.54	2.56±0.68	1.94±0.71	0.56±0.18
Lyα Luminosity (erg s^{-1})								
$42.2 < \log_{10}(\mathrm{L}_{\mathrm{Ly}\alpha}) \leq 43.0$	2639	2.99	-0.18±0.09	-0.44±0.18	-0.24±0.11	-0.35±0.14	-0.22±0.15	-0.03±0.04
$43.0 < \log_{10}(\mathrm{L}_{\mathrm{Ly}\alpha}) \leq 43.3$	748	3.33	-0.02±0.17	-0.19±0.33	-0.08±0.21	-0.06±0.26	0.02±0.28	0.07±0.07
$43.3 < \log_{10}(\mathrm{L}_{\mathrm{Ly}\alpha}) \leq 43.5$	170	4.12	0.26±0.3	-0.09±0.69	0.18±0.44	0.2±0.57	0.79±0.59	0.05±0.15
$43.5 < \log_{10}(\mathrm{L}_{\mathrm{Ly}\alpha}) \leq 43.8$	83	3.33	0.83±0.50	2.22±0.94	0.93±0.62	1.41±0.78	1.84±0.82	0.46±0.21
$43.5 < \log_{10}(\mathrm{L}_{\mathrm{Ly}\alpha}) \leq 43.8^{b}$	50	4.58	-0.14±0.63	1.23±1.24	-0.52±0.79	0.88±1.03	1.46±1.05	0.42±0.27
$43.8 < \log_{10}(\mathrm{L}_{\mathrm{Ly}\alpha}) \leq 44.8$	33	3.12	0.75±0.8	1.42±1.54	1.02±1.01	0.09±1.27	1.59±1.28	0.46±0.31
Stellar Mass ($M_{\odot}$)								
$7.8 < \log_{10}(\mathrm{M}_{\star}) \leq 9.0$	1047	2.99	-0.34±0.15	-0.61±0.28	-0.58±0.17	-0.58±0.21	-0.43±0.23	-0.09±0.06
$9.0 < \log_{10}(\mathrm{M}_{\star}) \leq 9.5$	1115	2.99	-0.36±0.14	-1.14±0.27	-0.65±0.17	-0.57±0.22	-0.39±0.23	0.02±0.06
$9.5 < \log_{10}(\mathrm{M}_{\star}) \leq 10.0$	843	3.16	-0.06±0.16	-0.23±0.32	0.05±0.20	-0.28±0.25	-0.2±0.26	-0.04±0.06
$10.0 < \log_{10}(\mathrm{M}_{\star}) \leq 12.0$	669	3.16	0.7±0.19	1.22±0.36	1.85±0.22	1.82±0.30	1.66±0.30	0.29±0.07
$10.0 < \log_{10}(\mathrm{M}_{\star}) \leq 12.0^{b}$	461	3.33	0.6±0.21	0.77±0.43	1.27±0.28	1.80±0.35	1.82±0.36	0.16±0.09
Redshift (z)								
$2.2 < z \leq 2.7$	876	2.50	0.0±0.15	-0.35±0.29	0.03±0.19	-0.21±0.25	0.07±0.26	-0.04±0.06
$2.7 < z \leq 3.5$	2139	3.16	-0.09±0.10	-0.17±0.18	-0.13±0.12	-0.22±0.16	-0.19±0.16	-0.01±0.04
$3.5 < z \leq 6.0$	659	4.82	-0.25±0.16	-0.77±0.31	-0.33±0.19	-0.01±0.26	0.15±0.28	0.1±0.07

[a] Number of LAEs included in each stack. [b] LAEs containing radio and/or X-ray AGN are excluded from these stacks. [c] Flux densities at 100–850 μm in mJy.

2.3.2.2 Stacking Results

We stack the whole population of LAEs, and also separately stack LAEs with radio and/or X-ray AGN, as well as subsets that are binned by Lyα luminosity, stellar mass and redshift. The binning scheme from Calhau et al. (2020) is adopted, such that our results can be directly compared with the Calhau et al. (2020) X-ray stacks. The subsets are listed in Table 2.2 along with their median stacked flux densities in the 100–850 μm data. Figure 2.3 displays these measurements graphically and Figure 2.4 shows example stacks including all LAEs, LAEs that contain AGN, LAEs with $\log_{10}(\mathrm{L_{Ly\alpha}}/\mathrm{erg\,s^{-1}}) = 43.5$–$43.8$, those with stellar mass $\log_{10}(\mathrm{M_\star}/\mathrm{M_\odot}) = 10$–$12$ (both including and excluding AGN) and those at $z = 3.5$–6.

We do not detect far-infrared emission from the population of all 3674 LAEs as a whole, suggesting that their median flux density is < 0.24 mJy, < 0.27 mJy, and < 0.09 mJy (3σ) at 100, 250, and 850 μm, respectively. Most of the other stacks are also undetected at all targeted wavelengths, and upper limits will be used for these throughout our analyses (Section 2.4). However, the LAEs that contain AGN or are the most massive are detected at most of the targeted far-IR wavelengths i.e. these are the LAEs that contain the most dust, as shown in Figure 2.3 and Table 2.2. The second brightest bin of Lyα luminosity (i.e. with $\log_{10}(\mathrm{L_{Ly\alpha}}/\mathrm{erg\,s^{-1}}) = 43.5$–$43.8$) is undetected at 100, 250 and 350 μm, but has tentative signals at the 2.7, 2.2 and 2.2σ levels at 160, 500 and 850 μm, respectively. This bin contains $\sim 2.5\times$ more LAEs than the highest luminosity bin and therefore reaches $\sim 1.6\times$ deeper, so these results are consistent with Lyα luminosity also being a driver of far-IR emission in LAEs.

Since AGN are more common in the most massive and most Lyα-luminous LAEs (Calhau et al., 2020) we next exclude AGN and repeat the stacking procedure for the different subsets. As expected, subsets that were not previously detected remain undetected when AGN are excluded. The 50 LAEs with $\log_{10}(\mathrm{L_{Ly\alpha}}/\mathrm{erg\,s^{-1}}) = 43.5$–$43.8$ that are not AGN are not detected when stacked, even when combined with the brightest non-AGN LAEs, which increases the sample to 59 and improves the sensitivity. After removing AGN, the stack of the most

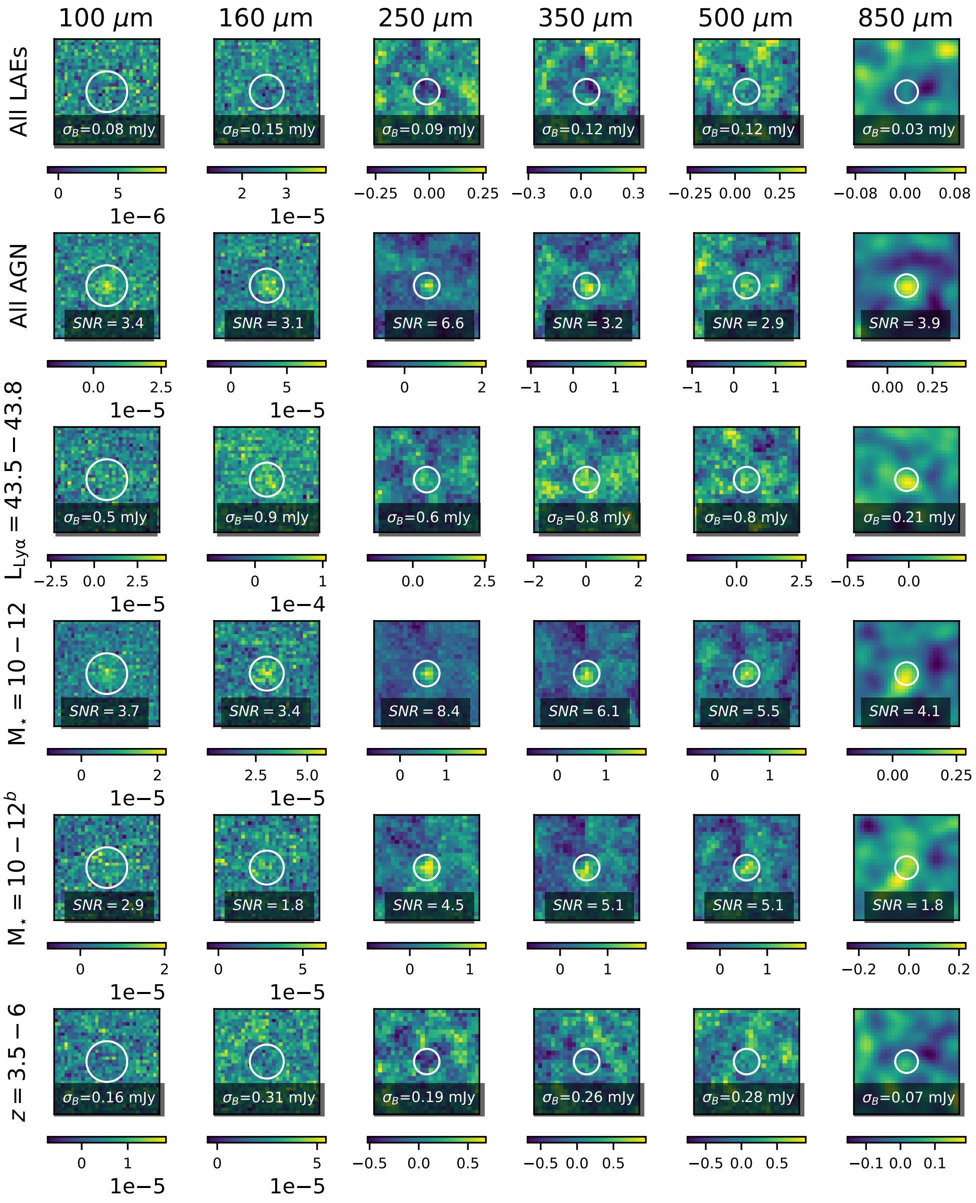

Figure 2.4: Images of six of our median stacks. Rows correspond to different subsets (labelled on the left) and columns show the different wavelengths (labelled at the top). From top to bottom, the example stacks show and those for are all LAEs, all LAEs that contain AGN, LAEs with $\log_{10}(\mathrm{L}_{\mathrm{Ly}\alpha}/\mathrm{erg\,s}^{-1}) = 43.5$–$43.8$, those with $\log(\mathrm{M}_\star/\mathrm{M}_\odot) = 10$–$12$ and those in the same mass bin but with AGN excluded (denoted by ^{b}), and those at $z = 3.5$–6. Colour bars are showing flux density in Jy for PACS and in mJy for the other stacks. White circles are located at the centres of the stacks and represent the beam sizes at the relevant wavelength. The sizes of the cutouts are discussed in Section 2.3.2. For subsets that are detected at $\geq 3\sigma$ in ≥ 3 bands the labels give the signal-to-noise ratio (SNR); for samples that are predominantly not detected in out stacks the background noise level is instead given.

massive LAEs is detected at 4.5, 5.1 and 5.1σ at 250, 350 and 500 μm, respectively, and has a tentative 2.9σ signal at 100 μm. This suggests that both AGN and stellar mass drive the far-infrared emission from LAEs.

2.4 Results And Discussion

2.4.1 SED Fitting

Having identified far-IR emission from some individual LAEs and measured median flux densities from LAE stacks, we next use SED fitting to quantify the dust emission from these galaxies. For the five individually-detected LAEs the photometry used is presented in Table 2.1 and for stacks we use the detections and limits given in Table 2.2. Where possible we employ spectroscopic redshifts (Hasinger et al., 2018) with narrow/medium-band constrained SC4K photometric redshifts (Sobral et al., 2018) used otherwise. For stacked samples the median redshift of the included sources is used (Table 2.2).

Different methods of SED fitting are used depending on whether or not the system is detected at $\geq 3\sigma$ in ≥ 2 wavelengths. For those stacks or sources that are undetected or only detected in one band we use the SWIRE Sd galaxy and M82 SED templates (Polletta et al., 2007) to constrain the far-infrared luminosity. These SED templates are scaled to the 3σ flux density upper limit at 850 μm (which, relative to the SEDs, is the deepest of the datasets; Figure 2.5) at the redshift of the individual LAE or the median redshift value of the stack. The Sd and M82 templates are chosen because they cover the full range of effective dust temperatures in SWIRE, and therefore encompass the range of plausible infrared luminosities. For systems that have multiple $\geq 3\sigma$ detections the SED fitting code MONTE CARLO INFRARED SPECTRAL ENERGY DISTRIBUTION (MCIRSED; Casey 2012; Drew & Casey 2022) is used. MCIRSED has six free parameters as standard, but since we have a maximum of six photometric points we reduce the number of degrees of freedom by fixing the emissivity index ($\beta_{\rm IR}$) to $\beta_{\rm IR} = 1.5$ and setting the mid-infrared power-law slope (α) to $\alpha = 2.0$. We tested the effect of

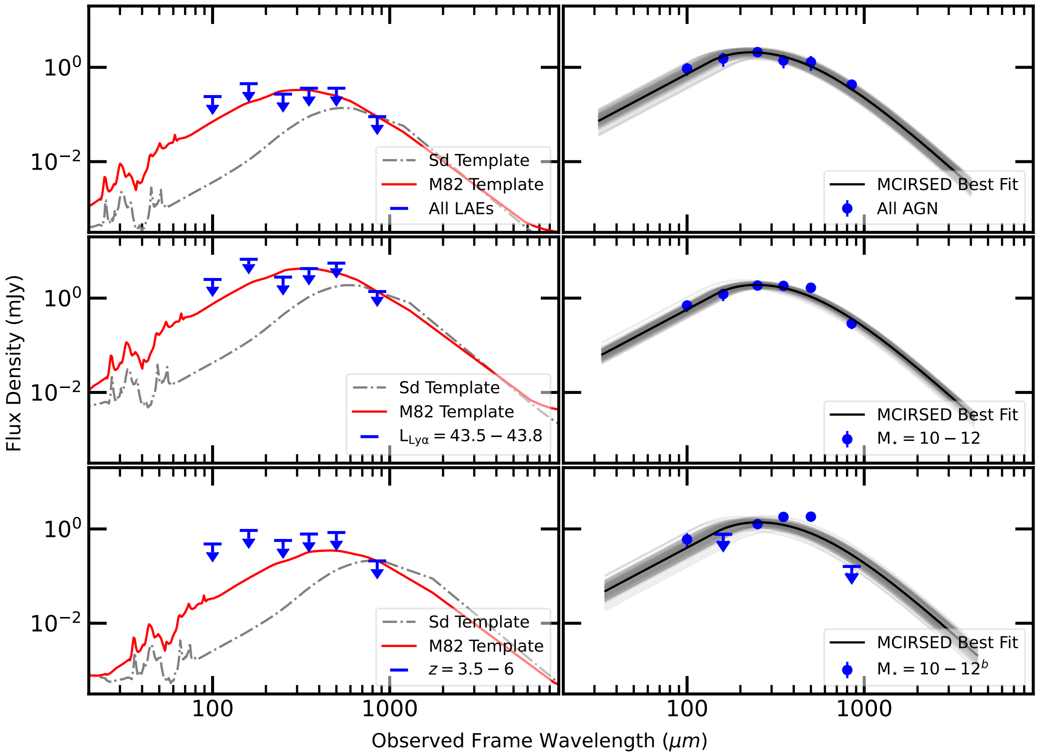

Figure 2.5: Far-infrared SEDs for key stacks from Table 2.2. The left-hand column shows stacks that are undetected at all bands, overlaid with the SWIRE Sd and M82 templates (Polletta et al., 2007) that provide upper limits on the infrared luminosities. The right-hand column shows stacks that have ≥ 2 detections and are fit with MCIRSED as described in Section 2.4.1. For these SEDs the black line represents the best fit, while the gray lines show 100 other less probable fits sampled from the MCMC posterior distribution. Upper limits are plotted at the 3σ level. The left-hand panels show, from top to bottom, stacks of all SC4K LAEs, those with $L_{Ly\alpha} = 10^{43.5-43.8}$ erg s^{-1}, and those at $z = 3.5 - 6$. In the right-hand column the stacks of all LAEs containing radio and/or X-ray AGN, the most massive LAEs ($M_\star = 10^{10-12}\ M_\odot$) and the most massive LAEs excluding those that contain AGN (depicted by ^{b}). The SEDs demonstrate the range of infrared luminosities probed by the Sd and M82 templates, the robustness of the stacked flux densities and the quality of the MCIRSED fits. An SED fit that goes through the 3σ upper limits is nearly ruled out by the data, so care must be taken, as the SED is expected to remain strictly below the 3σ upper limits.

not fixing α and β_{IR} and find no significant differences in the derived far-infrared luminosities, but significantly increased uncertainty on these parameter.

For the MCIRSED fits (i.e. individual LAE and stacks with ≥ 2 bands with $\geq 3\sigma$ detections) the SED fitting is performed using the measurements in all detected bands and we include the measured values (and uncertainties) for any remaining band(s) that have $\geq 2.5\sigma$ signals. For any values that are below the 2.5σ level we show the 2.5σ noise as an upper limit. These upper limits are not included in the SED fitting; they are shown only to illustrate the sensitivity (or non-detection) at those wavelengths. For the LAEs SC4K-IA574-34828 and SC4K-IA484-69327 the catalogued ~ 0 mJy flux densities at 350 μm and 250 μm, respectively, are inconsistent with other photometry for these sources (Table 2.1) and we therefore exclude these data from the SED fits. MCIRSED and SWIRE template-based SEDs for key stacks are presented in Figure 2.5. From the SED fits described above we estimate the rest-frame 8–1000 μm far-infrared luminosities ($\mathrm{L_{FIR}}$), including 3σ upper limits for LAE stacks that are not detected in *Herschel* or SCUBA-2. The SED-derived far-infrared properties of the five individually-detected LAEs are presented in Table 2.1. Table 2.3 presents results for the stacked data.

We next derive dust-obscured SFRs ($\mathrm{SFR_{FIR}}$) for the LAEs and stacks using the relationship between infrared luminosity and SFR from Kennicutt (1998b) which is given in Equation 2.1:

$$\mathrm{SFR_{FIR}}(\mathrm{M_{\odot}\ yr^{-1}}) = 1.09 \times 10^{-10} \mathrm{L_{FIR}}(\mathrm{L_{\odot}}) \tag{2.1}$$

Equation 2.1 assumes a Salpeter (1955) IMF, so we multiply the resulting SFRs by a factor of 0.63 to scale them to a Chabrier (2003) IMF. For systems that are not detected in the infrared Equation 2.1 is used to calculate the 3σ upper limit on the obscured SFR.

The far-infrared luminosities of individually-detected LAEs are all in the ULIRG range with $\mathrm{L_{FIR}} = 10^{12.5}$ to $10^{13.1}\,L_{\odot}$, corresponding to obscured SFRs of 360–1250 $M_{\odot}\,\mathrm{yr}^{-1}$ (assuming no AGN contribution to the infrared fluxes). The average far-infrared luminosities of the subsets of LAEs that are detected in the stacks are slightly lower, in the range $10^{11.9}$ to $10^{12.3}\,L_\odot$, corresponding to far-infrared-based SFRs of 100–190 $M_\odot\,\mathrm{yr}^{-1}$. LAEs that are in stacks that are not detected are fainter and have 3σ upper limits of $\mathrm{L_{FIR}} < 10^{10.4}$ to $10^{12.3} L_\odot$, equivalent to $\mathrm{SFR_{FIR}} \leq 3$–$230\,M_\odot\,\mathrm{yr}^{-1}$. In previous studies, Wardlow et al. (2014) stacked $z = 2.1$–4.5 LAEs at SPIRE and SCUBA-2 wavelengths, and Kusakabe et al. (2015) stacked $z = 2.23$ LAEs at PACS and MIPS wavelengths. These studies constrained the average emission of LAEs at these redshifts to $\mathrm{L_{FIR}} < 10^{10.04}\,L_\odot$ and $\mathrm{L_{FIR}} \lesssim 10^{11}\,L_\odot$ (depending on the redshift and assumed SED) for Kusakabe et al. (2015) and Wardlow et al. (2014), respectively. Our measurements are consistent with these results, giving e.g. $\mathrm{L_{FIR}} \lesssim \times 10^{11.4}\,L_\odot$ for $z = 2.2$–2.7 LAEs scaled to the M82 template and $\mathrm{L_{FIR}} \lesssim \times 10^{11.1}\,L_\odot$ for all SC4K LAEs and the same template.

These results demonstrate that most LAEs are faint in the infrared, with obscured SFRs at the level of 10s of $M_\odot\,\mathrm{yr}^{-1}$ or lower. Nevertheless, some LAEs can be infrared-luminous, and these are typically those that are massive or that contain AGN.

Table 2.3: Average far-infrared properties of different groups of LAEs derived from SED fitting to our stacked data. Limits are at the 3σ level and the two values are derived using the Sd (first value) and M82 (second value) SED templates.

Sample	# Sources[a]	Median z	$\log_{10}(L_{\rm IR})$[c] ($L_\odot$)	SFR$_{\rm FIR}$[d] ($M_\odot$ yr^{-1})	SFR$_{\rm UV}$[e] ($M_\odot$ yr^{-1})	SFR$_{\rm Ly\alpha}$[f] ($M_\odot$ yr^{-1})	$f_{\rm esc}({\rm Ly}\alpha)$[g]
All LAEs	3674	2.99	≤10.4, ≤11.1	≤3, ≤15	4±1	$4.1^{+0.6}_{-0.6}$	≥0.59, ≥0.21
All AGN	298	2.99	$12.1^{+0.1}_{-0.1}$	120^{+20}_{-20}	6±1	$6.4^{+0.6}_{-0.6}$	$0.05^{+0.01}_{-0.01}$
X-ray AGN	240	2.99	$12.1^{+0.1}_{-0.1}$	120^{+20}_{-20}	7±01	$6.9^{+0.7}_{-0.6}$	$0.05^{+0.01}_{-0.01}$
Radio AGN	108	2.99	$12.3^{+0.1}_{-0.1}$	190^{+40}_{-40}	6±1	$7.1^{+0.5}_{-0.6}$	$0.04^{+0.01}_{-0.01}$
Lyα Luminosity (erg s^{-1})							
$42.2 < \log_{10}(L_{\rm Ly\alpha}) \leq 43.0$	2639	2.99	≤10.5, ≤11.3	≤ 4, ≤20	3±1	$3.5^{+0.6}_{-0.6}$	≥0.48, ≥0.15
$43.0 < \log_{10}(L_{\rm Ly\alpha}) \leq 43.3$	748	3.33	≤10.8, ≤11.5	≤7, ≤40	7±2	$7.6^{+0.7}_{-0.6}$	≥0.55, ≥0.18
$43.3 < \log_{10}(L_{\rm Ly\alpha}) \leq 43.5$	170	4.12	≤11.2, ≤11.8	≤20, ≤70	10±2	$13.4^{+1.0}_{-0.9}$	≥0.48, ≥0.16
$43.5 < \log_{10}(L_{\rm Ly\alpha}) \leq 43.8$	83	3.33	≤11.6, ≤12.3	≤50, ≤230	17±4	$22.8^{+0.5}_{-0.5}$	≥0.36, ≥0.09
$43.5 < \log_{10}(L_{\rm Ly\alpha}) \leq 43.8$[b]	50	4.58	≤11.5, ≤12.1	≤30, ≤130	15±3	$21.8^{+1.6}_{-1.4}$	≥0.45, ≥0.15
$43.8 < \log_{10}(L_{\rm Ly\alpha}) \leq 44.8$	33	3.12	≤11.4, ≤12.1	≤30, ≤160	40±10	$51.1^{+1.2}_{-1.2}$	≥0.76, ≥ 0.27
Stellar Mass ($M_\odot$)							
$7.8 < \log_{10}(M_\star) \leq 9.0$	1047	2.99	≤10.7, ≤11.4	≤10, ≤30	3±1	$3.4^{+0.6}_{-0.6}$	≥0.42, ≥0.11
$9.0 < \log_{10}(M_\star) \leq 9.5$	1115	2.99	≤10.7, ≤11.4	≤10, ≤30	5±1	$4.2^{+0.6}_{-0.6}$	≥0.41, ≥0.12
$9.5 < \log_{10}(M_\star) \leq 10.0$	843	3.16	≤10.7, ≤11.4	≤10, ≤30	10±1	$4.1^{+0.6}_{-0.6}$	≥0.37, ≥0.12
$10.0 < \log_{10}(M_\star) \leq 12.0$	669	3.16	$12.0^{+0.1}_{-0.1}$	120^{+15}_{-15}	7±1	$5.7^{+0.7}_{-0.6}$	$0.05^{+0.01}_{-0.01}$
$10.0 < \log_{10}(M_\star) \leq 12.0$[b]	461	3.33	$11.9^{+0.1}_{-0.1}$	100^{+20}_{-20}	7±1	$5.0^{+0.6}_{-0.6}$	$0.05^{+0.01}_{-0.01}$
Redshift (z)							
$2.2 < z \leq 2.7$	876	2.50	≤10.7, ≤11.4	≤5, ≤30	3±1	$2.5^{+0.4}_{-0.4}$	≥0.33, ≥0.08
$2.7 < z \leq 3.5$	2139	3.16	≤10.6, ≤11.3	≤5, ≤20	4±1	$4.2^{+0.6}_{-0.6}$	≥0.54, ≥0.18
$3.5 < z \leq 6.0$	659	4.82	≤10.9, ≤11.5	≤10, ≤30	9±2	$7.4^{+1.1}_{-1.1}$	≥0.40, ≥0.17

[a] Number of LAEs included in each stack. [b] LAEs containing radio and/or X-ray AGN are excluded from these stacks. [c] Rest-frame 8–1000 μm far-infrared luminosity. [d] Dust-obscured SFR, derived from the far-infrared luminosity (Section 2.4.1). [e] Unobscured SFR, derived from dust-uncorrected rest-frame UV luminosity (Section 2.4.2). [f] Apparent Lyα-derived SFR, calculated from the observed Lyα luminosity (Section 2.4.2). [g] Lyα escape fraction, calculated as described in Section 2.4.2.

2.4.2 Lyα Escape Fraction

Lyα is affected by dust attenuation and resonant scattering by neutral hydrogen, which cause the absorption and re-emission of Lyα photons at different wavelengths and in different directions. These effects make Lyα observations hard to interpret, particularly for measuring SFR, for which Lyα is often used at high redshift (e.g. Tapken et al., 2007; Otí-Floranes et al., 2014; Oyarzún et al., 2017). A key parameter is $f_{\rm esc}({\rm Ly}\alpha)$, which measures the fraction of Lyα produced to that is detected. Thus, $f_{\rm esc}({\rm Ly}\alpha)$ can be used to calculate the true Lyα emission, accounting for attenuation and scattering. Note that it is possible that the regions from which we can detect Lyα may be completely disparate from those that emit detectable infrared radiation: this is particularly probable at high-redshift, where star formation is known to be "clumpy" (e.g. Dekel et al., 2009). Therefore, to estimate the total SFR of a galaxy (and thus the Lyα production) requires the sum of both the obscured and unobscured SFR. $f_{\rm esc}({\rm Ly}\alpha)$ can then be calculated by comparing the total SFR with the SFR inferred from the Lyα luminosity as in Equation 2.2:

$$f_{\rm esc}({\rm Ly}\alpha) = \frac{{\rm SFR}_{{\rm Ly}\alpha}}{{\rm SFR}_{\rm total}} = \frac{{\rm SFR}_{{\rm Ly}\alpha}}{{\rm SFR}_{\rm UV} + {\rm SFR}_{\rm FIR}} \tag{2.2}$$

where ${\rm SFR}_{{\rm Ly}\alpha}$ is the SFR inferred from the observed (i.e. detectable) Lyα luminosity, ${\rm SFR}_{\rm total}$ is the total SFR in the galaxy, and ${\rm SFR}_{\rm UV}$ is the SFR-derived from the observed rest-frame UV emission.

${\rm SFR}_{\rm FIR}$ is calculated from our infrared observations as described in Section 2.4.1. For the UV-based SFR we use the rest-frame $\lambda_{\rm UV,0} = 1400$–$1600\,$Å UV absolute magnitude (${\rm M}_{\rm UV}$) from Santos et al. (2020), which is extracted from MAGPHYS fitting with a prior that $\beta_{\rm UV} \geq -2.44$ and has not been dust-corrected. The observed Lyα luminosity (without dust correction) is also taken from Santos et al. (2020). SFRs derived from both the Lyα luminosity (${\rm L}_{{\rm Ly}\alpha}$) and ${\rm M}_{\rm UV}$ are calculated according to Kennicutt (1998b), as given in Equations 2.3 and 2.4:

$${\rm SFR}_{{\rm Ly}\alpha}({\rm M}_\odot\ {\rm yr}^{-1}) = 5.73 \times 10^{-43} {\rm L}_{{\rm Ly}\alpha}({\rm ergs}^{-1}) \tag{2.3}$$

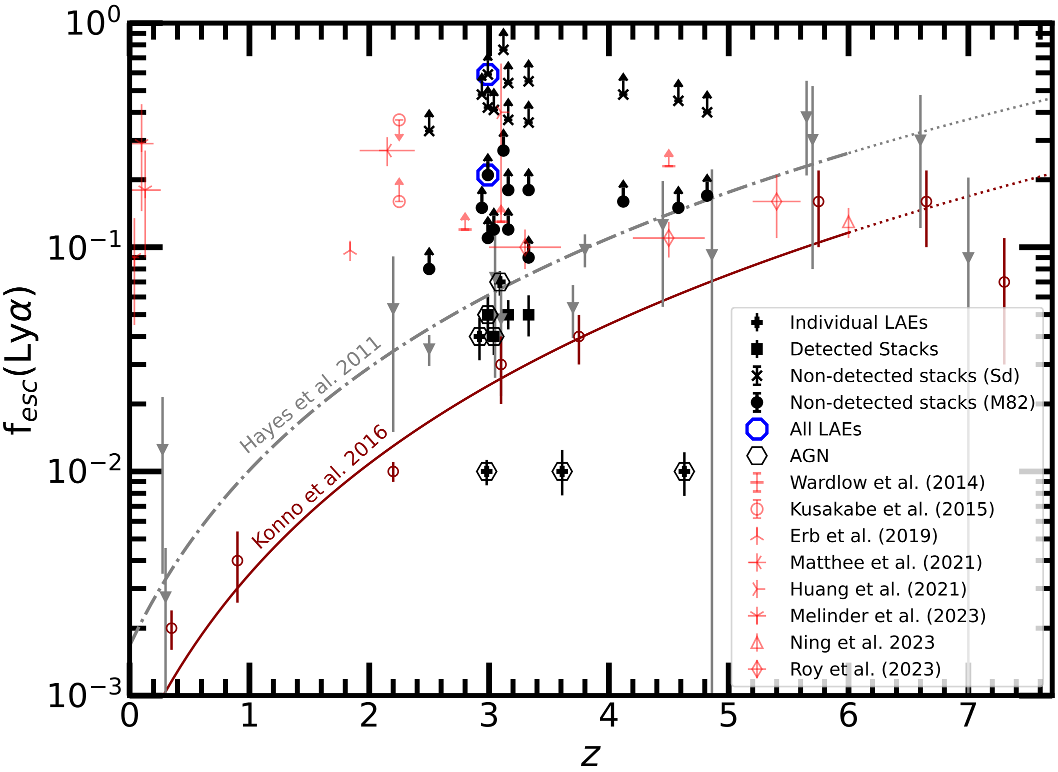

Figure 2.6: The evolution of Lyα escape fraction as a function of redshift, with our results shown in black. We highlight the results from stacking the whole SC4K catalogue and indicate LAEs containing AGN and the AGN-specific stacks. For stacks that are not detected in the infrared data we show the 3σ lower limits derived assuming both the Sd and M82 templates, where the Sd templates give higher $f_{\mathrm{esc}}(\mathrm{Ly}\alpha)$ limits for the same dataset. The grey symbols and line shows results and the fit from Hayes et al. (2011), the maroon symbols and line are the equivalent from Konno et al. (2016); dotted portions of the lines indicate our extrapolation of these fits to higher redshifts than originally studied. Red symbols represent $f_{\mathrm{esc}}(\mathrm{Ly}\alpha)$ from Wardlow et al. (2014); Kusakabe et al. (2015); Erb et al. (2019); Huang et al. (2021); Matthee et al. (2021); Melinder et al. (2023); Ning et al. (2023) and Roy et al. (2023). Directly overlapping points are shifted to left or right by Δz=0.05 to aid visibility. Where LAEs or stacks are detected in the infrared the derived $f_{\mathrm{esc}}(\mathrm{Ly}\alpha)$ are consistent with previous LAE studies and the expected global evolution. However, many of our stacks probed deeper than previous studies of $f_{\mathrm{esc}}(\mathrm{Ly}\alpha)$ and still remain undetected, which could indicate significant evolution or variety in the population and suggests that deeper studies of individual sources are required.

$$\mathrm{SFR_{UV}}(\mathrm{M_\odot\ yr^{-1}}) = 5.4 \times 10^{-8} \times 10^{-0.4\mathrm{M_{UV}}} \tag{2.4}$$

where $\mathrm{M_{UV}}$ is in AB magnitudes. As with Equation 2.1 these SFRs are based on a Salpeter (1955) IMF, so we multiply the resulting SFRs by a factor of 0.63 to scale them to a Chabrier (2003) IMF. SFRs calculated from the different tracers and the resulting $f_{\mathrm{esc}}(\mathrm{Ly}\alpha)$ are presented in Table 2.1 for the LAEs that are individually-detected in the infrared, and in Table 2.3 for the stacked data.

Figure 2.6 shows the redshift evolution of $f_{\mathrm{esc}}(\mathrm{Ly}\alpha)$ for SC4K LAEs as calculated here from single-dish submillimetre data, compared with previous studies (Wardlow et al., 2014; Kusakabe et al., 2015; Erb et al., 2019; Matthee et al., 2021; Huang et al., 2021; Melinder et al., 2023; Ning et al., 2023; Roy et al., 2023), and parametrisations of the global trend (Hayes et al., 2011; Konno et al., 2016). The Hayes et al. (2011) and Konno et al. (2016) are offset from each other due to their uses of different Lyα and UV luminosity limits in the calculation of the Lyα and UV SFR density from Lyα and UV luminosity functions.

The five LAEs that are individually-detected in the submillimetre data all have $f_{\mathrm{esc}}(\mathrm{Ly}\alpha)$ from 1 to 7%, values which are scattered on or below the global $f_{\mathrm{esc}}(\mathrm{Ly}\alpha)$ at their redshifts of $\sim$ 3–4.6 (Figure 2.6). However, we caution that all five of these LAEs contain AGN and we have assumed no AGN contribution to their far-infrared emission. If this assumption is incorrect then their true $\mathrm{SFR_{FIR}}$ will be lower than assumed (i.e. reducing the denominator in Equation 2.2), which would nominally increase the $f_{\mathrm{esc}}(\mathrm{Ly}\alpha)$. However, the Ly$\alpha$ and UV fluxes could also be boosted by the presence of an AGN, making it difficult to say if or how the $f_{\mathrm{esc}}(\mathrm{Ly}\alpha)$ would change if all effects were accounted for.

As shown in Figure 2.6, we measure $f_{\mathrm{esc}}(\mathrm{Ly}\alpha)$ of 4–5% for detected stacks (i.e. the more massive LAEs and those containing AGN), which is consistent with the global $f_{\mathrm{esc}}(\mathrm{Ly}\alpha)$ and previous studies at similar redshifts. The lower limits for undetected stacks (i.e. average SC4K LAEs, non-AGN LAEs, and less massive galaxies) are higher than this, with lower limits that are calculated assuming a Sd-like infrared SED being significantly higher than those from the M82 SED template. The limits from the M82 template are generally similar to the evolution of the global $f_{\mathrm{esc}}(\mathrm{Ly}\alpha)$ (Hayes et al., 2011; Konno et al., 2016) and some previous studies (e.g. Erb et al., 2019; Roy et al., 2023), and thus consistent with this evolution, though results for the Sd template are significantly higher, which hints that LAEs may have infrared SEDs that are warmer than that of Sd galaxies and more akin to M82-like systems. The 3σ lower limits on $f_{\rm esc}({\rm Ly}\alpha)$ from the stack of the whole LAEs sample are $\geq 21\%$ and $\geq 59\%$ assuming the Sd and M82 templates, respectively. Both values are significantly higher than the global $f_{\rm esc}({\rm Ly}\alpha)$ at comparable redshifts, which is consistent with the results from Kusakabe et al. (2015) and could indicate significant variation between LAEs (e.g. redshift evolution) such that a global average insufficiently represents the population. Matthee et al. (2021), Kusakabe et al. (2015) and Melinder et al. (2023) contain galaxies with similarly high $f_{\rm esc}({\rm Ly}\alpha)$, which supports this possibility. Deeper infrared studies of more individual LAEs are required to fully understand any such variation.

2.4.3 IRX-$\beta_{\rm UV}$ Relation

In many studies rest-frame UV/optical observations are used to measure UV luminosity and to derive parameters such as SFR. However, these photons can be absorbed by dust and thus such measurements must be corrected for dust attenuation. Whilst UV/optical measurements such as the Balmer decrement (Hα/Hβ; e.g. Garn & Best 2010; Reddy et al. 2015) can be used, these do not account for regions that are entirely optically-thick at such wavelengths. Another option is to us the observed slope of the rest-frame UV emission, $\beta_{\rm UV}$, and to calibrate it using the correlation between $\beta_{\rm UV}$ and the infrared excess, IRX $= {\rm L_{IR}}/{\rm L_{UV}}$ (Meurer et al., 1999; Calzetti et al., 2000; Gordon et al., 2003; Reddy et al., 2018). These empirical relations are based on local starburst and star-forming galaxies but hold for high redshift LBGs albeit with higher scatter than locally (Capak et al., 2015; Bouwens et al., 2016; Barisic et al., 2017; Bowler et al., 2018). Measuring IRX for LAEs is more challenging, due to their faintness and infrared wavelengths, though Kusakabe et al. (2015) used their 3σ upper limit on $L_{\rm IR}$ from a Spitzer/MIPS stack of 213 $z \simeq 2.18$ LAEs to determine an upper limit on IRX which is consistent with the SMC attenuation curve (Pettini et al., 1998).

We calculate IRX for our stacks and infrared-detected LAEs using the ${\rm L_{IR}}$ and ${\rm L_{IR}}$ values calculated in Sections 2.4.1 and 2.4.2. We use the $\beta_{\rm UV}$ values from

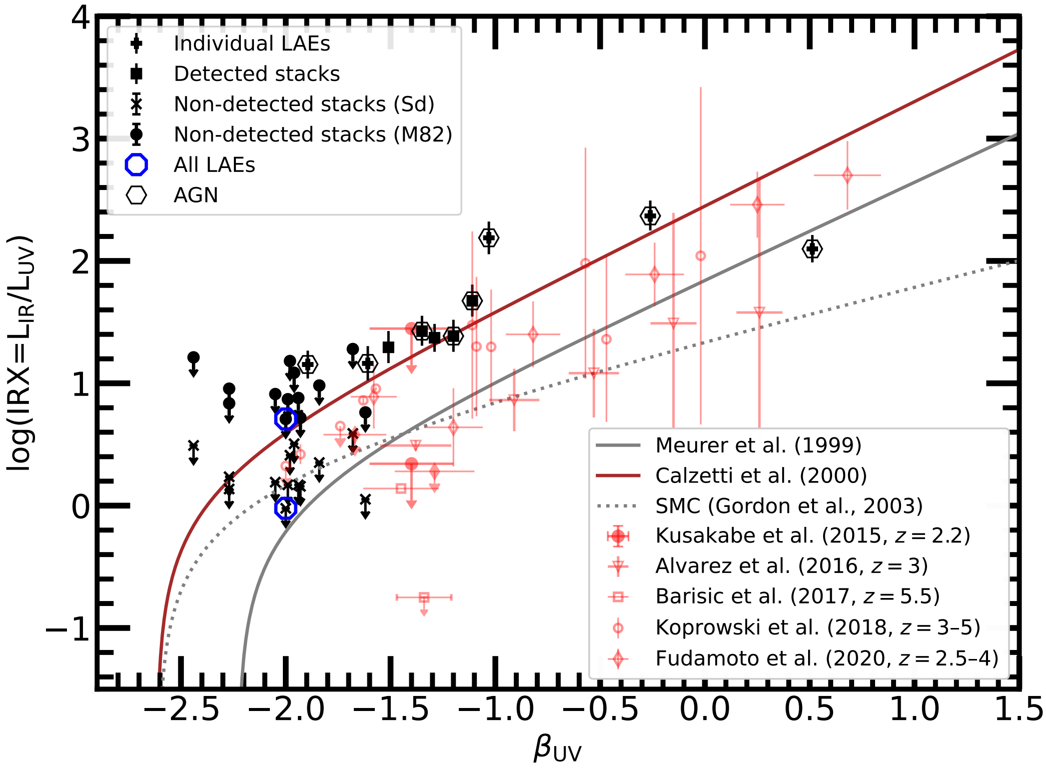

Figure 2.7: The location of our individually-infrared detected LAEs and stacked subsets in the IRX-$\beta_{\rm UV}$ plane, compared with previous LAE (Kusakabe et al., 2015) and LBG (Álvarez-Márquez et al., 2016; Barisic et al., 2017; Koprowski et al., 2018; Fudamoto et al., 2020) studies and empirical relationships from Meurer et al. (1999); Calzetti et al. (2000); Gordon et al. (2003) with adjustments from Reddy et al. (2018). For stacks that are not detected we show upper limits assuming both the Sd and M82 infrared SED templates (which encompass the full range of temperatures in the SWIRE template catalogue Polletta et al. 2007), and we highlight the stack of all LAEs and those containing AGN. Overlapping points have been shifted by 0.1 in the x-direction for visibility. The detected LAEs and stacks typically have higher $\beta_{\rm UV}$ and IRX than the medians of the stacks that are not detected, consistent with the dust laws shown. The detected LAEs and stacks appear to contain dust that is more similar to local star-forming galaxies (Calzetti et al., 2000) than the starburst Meurer et al. (1999) and the SMC (Gordon et al., 2003), which suggests that they are younger and contain more patchy dust than LBGs (Popping et al., 2017).

the SED fits in Santos et al. (2020) and calculate the median β_{UV} for stacked samples. Figure 3.6 compares our IRX-β_{UV} measurements with the empirical relationships from Calzetti et al. (2000) (i.e. local star-forming galaxies), Meurer et al. (1999) (i.e. local starburst galaxies) and Gordon et al. (2003) (i.e. SMC-like dust). We use the updates from Reddy et al. (2018) for the Calzetti et al. (2000) and Gordon et al. (2003) relations, which assumes a $\beta_{\mathrm{UV},0} = -2.62$, metallicity of $0.14Z_{\odot}$, constant star-formation, and a stellar population age of 100 Myr. We also compare with the data for LAEs from Kusakabe et al. (2015) and with LBGs at similar redshifts (Álvarez-Márquez et al., 2016; Barisic et al., 2017; Koprowski et al., 2018; Fudamoto et al., 2020).

Our results are consistent with the upper limits for LAEs from stacked PACS data from Kusakabe et al. (2015), though most of our measurements are significantly higher than the MIPS 24 μm stacked results presented in Kusakabe et al. (2015): this is likely due to the uncertainties associated with extrapolating from 24 μm to the integrated far-infrared luminosity. All except one of our detected stacks (the X-ray AGN) and individually infrared-detected LAEs (SC4K-IA484-28746) lie on or below the Calzetti et al. (2000) extinction curve, suggesting that these systems have similar dust to local star-forming galaxies. The detected LAEs and stacks (i.e. the most massive systems and those containing AGN) have significantly higher IRX (by ~ 0.7 dex) than the LBGs from Álvarez-Márquez et al. (2016) and Barisic et al. (2017) and they are also slightly systematically higher than the LBGs studied by Koprowski et al. (2018) and Fudamoto et al. (2020). This result suggest that the most massive LAEs have younger stellar populations and a higher fraction of stellar light that is not obscured when compared with LBGs (Popping et al., 2017) i.e. these LAEs are young and clumpy or have unevenly distributed dust or a dust screen with holes, which is similar to interpretations of $z \sim 0.3$ LAEs (Oteo et al., 2012).

For the stacks that are not-detected in the infrared we show the 3σ upper limits on IRX from both the Sd and M82 SED templates, which encompass the range of infrared SED temperatures (Polletta et al., 2007). Limits that are calculated assuming the Sd-like SED template are significantly lower than those from the M82 template and would suggest that LAEs are more likely to follow a SMC- or Milky Way-like extinction curve. However, the limits determined from the M82

SED (which gives more typical $f_{\rm esc}$(Lyα) values; Figure 2.6) are also consistent with the Calzetti et al. (2000) relation. Thus, even with a catalogue of ~ 4000 LAEs and stacking some of the deepest *Herschel* and SCUBA-2 data available we are still unable to measure IRX for LAEs with the bluest UV slopes (i.e. $\beta_{\rm UV} \lesssim -1.5$). Deeper measurements are required to determine whether lower-mass LAEs have similar the IRX-$\beta_{\rm UV}$ properties to the higher mass population (which typically have redder UV slopes), though our limits are consistent with this interpretation.

2.5 Conclusions

We have analysed the dust emission and far-infrared properties of 3674 LAEs at $z = 2.2$–6 in the SC4K survey of the COSMOS field (Sobral et al., 2018). We used publicly available *Herschel* PACS and SPIRE data at 100, 160, 250, 350 and 500 μm (Lutz et al., 2011; Oliver et al., 2012; Shirley et al., 2021) and SCUBA-2 850 μm observations from the S2COSMOS survey (Simpson et al., 2019). We identified five LAEs that are sufficiently bright to be detected in the SCUBA-2 850 μm data, and used stacking to probe the submillimetre emission from the remaining LAEs. We performed far-infrared SED fitting, using MCIRSED where possible (i.e. for systems with detections at ≥ 2 infrared wavelengths) and SWIRE galaxy templates otherwise. We used these results to measure IRX-$\beta_{\rm UV}$ and $f_{\rm esc}$(Lyα) for the LAEs that were individually-detected in the submillimetre and for median stacks of subsets of LAEs. Our main results are:

1. The five LAEs that are bright enough to be individually detected in the infrared without stacking all contain radio and/or X-ray AGN and have higher average Lyα luminosity than the SC4K LAEs as a whole. The origin of Lyα, continuum UV, and far-infrared emission from these LAEs is uncertain and may include contributions from the AGN.

2. A stack of all the SC4K LAEs probes down to $\sigma = 0.03$ mJy at 850 μm but this median LAE is still undetected. We also stacked subsets of LAEs in bins of redshift, Lyα luminosity, stellar mass, and distinguished by the

presence of AGN. In these stacks dust emission was detected from the stacks of all AGN, X-ray-selected AGN, radio-selected AGN and the most massive LAEs ($\mathrm{M}_\star = 10^{10-12}\,M_\odot$).

3. Whilst many of the most massive LAEs contain AGN, we also excluded the AGN and stacked the remaining $\mathrm{M}_\star = 10^{10-12}\,M_\odot$ galaxies, showing that these non-AGN but massive LAEs also produce significant dust emission. Thus, the submillimetre emission from LAEs is separately correlated with both stellar mass and AGN activity. Deeper far-infrared data are required to detect dust emission from the lower mass, fainter LAEs.

4. We measured $f_{\mathrm{esc}}(\mathrm{Ly}\alpha)$ for the five LAEs that were individually-detected in the infrared data of 1–7%, and the subsets of LAEs that were detected in the stacks have $f_{\mathrm{esc}}(\mathrm{Ly}\alpha) = 4$–5%. These are similar to previous studies and consistent with the global evolution of $f_{\mathrm{esc}}(\mathrm{Ly}\alpha)$.

5. For undetected stacks, including the stack of entire population of LAEs, we explored the effects of different infrared SED templates and found that the $f_{\mathrm{esc}}(\mathrm{Ly}\alpha)$ that were derived from assuming a Sd-like SED template give $f_{\mathrm{esc}}(\mathrm{Ly}\alpha) \geq 33\%$ (3σ), which is significantly higher than the global $f_{\mathrm{esc}}(\mathrm{Ly}\alpha)$ at comparable redshifts. Limits derived using a M82 SED template are closer to the evolution expected from Hayes et al. (2011), which suggests that LAEs likely have warmer dust than local Sd-like galaxies. The stack of all the SC4K LAEs has a higher limit on $f_{\mathrm{esc}}(\mathrm{Ly}\alpha)$ than expected from the global evolution and may indicate significant variation or evolution within the population.

6. The detected galaxies and median stacks all have redder UV slopes (β_{UV}) than those that were not detected. They also tend to have higher IRX than LBGs, though our results are consistent with the Calzetti et al. (2000) dust law. Our IRX-β_{UV} results suggest that LAEs contain young stellar populations (as expected) and clumpy or unevenly distributed dust.

Deeper far-infrared data, particularly data that are able to probe a variety of individual LAEs, are required to understand the diversity in this population and confirm the effect of stellar mass and AGN on their dust emission. Our study has shown the depths required, which can currently only be obtained with interferometric instruments due to the confusion limit.

Chapter 3

Measuring dust in LAEs using ALMA observations

3.1 Introduction

In this chapter, we expand upon the work in Chapter 2 to focus on the detection and characterization of faint dust emission from LAEs. As we showed in Chapter 2, current single-dish far-infrared telescopes can mostly detect only the brightest LAEs. To gain a complete picture of dust in the LAE population, we need to probe both far-infrared faint and bright LAEs. The ALMA interferometer has emerged as a revolutionary tool in this field, offering the high sensitivity and resolution needed to detect weak dust continuum emission that single-dish instruments often miss. Compared to single-dish observations, ALMA's superior spatial resolution minimizes confusion noise, provides accurate positional matching with optical counterparts, and allows for a deeper investigation into the dust properties of individual LAEs. As a result, faint LAEs that can not be detected with single-dish observations due to limited sensitivity and large beam sizes (e.g. Chapter 2) can be revealed by ALMA.

In this study, we use ALMA archival data from A^{3}COSMOS (Liu et al., 2019; Adscheid et al., 2024) to probe the far-infrared emission from SC4K (Sobral et al., 2018) LAEs at $z = 2$–6. We identify ALMA observations that cover SC4K

LAEs in different continuum bands and fit a modified-blackbody model spectral energy distribution (SED) to calculate far-infrared luminosities and upper limits for detected and undetected LAEs. The $f_{\rm esc}({\rm Ly}\alpha)$ and IRX values for all observed LAEs are estimated by combining these new deep far-infrared measurements with exiting short wavelength properties from the SC4K survey. Our far-infrared measurements are valuable for further constraining the IRX-$\beta_{\rm UV}$ and main sequence relation for LAEs, comparing $f_{\rm esc}({\rm Ly}\alpha)$ values with the global $f_{\rm esc}({\rm Ly}\alpha)$ evolution.

The structure of this chapter is as follows: in Section 3.2, we present our sample of LAEs from SC4K and far-infrared data from the ALMA archive. Identified ALMA observations and detections, SED fitting, $f_{\rm esc}({\rm Ly}\alpha)$ and IRX-$\beta_{\rm UV}$ for observed LAEs are described in Section 3.3. We present the conclusions in Section 3.4. For this study, we follow a cold dark matter cosmology (ΛCDM) with $H_0 = 69.3$ kms^{-1} Mpc^{-1}, $\Omega_{\rm M} = 0.29$, and $\Omega_\Lambda = 0.71$ (Hinshaw et al., 2013) and employ the Chabrier (Chabrier, 2003) initial mass function (IMF).

3.2 Data

In this study, we analyze the properties of dust emission from LAEs in the ~2 deg^2 COSMOS field using far-infrared data from the extensive ALMA archive [1].

3.2.1 LAE sample

As in Chapter 2, we use a sample of 3908 LAEs including 314 AGN (8%; Calhau et al., 2020) from the SC4K survey (Sobral et al., 2018) obtained using the ground based Subaru and the Isaac Newton telescopes. These LAEs are selected by targeting the Lyα line, using deep narrow- and medium-band observations. This survey is spread across 16 redshift slices and includes 3683 LAEs with reliable parameters derived from spectral energy distribution (SED) fitting (Santos et al., 2020). The sample covers Lyα luminosity ($\log_{10}(L_{{\rm Ly}\alpha}/{\rm erg\ s^{-1}})$) from 42.06 to 44.54.

---

[1] `https://almascience.eso.org/aq/`

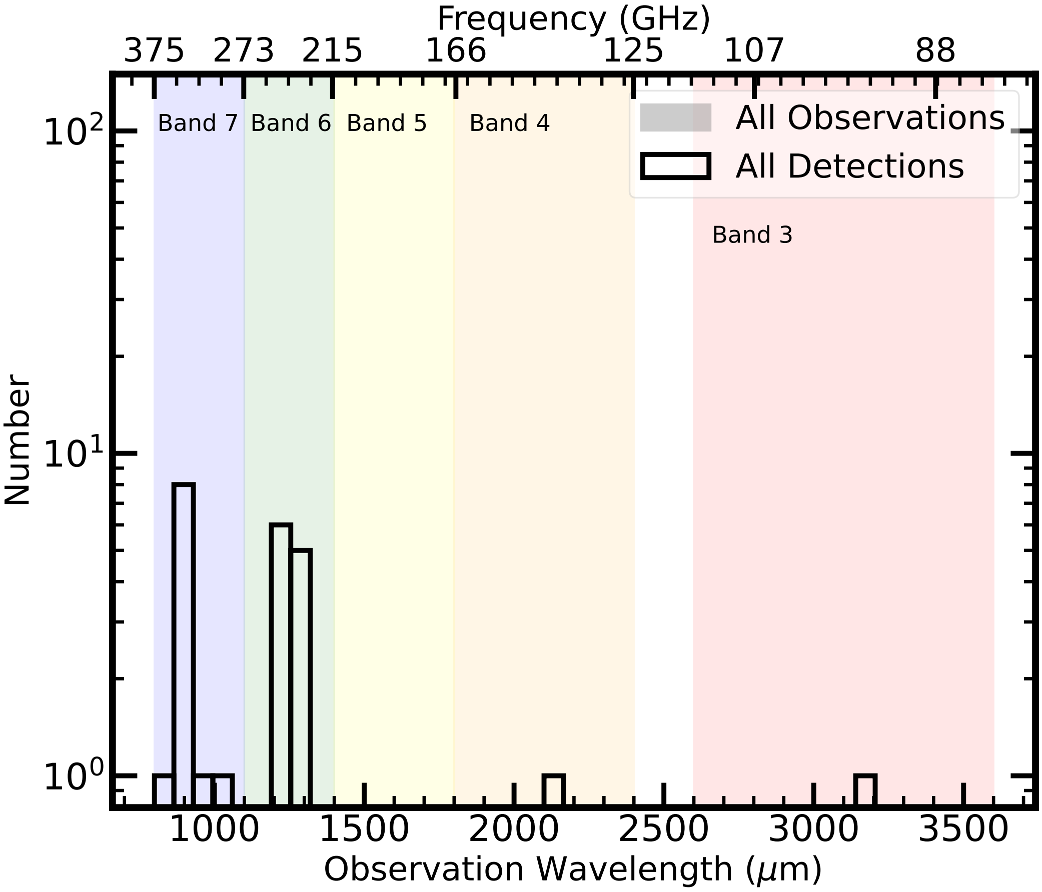

Figure 3.1: The wavelength distribution of ALMA archival observations of SC4K LAEs. The shaded gray and unfilled black distributions represent the number of A^{3}COSMOS unique observations and detections spread across Bands 3 through 7. The spatial coverage for Band 5 is significantly lower than the other Bands, resulting in no LAE observations in this Band. Whilst many LAEs are observed in Bands 3 and 4 most of the continuum detections are in Bands 6 and 7 due to the sensitivity of these data to the peak of the dust SED. The blue, green yellow, orange and red stripes shows the wavelength coverage for Bands 7, 6, 5, 4 and 3 respectively.

3.2.2 Far-infrared data

We utilize far-infrared ALMA data from Automated Mining of the ALMA Archive in the COSMOS Field (A^3COSMOS; Liu et al., 2019; Adscheid et al., 2024, version number `20220606`). The A^3COSMOS project uses publicly available ALMA archive data from Bands 3, 4, 6 and 7, each with a spatial coverage of approximately 200 arcmin^2, up until June 6, 2022. This database uses the COSMOS master catalogue (Liu et al., 2019), prepared using COSMOS2015 (Laigle et al., 2016), K_s-band (Muzzin et al., 2013), i-band (Capak et al., 2007), IRAC (Sanders et al., 2007), and VLA (Smolčić et al., 2017) prior catalogues, to locate and measure flux densities of these previously detected sources. As a result, it includes 1,756 unique sources, including both detections and the positions of sources in the prior catalogue and 131 sources identified through blind photometry only. The spatial coverage of this database is significantly lower than single-dish observations such as S2COSMOS (Simpson et al., 2019) due to the small ALMA field of view. However, single dish observations suffer from source confusion, resulting in lower sensitivity than deep interferometric surveys. The depth (1σ pixel RMS noise) of A^3COSMOS data for ALMA Bands 3, 4, 6 and 7 ranges form 0.01 to 1 mJy, which makes the deepest ALMA observations $\sim$100 times deeper compared to the single-dish survey, S2COSMOS.

To analyse the dust properties of LAEs, we first match the SC4K coordinates with the A^3COSMOS catalogue within a matching radius of 10 arcseconds using both best and all matches within the target radius. The distribution of angular separations from both methods shows a minimum at 1.5 arcseconds, leading us to choose a 1.5 arcsecond radius as the cut-off for identifying physically-associated sources. Similar steps are applied to the blind catalogue with the same 1.5 arcsecond matching radius. Following Liu et al. (2019), we consider sources with a 4.35σ peak in the prior catalogue as detections. At this signal-to-noise ratio (SNR), the probability of a source being a spurious detection is 50%. In the blind catalogue the threshold for 50% of sources being spurious is higher at 5.4σ. In case of detection in both the prior and blind catalogues we preferentially select the match in the prior catalogue due to the probability of spurious detection for

Table 3.1: The number of SC4K LAEs that have been observed by ALMA in at least one Band. Repeat observations may be in the same or different Bands.

	# Observations	# Observed LAEs	# Detected LAEs
	1	254	8
	2	66	3
	3	30	4
	4	12	0
	5	6	1
	6	2	0
	7	2	0
	8	1	0
	19	1	0
	20	1	0
Total	627	375	16

the same SNR level. After cross-matching, we find that all blind LAE detections are already in the prior catalogue and therefore we use the prior catalogue only. We manually check matching separation and A^{3}COSMOS ID to ensure the ALMA observations are associated with LAEs.

Table 3.2: Far-infrared properties of 16 SC4K LAEs detected in A^{3}COSMOS. We utilize ALMA detections and flux upper limits from A^{3}COSMOS and fit a modified blackbody curve to determine their far-infrared luminosity and star-formation rate (Section 3.3.2; table continous on next page).

Source ID	$z_{\rm phot}$	AGN Status	Wavelength (μm)	Flux Density^b (mJy)	$\log_{10}(L_{\rm IR})^c$ ($L_\odot$)	SFR$^c_{\rm IR}$ ($M_\odot\,{\rm yr}^{-1}$)
SC4K-NB392-201	2.22	X-ray	1287	0.21±0.05	11.55±0.09	39±9
SC4K-IA427-47810[a]	2.50	Blazar	873, 873	0.20±0.05, ≤ 0.11	–	–
			3200	0.22±0.02		
SC4K-IA427-26216	2.50	Radio	1287	0.25±0.07	11.62±0.10	45±12
SC4K-IA484-176970	2.99	–	873, 1249	0.77±0.28, ≤ 0.84	11.62±0.13	45±16
SC4K-IA484-28746[d]	2.99	X-ray and Radio	873, 1287	4.36±0.29, 1.23±0.18	12.29±0.05	214±28
			2124	0.23±0.05		
SC4K-IA484-33705	2.99	Radio	1249, 1287	0.34±0.12, 0.43±0.16	11.74±0.14	60±22
SC4K-IA484-62915	2.99	X-ray and Radio	873	0.72±0.28	11.59±0.14	42±16
SC4K-IA505-158978	3.16	X-ray and Radio	873, 1287	2.91±0.42, 0.63±0.07	12.09±0.05	135±18
SC4K-IA505-178627[d]	3.16	X-ray and Radio	873, 873	5.26±0.47, 5.27±0.68	12.45±0.05	310±34
			2035, 2156	≤ 0.37 , ≤ 0.39		
SC4K-IA505-93122	3.16	X-ray	1249	0.38±0.09	11.70±0.09	55±13

(Continued)

Source ID	$z_{\rm phot}$	AGN	Wavelength (μm)	Flux Density[b] (mJy)	$\log_{10}(L_{\rm IR})^c$ ($L_\odot$)	$\mathrm{SFR}^c_{\rm IR}$ ($M_\odot\,\mathrm{yr}^{-1}$)
SC4K-IA527-200272	3.33	X-ray and Radio	1249	1.09±0.11	12.15±0.04	153±15
SC4K-IA574-34828[d]	3.74	X-ray and Radio	1249, 1249	3.44±0.12, 3.50±0.13	12.62±0.02	456±17
			1249	3.37±0.14		
SC4K-IA679-203642	4.58	–	860	0.20±0.07	11.06±0.14	12±5
SC4K-IA679-223923[d]	4.58	Radio	869	5.32±0.13	12.50±0.01	342±8
SC4K-IA767-174198	5.32	X-ray	953	0.27±0.06	11.28±0.09	21±5
SC4K-NB816-459515	5.70	–	1029, 2067	0.45±0.04, $\leq$ 0.06	11.56±0.04	39±4

[a] This source is likely a flat spectrum radio source (e.g. blazar Smolčić et al., 2017), thus we exclude it from further analysis.

[b] In case of non-detections flux density upper limits are at 4.35σ.

[c] The far-infrared luminosity and IR SFRs are derived using a modified-blackbody SED with $T_{\rm dust} = 40\,$K and $\beta_{\rm IR} = 1.96$. These inferred parameters have typical systematic uncertainties of ±0.4 dex and $\pm 60\,M_\odot\,\mathrm{yr}^{-1}$, respectively, which is due to the choice of SED (Section 3.3.2).

[d] The source is also detected in at least two bands from single-dish observations (Chapter 2). The difference in $L_{\rm IR}$ is likely due to the different SED fitting method used in Chapter 2.

3.3 Results and discussion

3.3.1 ALMA observations and detections

The process of catalogue matching and identifying LAE counterparts in ALMA observations results in 627 unique observations of 375 LAEs, including 119 observations of 69 LAEs with AGN. The number of ALMA observations and detections per LAE is shown in Table 3.1. The sensitivity within the ALMA field of view decreases as we move from the center to the outskirts due to the primary beam. Amongst the 627 observations, only 364 (58%) fall in the $> 50\%$ sensitivity range of the ALMA primary beam.

Dust continuum emission is detected at SNR $> 4.35\sigma$ from 16 LAEs across 24 observations (Table 3.2). Amongst these 16 A^{3}COSMOS-detected LAEs 13 are AGN hosts (Calhau et al., 2020). All of these detections are in the $> 50\%$ sensitivity region, and the LAE furthest from the pointing centre achieves 67% of the peak coverage. One of LAEs (SC4K-IA427-47810) has detections at both 870 and 3200 μm with similar flux densities at both wavelengths. This is unusual, as star-forming galaxies typically do not have flat far-infrared spectral energy distributions (SED). Radio data show that SC4K-IA427-47810 is a Compton-thick AGN containing extremely bright radio source (Smolčić et al., 2017). We therefore exclude this source from further analysis. Among the 15 remaining sources, four are also detected with *Herschel*/SCUBA-2 (Chapter 2).

In Bands 7, 6, 4 and 3, we identify 146, 143, 146 and 191 A^{3}COSMOS LAE observations respectively. However, only 11, 11, 1, and 1 detections in Bands 7, 6, 4 and 3, respectively, are confirmed to be associated with LAEs. The number of ALMA observations and detected LAEs per Band is illustrated in Figure 3.1. The A^{3}COSMOS spatial coverage in Bands 5, 8, and 9 is limited as these Bands are significantly affected by the atmospheric absorption lines. We identify dust emission associated with 15 unique LAEs, most of which are in Bands 6 and 7. The dust emission peak ($\lambda_{\rm rest} \sim 100\mu$m) is expected to fall at $\lambda_{\rm obs} \sim 300$–$700\ \mu$m for the SC4K LAEs. Many LAEs are observed in Bands 3 and 4, but continuum detections are predominantly seen in Bands 6 and 7, as these Bands are more sensitive to the peak of the dust SED.

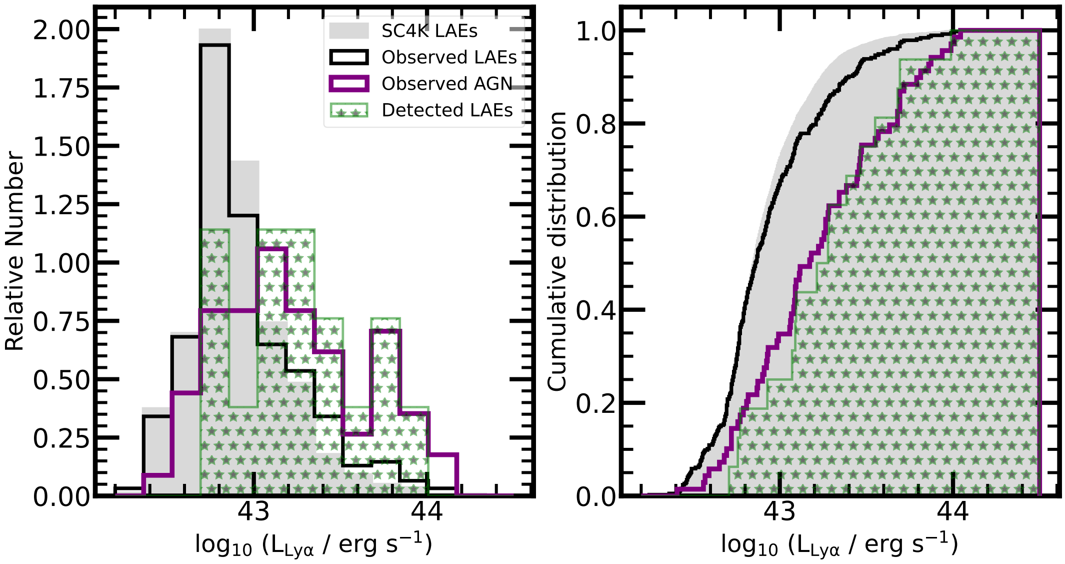

Figure 3.2: Comparison of the Lyα luminosity distribution differential (left) and cumulative (right) of all SC4K LAEs with ALMA-observed LAEs, ALMA-observed LAEs containing AGN and detected LAEs. The SC4K and ALMA-observed LAEs show very similar distribution, suggesting that archival observations of SC4K LAEs are randomly distributed, as expected since the LAEs are mostly untargeted but are serendipitously observed in the fore/background of other observations. Observed AGN and all ALMA-detected LAEs are brighter in Lyα than the parent distribution, suggesting bias in these selections. Calhau et al. (2020) showed that LAEs with the highest Lyα luminosity are more likely to be AGN, which is consistent with these data. The comparison of all SC4K LAEs with ALMA-detected LAEs shows that the most Lyα luminous systems are also more likely to have detected dust emission, suggesting that they are brightest in the far-infrared.

A comparison of the distribution of Lyα luminosity for the whole SC4K sample, ALMA-observed LAEs, ALMA-observed LAEs containing AGN and detected LAEs is shown in Figure 3.2. The SC4K and ALMA-observed LAEs show broadly similar distributions, consistent with the expectation that archival observations sample a wide range of LAEs in a relatively unbiased manner. This is expected, given that most SC4K LAEs were not directly targeted but serendipitously observed in the foreground or background of observations. However, there is a clear bias in the A^{3}COSMOS detections toward Lyα-bright sources, many of which host AGN. This trend aligns with the findings of Calhau et al. (2020), who showed that the most Lyα-luminous LAEs are more likely to host AGN and have dust emission detectable in the far-infrared. So, while the overall LAE population appears well represented, the detected group is mostly AGN-dominated and IR-bright systems.

In Figure 3.3, we compare the Lyα luminosity and observation wavelengths of all A^{3}COSMOS counterpart observations of SC4K LAEs including AGN observations and detections along with their RMS noise. We include 627 A^{3}COSMOS observations at different wavelengths for 375 LAEs, including 119 AGN, resulting in 16 detections. The A^{3}COSMOS archival data reveals more detections at shorter wavelengths (Bands 6 and 7) compared to longer wavelengths (Bands 3 and 4) as shown in Figure 3.1, despite the lower RMS noise at longer wavelengths. This discrepancy arises because the peak of dust emission at the target redshift range ($z = 2$–6) is expected to be between 300-700 μm making it closer to Bands 6 and 7. Consequently, these galaxies are expected to be brighter in Bands 6 and 7 and fainter in Bands 3 and 4. The dust SED shape is likely also the reason that most Bands 3 and 4 data are deeper than the Bands 6 and 7 observations.

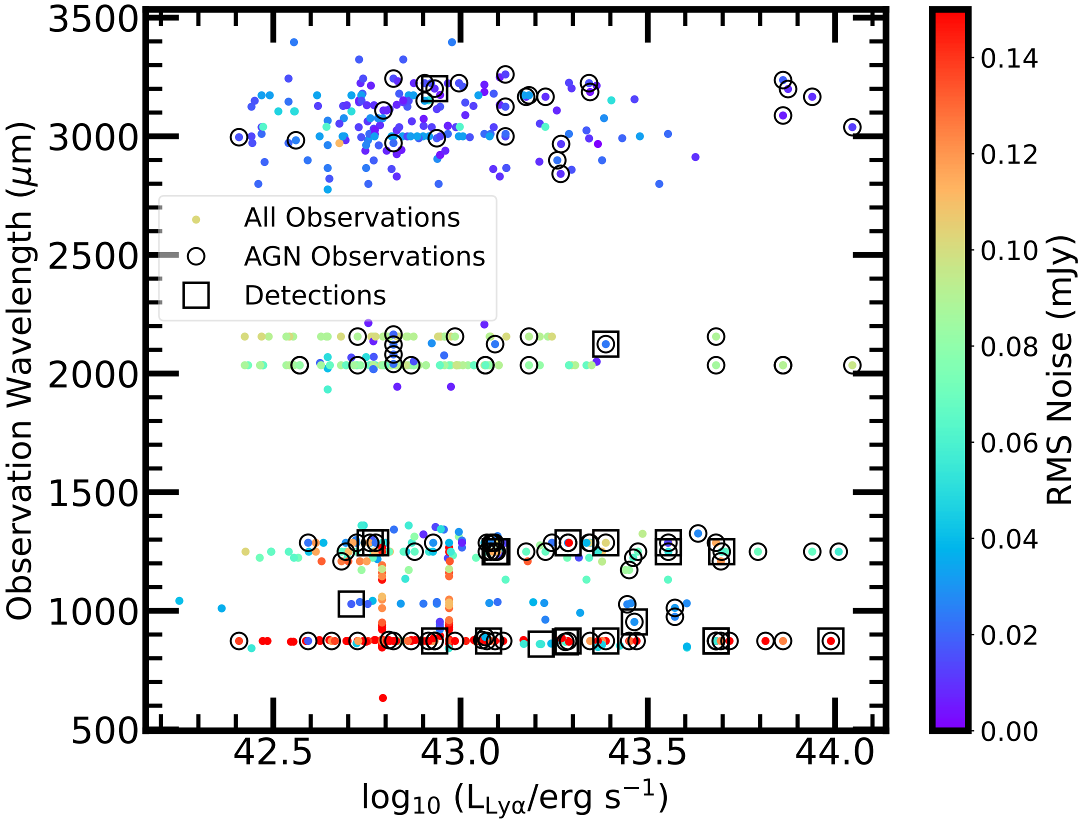

Figure 3.3: Distribution of Lyα luminosity and observation wavelengths of A^{3}COSMOS observations of SC4K LAEs, with LAEs that contain AGN and those that are detected in ALMA highlighted. The RMS noise of each observation is indicated by the colourbar. Most detections are at observation wavelengths of 800–1300 μm which correspond to the peak of the dust SED. Thus, despite being shallow (i.e., having high RMS) at these wavelengths, more sources are detected there.

Table 3.3: Physical properties of ALMA-detected LAEs. (continued on next page)

Source ID	$z_{\rm phot}$	UV slope ($\beta_{\rm UV}$)	$\log_{10}$($\rm L_{Ly\alpha}$) ($\rm erg\,s^{-1}$)	$\rm SFR_{Ly\alpha}$ ($M_\odot\,\rm yr^{-1}$)	$\log_{10}$($\rm L_{UV}$)^d ($L_\odot$)	$\rm SFR_{UV}$ ($M_\odot\,\rm yr^{-1}$)	$f_{\rm esc}$(Lyα)	$\log_{10}$(IRX)
SC4K-NB392-201	2.22	-1.04	$42.77^{+0.04}_{-0.04}$	$3.4^{+0.3}_{-0.3}$	11.22	24.8±2.9	$0.05^{+0.01}_{-0.01}$	$0.34^{+0.14}_{-0.13}$
SC4K-IA427-26216	2.50	-1.26	$42.76^{+0.05}_{-0.05}$	$3.3^{+0.4}_{-0.4}$	10.47	4.5±0.5	$0.07^{+0.02}_{-0.02}$	$1.15^{+0.15}_{-0.13}$
SC4K-IA484-176970	2.99	-1.03	$43.08^{+0.03}_{-0.04}$	$6.8^{+0.6}_{-0.6}$	10.39	3.7±0.4	$0.14^{+0.05}_{-0.05}$	$1.23^{+0.18}_{-0.15}$
SC4K-IA484-28746^e	2.99	0.51	$43.39^{+0.02}_{-0.02}$	$14.0^{+0.5}_{-0.6}$	10.85	10.7±1.2	$0.06^{+0.01}_{-0.01}$	$1.44^{+0.11}_{-0.11}$
SC4K-IA484-33705	2.99	-1.89	$43.56^{+0.01}_{-0.01}$	$20.6^{+0.6}_{-0.6}$	10.66	6.9±0.8	$0.31^{+0.10}_{-0.10}$	$1.08^{+0.19}_{-0.16}$
SC4K-IA484-62915	2.99	-2.00	$43.99^{+0.01}_{-0.01}$	$55.9^{+0.6}_{-0.6}$	11.61	61.4±7.1	$0.54^{+0.09}_{-0.09}$	$-0.02^{+0.19}_{-0.16}$
SC4K-IA505-158978	3.16	-1.27	$43.29^{+0.03}_{-0.03}$	$11.1^{+0.8}_{-0.7}$	10.67	7.1±0.8	$0.08^{+0.01}_{-0.01}$	$1.42^{+0.11}_{-0.11}$
SC4K-IA505-178627^e	3.16	-1.89	$43.68^{+0.01}_{-0.01}$	$27.6^{+0.7}_{-0.7}$	11.37	35.1±4.1	$0.08^{+0.01}_{-0.01}$	$1.08^{+0.11}_{-0.11}$
SC4K-IA505-93122	3.16	-0.74	$43.10^{+0.04}_{-0.05}$	$7.2^{+0.8}_{-0.7}$	10.45	4.2±0.5	$0.12^{+0.03}_{-0.03}$	$1.25^{+0.14}_{-0.13}$
SC4K-IA527-200272	3.33	-2.14	$43.70^{+0.01}_{-0.01}$	$28.6^{+0.6}_{-0.5}$	11.61	61.7±7.1	$0.13^{+0.01}_{-0.01}$	$0.54^{+0.11}_{-0.11}$

(Continued)

Source ID	$z_{\rm phot}$	UV slope ($\beta_{\rm UV}$)	$\log_{10}(\rm L_{Ly\alpha})$ (erg s^{-1})	SFR$_{\rm Ly\alpha}$ ($M_\odot$ yr^{-1})	$\log_{10}(\rm L_{UV})^d$ ($L_\odot$)	SFR$_{\rm UV}$ ($M_\odot$ yr^{-1})	$f_{\rm esc}$(Lyα)	$\log_{10}$(IRX)
SC4K-IA574-34828^e	3.74	-1.03	$43.09^{+0.06}_{-0.06}$	$7.1^{+1.0}_{-0.9}$	10.81	9.8±1.2	$0.02^{+0.01}_{-0.01}$	$1.81^{+0.10}_{-0.10}$
SC4K-IA679-203642	4.58	-1.84	$43.22^{+0.06}_{-0.07}$	$9.4^{+1.4}_{-1.4}$	11.29	29.5±3.4	$0.22^{+0.05}_{-0.05}$	$-0.23^{+0.19}_{-0.16}$
SC4K-IA679-223923^e	4.58	-0.26	$43.28^{+0.05}_{-0.06}$	$10.9^{+1.4}_{-1.5}$	10.69	7.4±0.9	$0.03^{+0.01}_{-0.01}$	$1.81^{+0.10}_{-0.10}$
SC4K-IA767-174198	5.32	-2.44	$43.46^{+0.05}_{-0.06}$	$16.7^{+2.2}_{-2.1}$	11.33	32.5±3.7	$0.31^{+0.06}_{-0.05}$	$-0.05^{+0.14}_{-0.13}$
SC4K-NB816-459515	5.70	-1.41	$42.71^{+0.06}_{-0.08}$	$2.9^{+0.4}_{-0.5}$	11.09	18.5±2.1	$0.05^{+0.01}_{-0.01}$	$0.47^{+0.11}_{-0.11}$

[d] The typical uncertainty in $\log_{10}(L_{\rm UV})$ is 0.6 dex estimated assuming 0.1 uncertainty in $M_{\rm UV}$.

[e] The source is also detected with shallower single-dish observations (Chapter 2). The difference in $f_{\rm esc}$(Lyα) (up to ∼5%) is likely due to the different SED fitting method used in Chapter 2.

3.3.2 SED Fitting

To analyse the far-infrared properties of 375 A^{3}COSMOS-observed LAEs including 15 detected LAEs, we fit modified-blackbody to the ALMA continuum flux densities from Liu et al. (2019). In case of non-detections, we show flux density upper limits (4.35σ; Liu et al., 2019). These limits are not used in SED fitting; they are used only to indicate non-detections. We utilize the adjusted modified blackbody equation from Casey (2012) which consists of two components, namely a power-law component at the short wavelength side and a cold-dust single-temperature greybody. The hot-dust power-law component dominates below 50 μm (mid-IR) and it is governed by a mid-IR power-law slope (α). The cold-dust components dominates at longer wavelengths and is governed by the dust emissivity ($\beta_{\rm IR}$). The modified blackbody function assumes that the optical depth becomes unity at $\lambda_0 = 200$ μm (Conley et al., 2011). Moreover, we apply a fixed value of α=2, which is expected to be consistent with the most sources (Casey, 2012) and $\beta_{\rm dust}$=1.96 from Ward et al. (2024) estimated for bright infrared galaxies at $z = 2$–6. We also employ SED fitting to the templates of M82 (starburst) and Sd (star-forming) galaxies from the SWIRE template library (Polletta et al., 2007) covering the range of possible SED fits for our targets (see also Chapter 2). We scale the modified blackbody, M82 and Sd templates at detected photometric point and for sources detected in more than one observation, we use the average flux densities and wavelength to calculate the scaling position of the SED fits. These SED fits are shown in Figure 3.4.

To determine far-infrared luminosity of detected LAEs, we utilize the area under the modified blackbody curve integrated from rest-frame 8 to 1000 μm (e.g. Kennicutt, 1998b). Infrared star-formation rates, SFR$_{\rm IR}$ are derived from these using the relation from Kennicutt (1998b) with a correction of a factor of 0.63 for Chabrier IMF (similarly to Chapter 2). The derived $L_{\rm IR}$ ($10^{11.1}$–$10^{12.6}$ $L_\odot$) and SFR$_{\rm IR}$ ($12 - 456$ $M_\odot$ yr^{-1}) for detected LAEs are presented in Table 3.2 with statistical errors from the photometric uncertainties. The modified blackbody fit is our primary method. The Sd and M82 templates are included to account for a broader range of possible SED shapes, given the limited photometric coverage. Our data consist of at most three measurements, primarily on the Rayleigh-Jeans side of the SED, and sometimes include upper limits. Consequently, the derived far-infrared luminosities and IR SFRs have typical systematic uncertainties of $\pm 0.4\,\mathrm{dex}$ and $\pm 60\,M_\odot\,\mathrm{yr}^{-1}$ respectively, driven by the choice of SED model. To approximate upper limits on far-infrared luminosities and $\mathrm{SFR}_{\mathrm{IR}}$ we use the same SED-fitting method for LAEs that were observed by ALMA but not detected. These will be used to evaluate lower limits on the Lyα escape fraction and upper limits on the infrared excess (Section 3.3.3 and 3.3.4).

3.3.2.1 Dust Temperature

This section discusses the dust temperature (T_{dust}) corresponding to the peak of the SED fits (Figure 3.4). The modified blackbody SED fit (Casey, 2012) used in this study is a function of intrinsic T_{dust} and includes two components: a warmer component dominating the shorter-wavelength side and a colder component contributing to the longer-wavelength side. In galaxies with AGN, the warmer and more compact dust components, often heated by AGN activity, contributes to the mid-infrared emission, while the cold-dust emission peaks at relatively longer wavelength. As among 16 A^{3}COSMOS-detected LAEs (see Table 3.2) all except three are AGN hosts, thus dust heating by AGN along with the cold-dust emission may be present for some of our targets. Therefore, to determine the range of dust temperatures represented by the M82 and Sd templates, we employ a modified blackbody function scaled to the median redshift of the A^{3}COSMOS-detected LAEs ($z = 3.16$). The dust temperature limits are defined by the temperatures at which the peaks of the Sd and M82 templates intersect the peak of the modified blackbody curve. Based on this method, we estimate the lower and upper limits of the dust temperature to be approximately 25 K and 55 K, respectively. For all SED fittings, we primarily use a modified blackbody function with a fixed dust temperature of $T_{\mathrm{dust}} = 40\,\mathrm{K}$, representing the average of these two bounds.

3.3.3 Lyα Escape Fraction

Lyα photons are good tracers of distant SFR. However, as described in Section 1.5 Lyα is strongly affected by resonant scattering and dust and is therefore challeng-

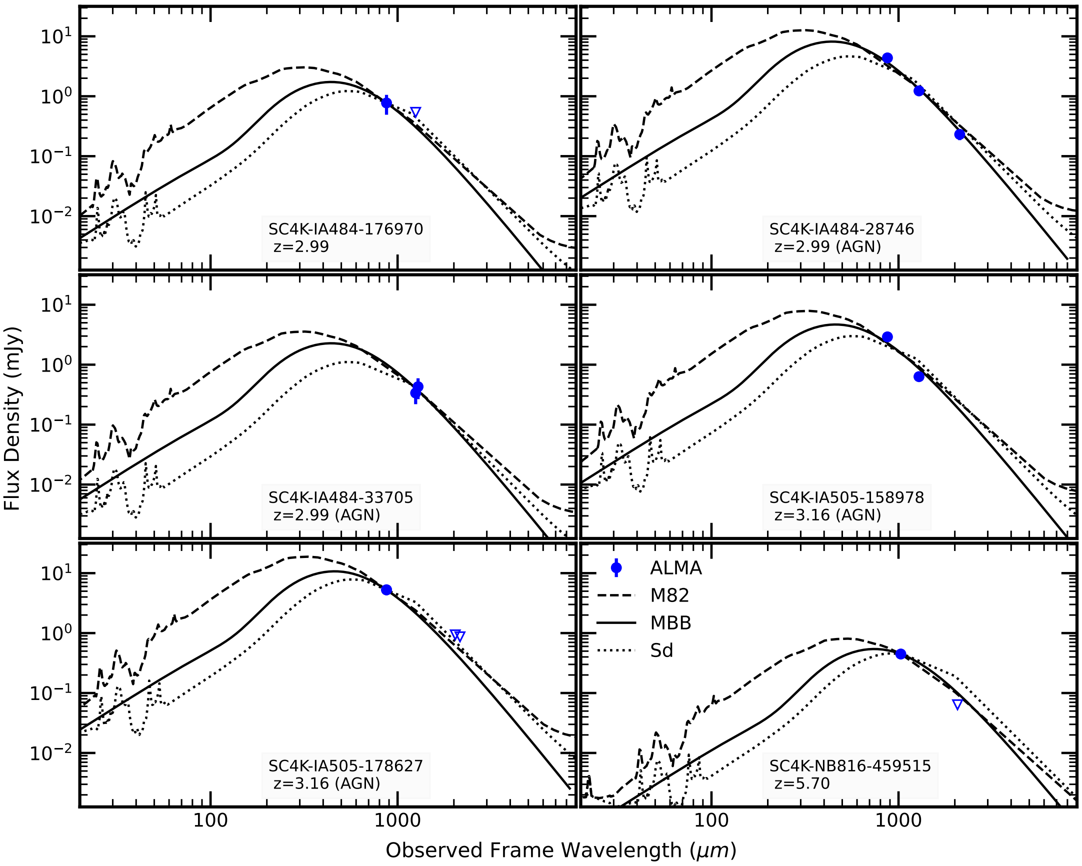

Figure 3.4: Example far-infrared SEDs of ALMA-detected LAEs with more than one ALMA observations. SEDs from Polletta et al. (2007) and a modified blackbody with α=2, $\beta_{\rm dust}$=1.96 and $T_{\rm dust}=40$K are scaled to the ALMA photometry. The Sd and M82 templates cover a range of dust temperature from $T_{\rm dust}\approx 25$ to 55K. The ALMA detections and upper limits (4.35σ) are depicted by blue dots and inverted blue triangles respectively. We determine the far-infrared luminosities by integrating the area under the curve from rest-frame 8 to 1000 μm and estimate their typical systematic uncertainties by employing $L_{\rm IR}$ range from the Sd and M82 templates. An SED that approaches 4.35σ upper limits is nearly inconsistent with the data, so caution is needed when using SED-driven $L_{\rm IR}$.

ing to interpret. We use the deep ALMA measurements of obscured emission from LAEs to calculate the $f_{\rm esc}({\rm Ly}\alpha)$ using equation 3.1. To calculate total SFR for each LAE, we need to combine dust-uncorrected $\rm SFR_{UV}$ and obscured ($\rm SFR_{IR}$).

$$f_{\rm esc}({\rm Ly}\alpha) = \frac{\rm SFR_{Ly\alpha}}{\rm SFR_{UV} + SFR_{IR}} \tag{3.1}$$

We estimate the dust-uncorrected $\rm SFR_{UV}$ and $\rm SFR_{Ly\alpha}$ (Table 3.3) using $\rm M_{UV}$ and Lyα luminosity, respectively, from SC4K by applying Kennicutt (1998b) with a correction of a factor of 0.63 for Chabrier IMF. The $\rm SFR_{IR}$ for this analysis is shown in Table 3.2 and calculated as described in Section 3.3.2. We derive $f_{\rm esc}({\rm Ly}\alpha)$ of the 15 $\rm A^3$COSMOS-detected LAEs are between 2–54% and presented in Table 3.3. We compare our results with the global $f_{\rm esc}({\rm Ly}\alpha)$ at similar redshift in Figure 3.5. The $f_{\rm esc}({\rm Ly}\alpha)$ of $\rm A^3$COSMOS-detected LAEs and the lower limits on $f_{\rm esc}({\rm Ly}\alpha)$ of $\rm A^3$COSMOS-observed LAEs scatter around the global $f_{\rm esc}({\rm Ly}\alpha)$ from Hayes et al. (2011) and Konno et al. (2016). Our results are consistent with Wardlow et al. (2014) and Chapter 2 who followed the same methodology. However, the constraint on $f_{\rm esc}({\rm Ly}\alpha)$ from Kusakabe et al. (2015) at $z = 2.2$, who also used the same method, is ∼3–4 times higher than our findings. It is important to note that our detections are affected by systematic uncertainties due to the choice of SED (Section 3.3.2), which can contribute uncertainties of up to 38%. Although our results are in general agreement with other studies (e.g., Erb et al., 2019; Matthee et al., 2021; Huang et al., 2021; Melinder et al., 2023; Ning et al., 2023; Roy et al., 2023), some of the SC4K LAEs have significantly higher or lower $f_{\rm esc}({\rm Ly}\alpha)$ than the global trend. Many of these are galaxies that have X-ray or radio AGN (Calhau et al., 2020), which may impact $f_{\rm esc}({\rm Ly}\alpha)$. The large variation in $f_{\rm esc}({\rm Ly}\alpha)$ between different LAEs is consistent with our results from Chapter 2 and supports the hypothesis of many LAEs containing unevenly distributed dust.

3.3.4 The IRX-$\beta_{\rm UV}$ Relation

UV-optical observations are significantly affected by the absorption and scattering of these photons by dust particles in the ISM, which can substantially alter the

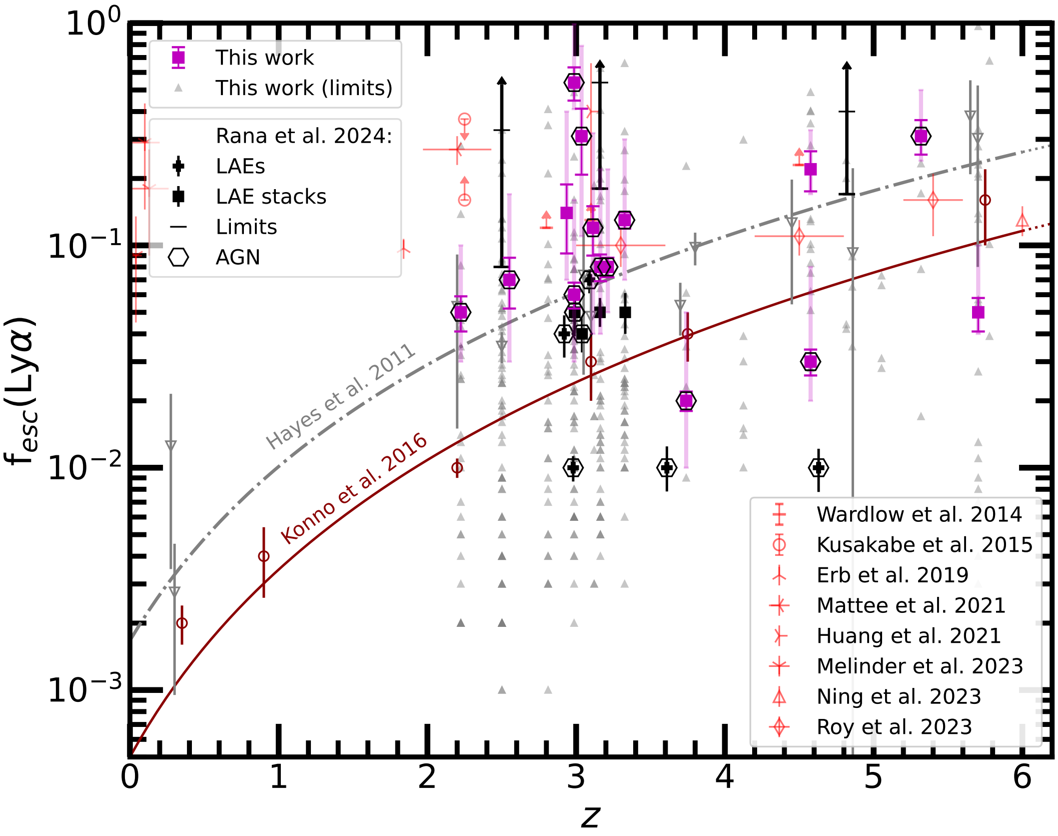

Figure 3.5: The escape fraction of Lyα photons from LAEs as function of redshift. Lines represent global redshift evolution of $f_{\rm esc}({\rm Ly}\alpha)$ for LAEs from (Hayes et al., 2011; Konno et al., 2016). We present the $f_{\rm esc}({\rm Ly}\alpha)$ values and lower limits on $f_{\rm esc}({\rm Ly}\alpha)$ for A^{3}COSMOS-detected and observed LAEs indicated by filled magenta squares and grey triangles, respectively. Darker errorbars show the statistical errors and the faded error bars represent the systematic uncertainties due to the choice of SED (Section 3.3.2). Black filled symbols depict $f_{\rm esc}({\rm Ly}\alpha)$ of individual LAEs, stacks of LAEs and lower limits on $f_{\rm esc}({\rm Ly}\alpha)$, respectively, from Chapter 2. Sources containing AGN in this study and from Chapter 2 are highlighted. Red symbols show the $f_{\rm esc}({\rm Ly}\alpha)$ for LAEs at similar redshifts from other studies (Wardlow et al., 2014; Kusakabe et al., 2015; Erb et al., 2019; Matthee et al., 2021; Huang et al., 2021; Melinder et al., 2023; Ning et al., 2023; Roy et al., 2023)

observed properties of galaxies. The photometric impact of dust is characterised by empirical dust extinction laws such as Meurer et al. (1999); Calzetti et al. (2000) and Gordon et al. (2003) which parametrize the relationship between the infrared excess (IRX = $L_{\rm IR}$ / $L_{\rm UV}$) and $\beta_{\rm UV}$. The Meurer et al. (1999) law represents UV-bright starburst galaxies dominated by young massive stars with lower metallicities than those associated with the Calzetti et al. (2000) law, whereas the SMC curve reflects stellar populations dominated by both young and older stars with significantly lower metallicities. These laws are sensitive to different conditions in star-forming regions that predominantly vary in terms of stellar age and metallicity.

IRX values for our ALMA detections and non-detections are calculated using the SED-driven $L_{\rm IR}$ (Section 3.3.2) and $\rm M_{UV}$ (Santos et al., 2020). We utilize $\beta_{\rm UV}$ values from the SC4K survey. The IRX and $\beta_{\rm UV}$ values for the 15 ALMA-detected LAEs are presented in Table 3.3 and in Figure 3.6. We compare our IRX-$\beta_{\rm UV}$ values with existing dust extinction curves for local starburst, star-forming galaxies and the SMC (Meurer et al., 1999; Calzetti et al., 2000; Gordon et al., 2003). We also compare our findings with previous studies on LAEs by Kusakabe et al. (2015) and Chapter 2, as well as LBGs at redshifts $z \sim$ 2–6.

Our results are consistent with the upper limits reported by Kusakabe et al. (2015) for LAEs at $z = 2.2$. However, individual detections, stacks and stack upper limits on LAEs from Chapter 2 follow the Calzetti et al. (2000) curve, which represents local star forming galaxies with young and intermediate-age stellar populations and near-solar metallicities. As we now utilize the superior sensitivity of ALMA compared to single-dish observations, our results include LAEs that are fainter in the far-infrared, which have IRX that are in the range from the Calzetti et al. (2000) to the Meurer et al. (1999) and SMC (Gordon et al., 2003) curves. Our results are broadly consistent with the previous studies on LBGs at similar redshifts by Álvarez-Márquez et al. (2016); Barisic et al. (2017); Koprowski et al. (2018) and Fudamoto et al. (2020).

The work in this chapter supports the assertion in Chapter 2 that deeper IR data were required to probe the IRX-$\beta_{\rm UV}$ for the majority of LAEs. However, there are a number of LAEs that were not detected in ALMA observations that have upper limits on IRX that are significantly below the local relations (i.e., ALMA detections should have been expected). There may be systems for which our SED assumptions are incorrect, or galaxies that contain unusual dust (e.g., Popping et al., 2017).

3.3.5 Impact of M_* on SFR and $f_{\rm esc}$(Lyα)

The total stellar mass (M_*) of a galaxy encompasses its history of star formation and structural growth. We next examine the SFR-M_* relation with SFRs updated with the inclusion of ALMA data, and study the influence of M_* on $f_{\rm esc}$(Lyα) for ALMA-observed LAEs by utilizing the M_* calculated from SED fitting by Santos et al. (2020).

3.3.5.1 The stellar mass-SFR main sequence

We study the SFR-M_* relationship for the dust-detected LAEs and also examine the potential evolution of this relationship with redshift. We utilize SFR$_{\rm IR}$ (Section 3.3.2), photometric redshift and M_* from Santos et al. (2020). Furthermore, we compare our far-infrared based SFR-M_* relation with the SFR$_{{\rm Ly}\alpha}$-based relation for the same LAEs from Santos et al. (2020) which was derived using apparent Lyα luminosity and EW to correct for $f_{\rm esc}$(Lyα). The SFR-M_* relation for our sample and its comparison with the main sequence (Speagle et al., 2014) at $z = 3$ and 6 is shown in Figure 3.7. As expected, there is a strong correlation between SFR$_{\rm IR}$ and M_* in our data. These LAEs scatter around the $z = 3$ main sequence, which is consistent with the SFR-M_* relation for our sample being similar to that of normal star-forming galaxies at same redshift. However, the main sequence has a scatter of 0.2 dex (Speagle et al., 2014), while our SFR$_{\rm IR}$ has a systematic uncertainty of 1.8 dex as the dust temperature (Section 3.3.2.1 and Figure 3.4) is poorly constrained due the dearth of far-infrared data on shorter wavelength regime. Our ALMA-detected LAEs have a scatter of up to ∼1 dex, suggesting that their far-infrared SEDs may lie within the range covered by Sd to M82 templates, but may not cover the range.

The dust-detected LAEs are typically more massive than the whole SC4K sample, as illustrated in Figure 3.8. However the sample consist of only 15 LAEs

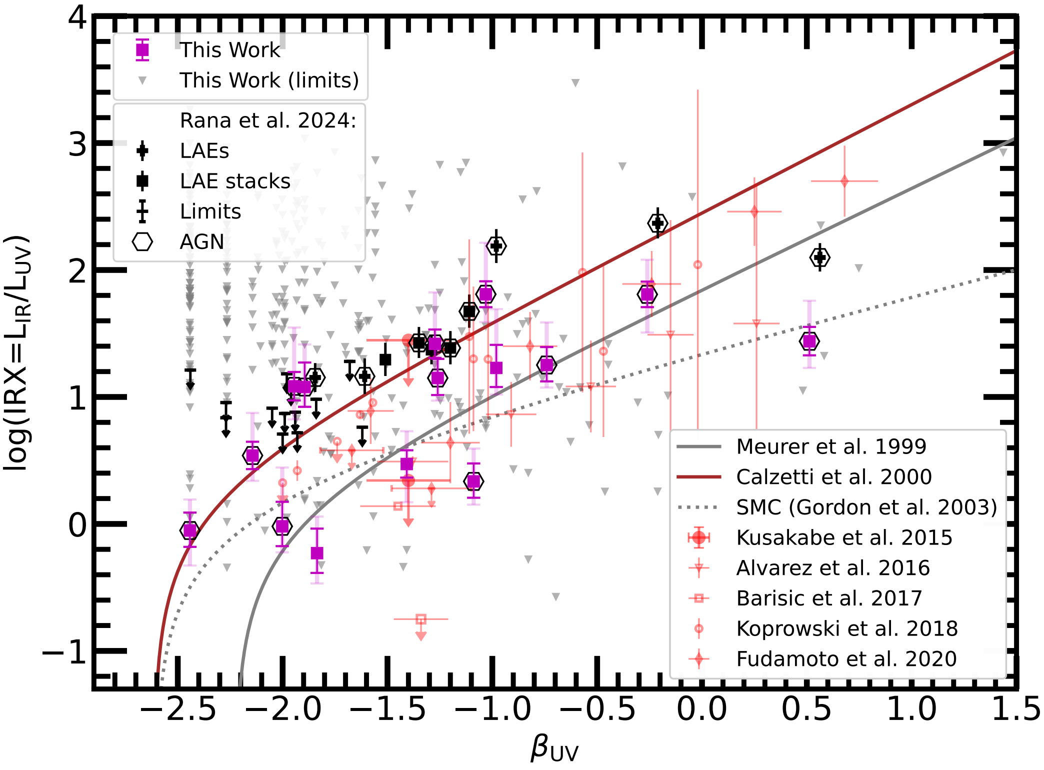

Figure 3.6: The dust extinction plane (IRX-$\beta_{\rm UV}$) for LAEs. ALMA detections and observations for LAEs in this study are represented by magenta squares and inverted grey triangles. Dark errorbars show the statistical uncertainties and faint errorbars show the systematic uncertainty due to SED uncertainty. Black symbols depict IRX-$\beta_{\rm UV}$ values for individual LAEs, stacks of LAEs, and upper limits on IRX-$\beta_{\rm UV}$ from single-dish far-infrared data (Chapter 2). AGN presence in both this study and measurements from Chapter 2 are indicated. Dust extinction curves for local starburst and star forming galaxies (Meurer et al., 1999; Calzetti et al., 2000) and SMC (Gordon et al., 2003) are shown. The IRX-$\beta_{\rm UV}$ values for LBGs at similar redshifts reported in previous studies by Álvarez-Márquez et al. (2016); Barisic et al. (2017); Koprowski et al. (2018) and Fudamoto et al. (2020) are indicated and IRX-$\beta_{\rm UV}$ upper-limits for LAEs at $z = 2.2$ from Kusakabe et al. (2015) are marked. Our results support the claim in Chapter 2 that deeper IR observations were needed to probe the IRX-$\beta_{\rm UV}$ relation, and show that LAEs follow similar IRX-$\beta_{\rm UV}$ relation to other star-forming galaxies such as LBGs.

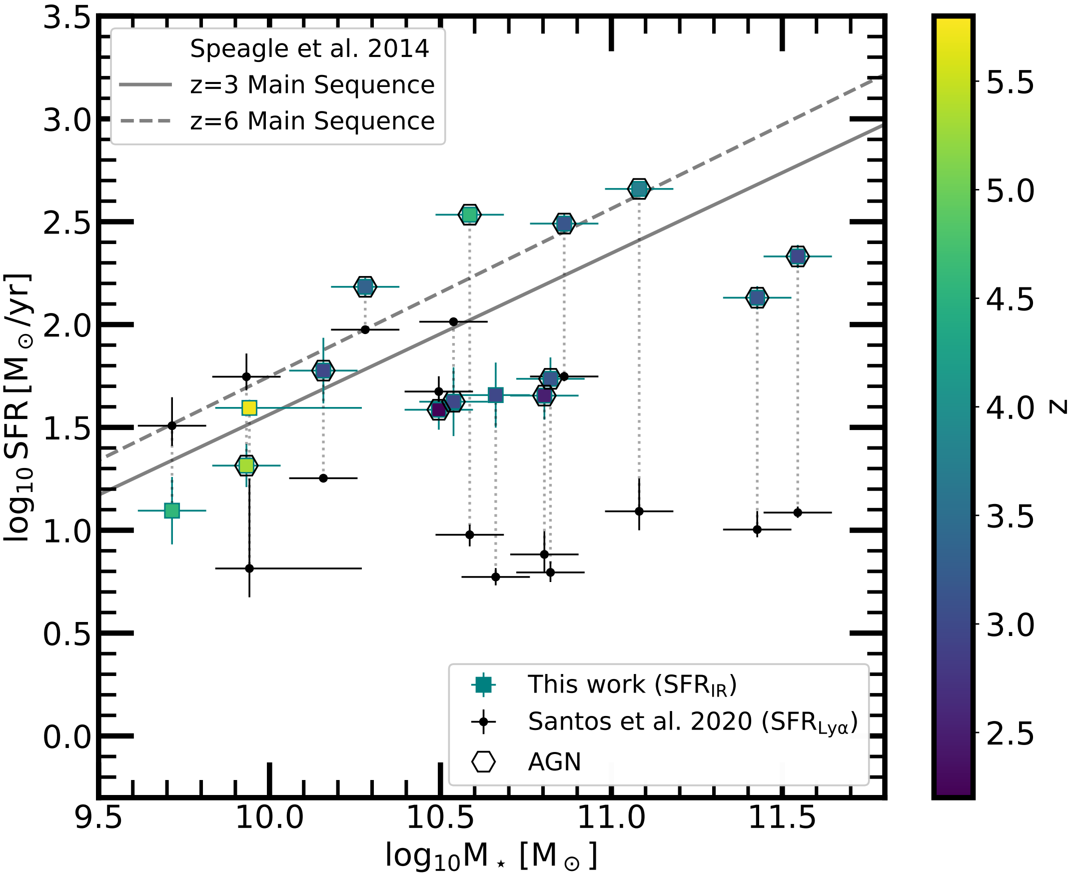

Figure 3.7: Comparison of SFR-M_* relation for ALMA-detected LAEs with galaxy main sequence at $z = 3$ and 6 from Speagle et al. (2014) which are extrapolated at both ends ($\log M_*/M_\odot = 9.7$–11.1) and have a scatter of ±0.2 dex each. Coloured squares depict SFR$_{\mathrm{IR}}$ for the ALMA detected LAEs and dust-corrected SFR$_{\mathrm{Ly}\alpha}$ for the same LAEs are shown by connected circles (Santos et al., 2020). The colour scaling shows the redshift of each source. LAEs that host AGN are highlighted. SFR$_{\mathrm{IR}}$ has a typical systematic uncertainty of 1.8 dex due the choice of SED (Section 3.3.2). The gap between SFR$_{\mathrm{IR}}$ and SFR$_{\mathrm{Ly}\alpha}$ widens with stellar mass, indicating that higher-mass LAEs are dustier. This suggests significant dust-obscured star formation in massive LAEs, highlighting the limitations of UV and Lyα tracers without accounting for dust.

which include 12 AGN so caution is advised. For the same LAEs the main sequence inferred from $\mathrm{SFR}_{\mathrm{Ly}\alpha}$ from Santos et al. (2020) is shallower than our dust-obscured $\mathrm{SFR}_{\mathrm{IR}}$. The difference between $\mathrm{SFR}_{\mathrm{IR}}$ and $\mathrm{SFR}_{\mathrm{Ly}\alpha}$ increases for higher mass LAEs, which implies that higher mass LAEs contain more dust than lower mass system and that the EW-based $f_{\mathrm{esc}}(\mathrm{Ly}\alpha)$ is less reliable for more massive LAEs. These results are consistent with Santos et al. (2020), who reported the deviation between $\mathrm{SFR}_{\mathrm{SED}}$ and $\mathrm{SFR}_{\mathrm{Ly}\alpha}$ at the high mass end. However, Santos et al. (2020) did not directly observe the obscured SFR due to lack of far-infrared data, instead they derived $\mathrm{SFR}_{\mathrm{SED}}$ by inferring amount of dust from the UV-optical slope. This indicates that Lyα may not be a reliable SFR tracer for high mass galaxies. One possible cause for this behaviour is that, as galaxies grow larger, their evolved stellar populations produce more dust, which absorbs Lyα photons and results in an underestimation of SFR in these galaxies. Moreover, it is also possible that the Lyα and dust emission originate from different regions within a galaxy. The deviation between $\mathrm{SFR}_{\mathrm{IR}}$ and $\mathrm{SFR}_{\mathrm{Ly}\alpha}$ implies that we need to combine multi-wavelength observations to accurately measure the SFR in LAEs of different mass. As shown in Figure 3.7, this difference can be as high as 2 dex for high-mass LAEs.

3.3.5.2 $f_{\mathrm{esc}}(\mathrm{Ly}\alpha)$-$M_*$ relation

The connection between the Lyman-alpha escape fraction and stellar mass is shown in Figure 3.8. We use $f_{\mathrm{esc}}(\mathrm{Ly}\alpha)$ derived from the ALMA measurements (described in Section 3.3.3) and M_* from Santos et al. (2020). Our results show that ALMA-detected LAEs are typically more massive than the overall SC4K LAE population and are likely to have higher $f_{\mathrm{esc}}(\mathrm{Ly}\alpha)$. This observation, along with the lower limits on $f_{\mathrm{esc}}(\mathrm{Ly}\alpha)$ for ALMA observed LAEs suggest that there may be a correlation between M_* and $f_{\mathrm{esc}}(\mathrm{Ly}\alpha)$. Furthermore, most of the high-mass LAEs are detected, and those that are not detected tend to have lower limits that are higher than their lower mass counterparts. One possible explanation for this pattern is that the dust in LAEs is patchy (e.g., Scarlata et al., 2009; Duval et al., 2014) which allow Lyα photons to escape. Moreover, while Lyα emission traces recent star formation (Dijkstra & Westra, 2010; Sobral et al., 2018), dust

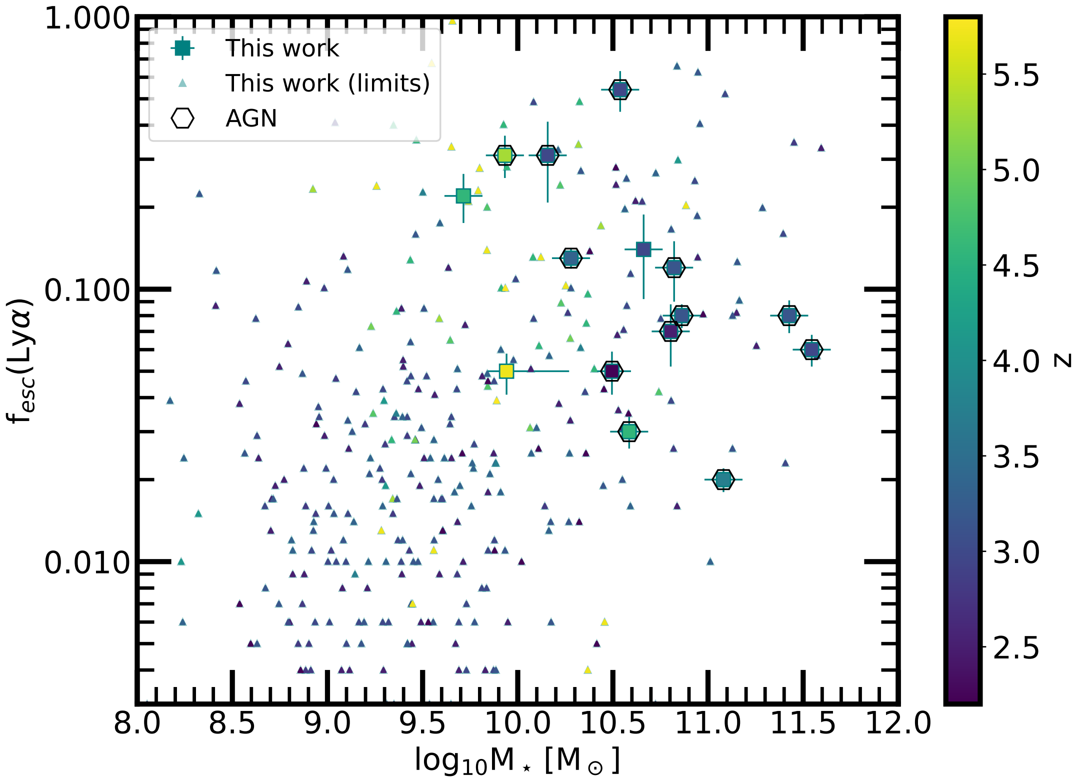

Figure 3.8: $f_{\mathrm{esc}}(\mathrm{Ly}\alpha)$ as a function of M_* for SC4K LAEs that have been observed by ALMA. Symbols are coloured by redshift and lower limits are represented by triangles. LAEs that host AGN are highlighted. ALMA-detected LAEs are typically more massive and likely have higher $f_{\mathrm{esc}}(\mathrm{Ly}\alpha)$ than the overall SC4K LAE population, suggesting a potential correlation between M_* and $f_{\mathrm{esc}}(\mathrm{Ly}\alpha)$. Most high-mass LAEs are detected, while undetected ones have higher $f_{\mathrm{esc}}(\mathrm{Ly}\alpha)$ limits than lower-mass LAEs, possibly due to patchy dust that allows Lyα photon escape.

emission is associated with slightly older stellar populations (Mallory et al., 2022; Werle et al., 2024). This difference suggests that the spatial distribution of Lyα and dust emitting regions may not always overlap, resulting in a higher $f_{\mathrm{esc}}(\mathrm{Ly}\alpha)$ in high-mass LAEs.

3.4 Conclusions

We have analysed far-infrared properties of SC4K LAEs at $z = 2$–6 using ALMA archive data from A^{3}COSMOS. With 627 observations of 375 LAEs, including 119

AGN, we identified 15 detections of dust continuum emission from this population. Our results show that most of the detections are within the high-sensitivity region of the ALMA beam, predominantly in Bands 6 and 7 which is in agreement with the expected peak of dust emission for LAEs at the redshift range of $z = 2$–6, which lies at 300–700 μm. We estimated $L_{\rm IR}$ by fitting a modified-blackbody model with parameters α=2, $\beta_{\rm dust}$=1.96 and $T_{\rm dust}$ = 40 K to infer other far-infrared properties such as SFR$_{\rm IR}$. Our key finding are as follows:

1. We identified 15 LAEs in ALMA far-infrared data with a SNR $\geq$4.35 that show dust continuum emission, including 12 AGN. The derived $L_{\rm IR}$ and SFR$_{\rm IR}$ of these LAEs are $10^{11.1} - 10^{12.6}$ $L_\odot$ and 12 – 456 $M_\odot\,{\rm yr}^{-1}$, respectively.

2. We estimated the $f_{\rm esc}$(Lyα) for ALMA detected and observed LAEs by combining dust-uncorrected SFR$_{{\rm Ly}\alpha}$ and SFR$_{\rm UV}$ with SFR$_{\rm IR}$. Our $f_{\rm esc}$(Lyα) measurements, range from 2 to 54% and are consistent with previous studies that used same method, as well as those employing different approaches. The significant systematic uncertainties in $f_{\rm esc}$(Lyα) arise primarily from the lack of ALMA photometric data points to constrain the shape of SED.

3. We calculated IRX values for our detections as 0.6 to 65 and compared them with dust extinction curves. Our IRX-$\beta_{\rm UV}$ values range from Calzetti et al. (2000), typical star-forming galaxies with near-solar metallicities, the Meurer et al. (1999), UV-bright starburst galaxies with lower metallicities than the Calzetti et al. (2000) to the SMC curve (Gordon et al., 2003) which depicts young and evolved stellar populations with much lower metallicities. These results are consistent with previous studies, including Kusakabe et al. (2015) and Chapter 2.

4. The SFR-M_* relation for dust-detected LAEs was found to be consistent with the main sequence at a similar redshift. However, the SFR$_{\rm IR}$-M_* relation is steeper than equivalent SFR$_{{\rm Ly}\alpha}$ for the same galaxies in high mass LAEs, suggesting that there is a significant dust obscuration that is not accounted for with standard UV-only analysis. This indicates the need for

multi-wavelength observations to estimate true star-formation in LAEs, as the $\mathrm{SFR}_{\mathrm{Ly}\alpha}$ estimate can be ∼2 dex lower than the true values.

5. An investigation into the relationship between $f_{\mathrm{esc}}(\mathrm{Ly}\alpha)$ and stellar mass reveals a potential correlation, further supporting the suggestion that the spatial distribution of dust in LAEs is likely to be patchy.

Chapter 4

Constraining molecular gas content in LAEs using ALMA observations

4.1 Introduction

In this chapter, we explore the molecular gas content in LAEs using submillimetre data. As LAEs are star-forming galaxies, they are expected to be rich in gas. One commonly used method to constrain gas content in star-forming galaxies utilizes the dust to gas mass ratio derived utilizing far-infrared continuum as a gas tracer (e.g., Leroy et al., 2011; Magdis et al., 2012; Scoville et al., 2014, 2016). However, LAEs are outliers to this relationship which has not yet been tested for LAEs. As we have seen, LAEs are young galaxies with faint dust continuum and as carbon monoxide (CO) molecules and neutral carbon ([C I]) also depend on ISM enrichment and dust shielding to survive (Wolfire et al., 2010; Glover & Clark, 2012), low dust content (Trainor et al., 2016; Izotov et al., 2024) implies that these indirect tracers are expected to be scarce in LAEs (Hunt et al., 2017; Coogan et al., 2019).

Previous studies have attempted to detect molecular gas in galaxies similar to LAEs but with mixed success. For example, Davies et al. (2010) used the Australia Telescope Compact Array (ATCA) to search for CO(1–0) and CO(2–1) in low-mass Lyman-break galaxies (LBGs) and managed to establish upper limits only. On the other hand, Magdis et al. (2017) reported the detection of CO(3–2) in a more massive LBG using the IRAM 30m telescope, indicating that the detection of molecular hydrogen may depend on galaxy mass or star formation efficiency. However, direct constraints on the molecular and atomic gas content of LAEs remain largely unexplored.

In this work, we use far-infrared emission lines in LAEs covered by ALMA, in order to determine which emission lines or CO transitions are present and how bright they are. This analysis will help us to probe physical conditions of the ISM and estimate the amount of molecular gas in LAEs. Additionally, by analysing how the gas mass fraction changes with redshift and stellar mass, we can gain insights into how LAEs evolve as they grow and what their likely evolutionary path might be. In this study, we search the ALMA observations for spectral coverage of far-infrared emission lines in LAEs, including multiple CO transitions, [C I] 609, [C I] 370, [C II] 158, and [N II] 205. As these lines are crucial to constrain gas content and and provide key information about the ISM in LAEs, we aim to enhance our understanding of the physical conditions of their ISM and gas.

This chapter is structured as follows: in Section 4.2, we describe the LAEs and ALMA archival data used in this analysis. Our results and analyses are presented in Section 4.3. We summarise our conclusions in Section 4.4. Throughout this chapter, we adopt a flat ΛCDM cosmology with $H_0 = 67.66\,\mathrm{km\,s^{-1}\,Mpc^{-1}}$, $\Omega_m = 0.31$, and $\Omega_\Lambda = 0.69$, based on the *Planck* 2018 satellite results (Planck Collaboration et al., 2020).

4.2 Data

In this study, we probe the gas content of a sample of LAEs in the COSMOS field using far-infrared observations from the ALMA archive.

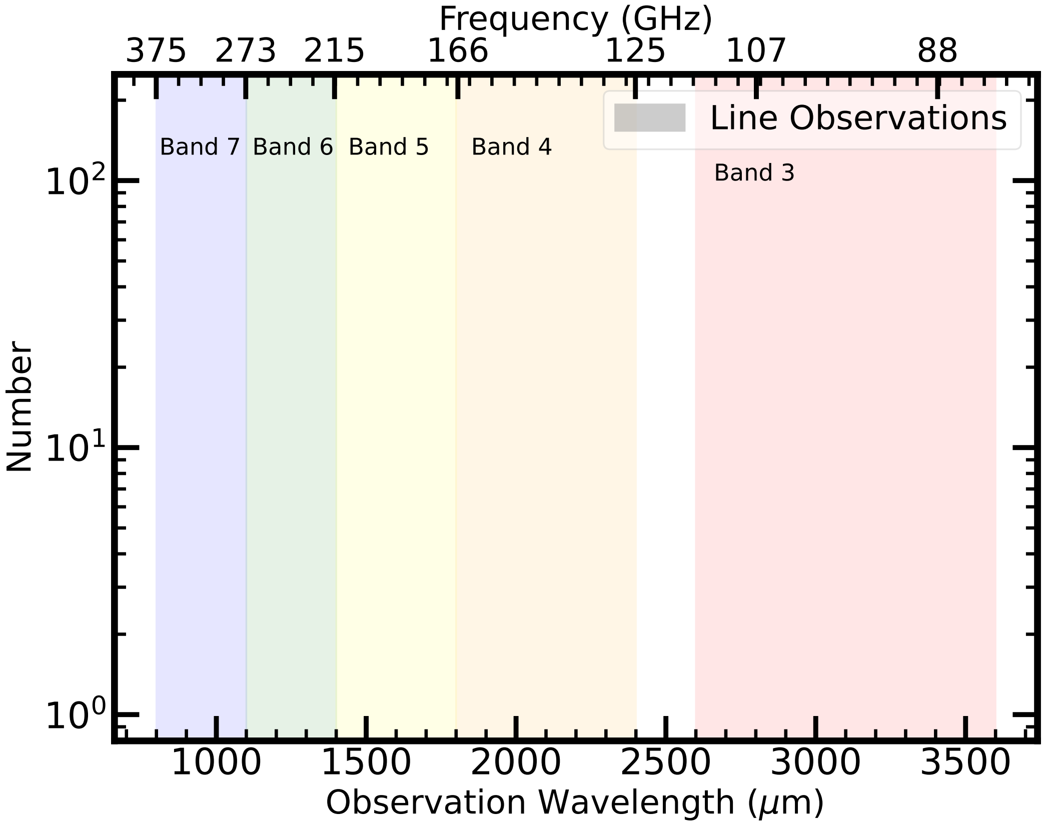

Figure 4.1: Distribution of LAEs with the spatial coverage across different ALMA Bands. The figure includes all LAEs with at least one overlapping ALMA observation, where a single LAE can be associated with multiple emission lines and a single line can have multiple observations. Bands 3, 4, 5, 6, and 7 are represented in faded red, orange, yellow, green, and blue, respectively. No coverage is found in Band 5.

4.2.1 Lyα Emitters dataset

We utilise the same sample (as in Chapters 2 and 3) of ∼4000 LAEs in the COSMOS field from the SC4K survey (Sobral et al., 2018). The sample spans a photometric redshift range of $z = 2.22$ to 5.78 and has a median SFR$_{\mathrm{Ly}\alpha}$ of 6.21 $M_\odot\,\mathrm{yr}^{-1}$, suggesting active star formation, as expected in LAEs. The redshifts have high precision since they include narrow- or medium-band coverage of Lyα emission.

4.2.2 ALMA Data

The COSMOS field is well covered by multi-wavelength observations, including a significant number of ALMA observations. To investigate the gas content of LAEs through their far-infrared emission lines, we use the ALMA Archive Mining and Visualization Toolkit (ALMINER; Ahmadi & Hacar, 2023) to search the ALMA archive.

We begin by utilising the `catalog` search function in ALMINER to asses the spatial coverage in order to check whether the position (RA, Dec.) of each SC4K LAE has been observed by any existing ALMA observations. This allows us to identify archival datasets that potentially include far-infrared emission lines for these LAEs. To confirm whether these observations also cover the relevant spectral range, we next use the `line_coverage` function in ALMINER. This function takes the output of the `catalog` search function, the rest-frame frequency (GHz) of the emission line of interest, and the redshift of each source, in our case, the photometric redshifts provided by the SC4K survey, as inputs. It then determines whether the specified emission line would fall within the spectral coverage of the available ALMA observations. This two-step process enables us to identify archival ALMA datasets with both spatial and spectral coverage suitable for studying far-infrared line emission from LAEs in the SC4K sample.

We focus on the following emission lines: [C I] 609, [C I] 370, [C II] 158, [N II] 205, and CO transitions such as CO(3–2), CO(4–3), CO(5–4), CO(6–5), CO(7–6), and CO(8–7)—as the redshift range of our LAEs (z =2.22–5.78) suggests that these lines may fall within the spectral coverage of existing ALMA observations. This makes them suitable targets for identifying potential detections in archival ALMA data.

Starting with spatial coverage, we identify a total of 574 ALMA observations overlapping with our LAE sample, covering Bands 3, 4, 6 and 7 as shown in Figure 4.1. Notably, no LAEs are covered by ALMA observations in Band 5. These 574 observations correspond to 364 emission lines in 349 LAEs, including 46 lines associated with 45 AGN. The comparison of the Lyα luminosity distribution for the SC4K sample, ALMA observed LAEs and AGN is illustrated in Figure 4.3. This comparison shows that the distribution of observed LAEs is similar to that

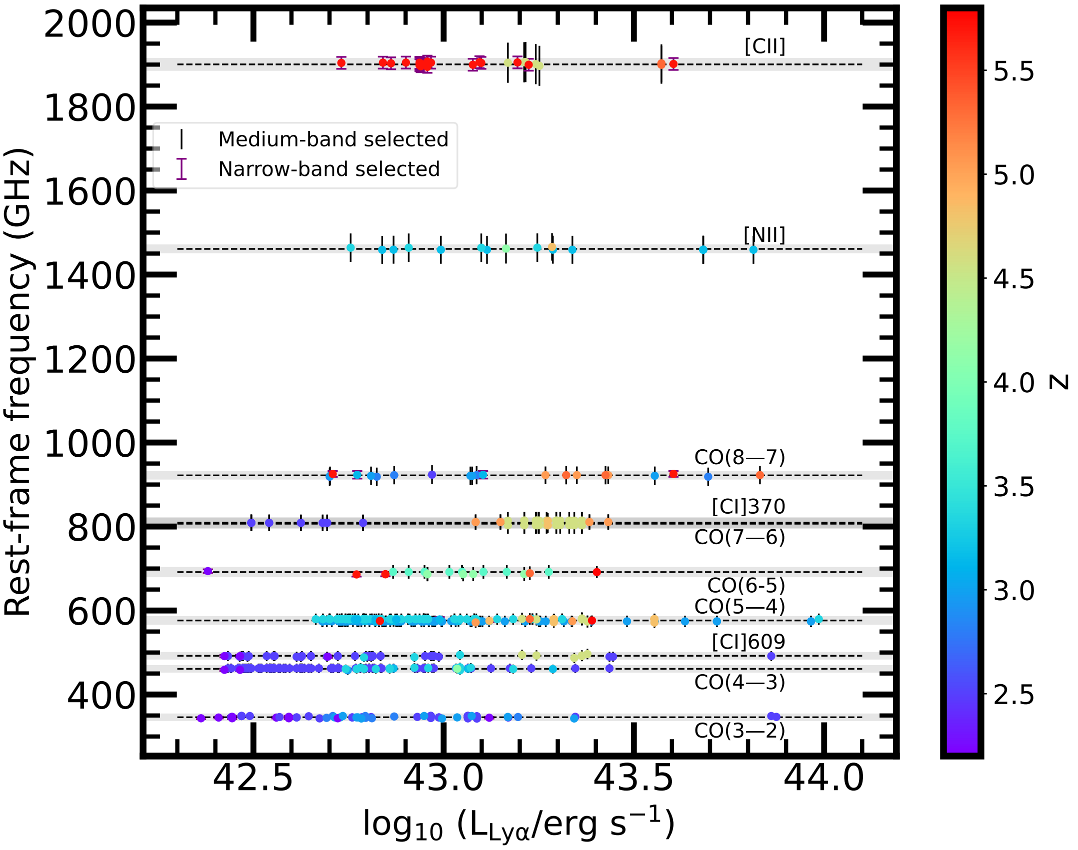

Figure 4.2: Comparison of rest-frame frequency uncertainties of target emission lines compared to the width of two consecutive ALMA spectral windows (i.e. a baseband, shaded as a function of LAE Lyα luminosity). Each point represents an emission line observation with redshift indicated by colour. Errorbars represent uncertainties in expected line frequency based on the narrow/medium band photometric redshift errors. The overlap between the shading and errorbars provide a reference to assess whether the frequency uncertainty lies within the expected spectral coverage of each observation. This figure also shows the typical redshift of sources with potential coverage of different lines. For example [C II] is only available for high redshift LAEs, and CO(3–2) only at low redshift, due to the most popular ALMA bands for COSMOS observations.

of SC4K sample, whereas the distribution of observed AGN is dominated by the sources that are brighter than the average Lyα luminosity of the SC4K sample. Thus our sample with spatial ALMA coverage has a bias toward AGN, particularly those with higher Lyα luminosities.

Due to the nature of ALMA's frequency setup, where each Band is divided into spectral windows (SPWs) that may include gaps in frequency coverage, most observations do not provide continuous spectral coverage across the entire frequency range of a Band, except when conducted in scan mode. Therefore, we next assess whether lines with spatial coverage fall within ALMA's spectral windows. In ALMA, a Spectral Window (SPW) is a frequency chunk within a baseband, used to observe specific spectral features. Each baseband can host up to 4 SPWs, and multiple basebands operate within a band. Figure 4.2 shows a plot of Lyα luminosity, rest-frame frequency of the line of interest, and redshift for 574 observations. For each line, we convert the central frequencies of two consecutive ALMA spectral windows to the rest-frame utilising the median photometric redshift of the target LAE. We compare these with the expected line frequency using the photometric redshift and associated uncertainty of the LAE from the SC4K. By doing this, we are able to assess whether each target line falls within spectral windows, represented by grey bars. This analysis helps to determine how many lines are likely to be spectrally covered in the archival data, despite the redshift uncertainties.

We apply spectral coverage checks by employing `line_coverage` function of ALminer and compare the uncertainties in expected observed frequencies—calculated by propagating photometric redshift uncertainties—with the widths of individual SPWs, basebands, and full ALMA Bands in case of spectral scan mode (Figure 4.4). This comparison allows us to determine whether the redshift uncertainty is small enough for the target line to be confidently captured within a spectral setup– i.e. when the frequency width of the observation is bigger than the frequency covered by redshift uncertainty. In the case of spectral scans, the full Bands provide spectral coverage for a line. This analysis results in a sample of 45 observations of LAEs with spectral coverage of one or more line. During data retrieval, we find that two LAEs with 3 observations fall near the edge of the primary beam and lack sufficient spatial coverage: these observations are

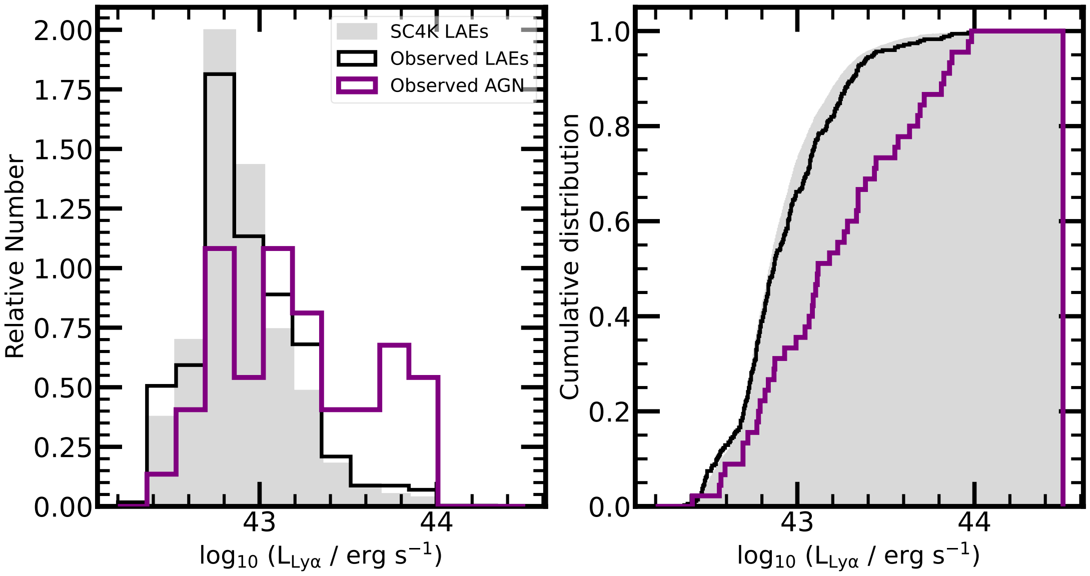

Figure 4.3: Comparing differential (left) and cumulative (right) histograms of Lyα luminosity distributions for the full SC4K sample, and LAEs, AGN that are observed with ALMA at any frequency. The SC4K and ALMA-observed LAEs have similar distributions, indicating that the ALMA archival LAE observations are randomly distributed, given that most of the LAEs were not targeted. In contrast, the observed LAEs that host AGN are systematically brighter in Lyα compared to the overall population (Calhau et al., 2020), implying a selection bias in these cases.

excluded from the sample, leaving 42 ALMA observations covering 35 distinct emission lines in 34 LAEs, including 3 AGN (see Table 4.1). Notably, one LAE (SC4K-IA679-43367) is observed in two different emission lines, namely [C I] 609 and CO(5–4).

4.2.3 Identifying emission line candidates for LAEs

For our spectral line search across these 34 sources, we use archival, continuum-subtracted, primary beam-corrected data cubes and the corresponding primary beams. We obtain the data directly from the ALMA Science Archive, covering observations from 2012 to 2022. As we have 42 observations for 34 sources, we select only the most sensitive data cube when multiple observations are available for a given source. The selection is based on line sensitivity at a velocity resolution of 10 km s^{-1} (`line_sens_10kms`, defined as the root mean square noise in μJy beam^{-1}). The selected cubes have `line_sens_10kms` values ranging from 448 to 21,169 μJy beam^{-1} (median: 1653 μJy beam^{-1}), angular resolutions ranging from 0.05″ to 12″ (median: 1.43″), and primary beam correction (sensitivity in the ALMA field of view) values from 0.37 to 1.0 (median: 0.74). All cubes have passed ALMA's Quality Assurance Level 2 (QA2) test and show flat baselines in line-free channels, confirming their suitability for spectral line analysis.

We begin the spectral extraction process using the non-primary beam-corrected data cubes generated from the primary-beam-corrected cubes and the primary beam. We take this step because primary beam correction boosts the noise in the outskirts of the cubes, which affects the statistics and can make noise peaks appear similar to real sources. However, once lines are identified we use the primary beam corrected cubes for accurate flux density measurements in the final analysis. To identify lines, we use the CASA task `specflux` to extract the 1D spectrum at the position (RA, Dec.) of each LAE. The extraction aperture is determined based on the angular size of the synthesized beam. If both the major and minor axes of the synthesized beam are greater than or equal to 0.5 arcseconds then we expect the LAE to be unresolved and we use the synthesized beam itself as the elliptical aperture for flux measurement. If either axis is smaller than 0.5 arcseconds, we utilise a fixed circular aperture with a diameter of 0.5 arcseconds

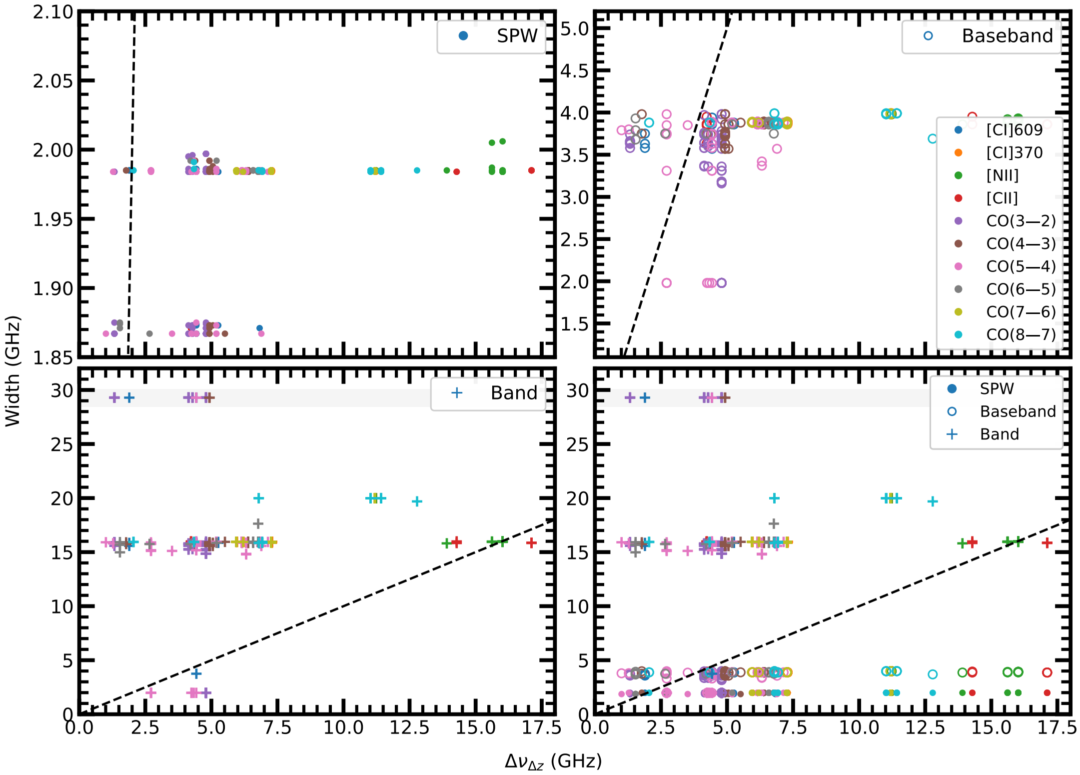

Figure 4.4: Assessment of spectral coverage for ALMA observations using photometric redshift uncertainties. The top-left panel compares the uncertainty in the expected observed frequency of each line ($\Delta\nu_{\Delta z}$) with the width of individual SPWs, shown as filled circles. The top-right panel shows the same comparison using the width of two consecutive SPWs (basebands), represented by unfilled circles. The bottom-left panel compares the frequency uncertainty with the full ALMA Band width, where spectral scan observations appear as horizontal grey bands and are marked with plus symbols. The bottom-right panel combines all three comparisons in a single plot. Symbols are colour-coded by emission line. Dashed one-to-one lines in each panel indicate where the uncertainty in the expected observed frequency matches the spectral width of the setup shown—SPWs, basebands, or full Bands (only spectral scans are relevant as there are gap/s in Bands for other setups). Observations appearing above these lines have frequency uncertainties smaller than the corresponding spectral coverage.

Table 4.1: Summary of LAEs with both spatial and spectral coverage of far-infrared emission lines. The table lists the number of ALMA observations and corresponding number of LAEs observed per emission line, along with the rest-frame frequency of each line.

Line	$\nu_{\rm rest}$ (GHz)	No. of Observations	No. of LAEs
[C I] 609	492.161	2	2
CO(3–2)	345.796	20	15
CO(4–3)	461.041	4	4
CO(5–4)	576.268	10	9
CO(6–5)	691.473	4	3
CO(8–7)	921.800	2	2
Total		42	35[a]

[a] One source is observed in two different emission lines; therefore, the total includes 35 line observations from 34 LAEs.

to ensure that all emission is captured. In all cases, the aperture is centered at the LAE coordinates, and the position angle is set to zero degrees.

Table 4.2: Potential emission lines with SNR > 3.1, corresponding to a false detection rate of ≤ 50%.

SC4K ID	Line	z[b]	ν_{obs}[c] (GHz)	FWHM ($\mathrm{km\,s^{-1}}$)	Flux[d] ($\mathrm{Jy\,km\,s^{-1}}$)	SNR[e]	pbcor[f]	Detection[g]
SC4K-IA427-167426[h]	*CO(3–2)*	*2.50*	*113.04*	*700±150*	*0.79±0.13*	*6.1*	*0.53*	*N*
SC4K-IA427-79391[i]	*CO(3–2)*	*2.50*	*92.91*	*160±50*	*0.17±0.04*	*4.2*	*0.59*	*N*
SC4K-IA464-50321	CO(3–2)	2.608	95.83	440±120	0.20±0.05	4.0	0.87	Y
SC4K-IA427-40442[j]	CO(3–2)	2.781	91.46	230±70	0.22±0.04	5.5	0.56	T
SC4K-IA427-70144[j]	CO(3–2)	2.830	90.28	340±110	0.16±0.04	4.0	0.85	T
SC4K-IA484-111739	CO(3–2)	3.040	85.60	200±70	0.33±0.08	4.1	1.00	Y
SC4K-IA484-12936	CO(3–2)	3.059	85.20	700±310	0.37±0.09	4.1	0.83	Y
SC4K-IA505-158978[n]	CO(4–3)	3.177	110.38	660±90	0.46±0.07	6.6	0.99	Y
SC4K-IA527-212136	CO(4–3)	3.530	101.79	550±160	0.28±0.08	3.5	0.69	Y
SC4K-IA679-78545[i]	*CO(5–4)*	*4.58*	*112.10*	*190±40*	*0.30±0.08*	*3.8*	*0.66*	*N*
SC4K-IA679-43367	CO(5–4)	4.674	101.57	170±40	0.29±0.06	4.8	0.58	Y
SC4K-NB816-459515[i,n]	*CO(8–7)*	*5.70*	*140.42*	*90±30*	*0.04±0.01*	*4.0*	*1.00*	*N*

[b] Emission line based redshift (three decimals); in case of non-detection the photometric redshift (two decimals) from Sobral et al. (2018) is used.

[c] Observed emission line frequency, whose reliability depends on the confidence of the line detection.

[d] Integrated line flux $S_{\mathrm{line}}\Delta v$, calculated using the 3σ area under the Gaussian profile.

[e] Signal-to-noise ratio calculated from the integrated flux and the corresponding line noise.

[f] Primary beam correction factor at the position of an LAE in the ALMA observation.

[g] Detection flags: N — non-detection (shown in italics); T — tentative detection; Y — confirmed detection determined as described in Section 4.2.3.1.

[h] The line is near the edge of the SPW, where the data is often noisy, and the observed line redshift is outside the range of the photometric redshift uncertainty (filter FWHM; see Figure 4.5 and Figure 4.6).

[i] The redshift of the observed line lies outside the photometric redshift uncertainty range, and visual inspection shows the spectrum is noisy (see Figure 4.5 and Figure 4.6).

[j] SNR ≥ 4 (<10% false detection rate), but the redshift of the observed line lies outside the photometric redshift uncertainty; thus, the line is classified as a tentative detection (see Figure 4.5 and Figure 4.6).

[n] LAE also detected in dust continuum emission with ALMA (Chapter 3).

We apply spectral line fitting to extracted 1D spectra from the non-primary-beam-corrected cubes for each LAE. Our procedure is similar to the approach described in Cooke et al. (2018). We begin by smoothing the extracted spectra through spectral re-binning. Each spectrum is re-binned using a sequence of increasing velocity bin sizes: 15, 25, 50, 75, 100, 150, and 200 km s^{-1}, starting from the bin size closest to the native spectral resolution. For each binning level, we compute the standard deviation of the flux density across the spectra and use this to calculate the signal-to-noise ratio (SNR) at each frequency. Potential line candidates are identified for further examination by locating peaks with SNR ≥ 2 in the re-binned spectra. We exclude any candidates that fall within six channels of the SPW edges, which are typically particularly noisy. 1D Gaussian line profiles are then fitted to the remaining line candidates and we integrate the line flux (in $\mathrm{Jy\,km\,s^{-1}}$) over the range covered by 3σ of the fitted line width (covering 99.7% of the Gaussian profile). The uncertainty in the integrated flux is calculated over the same spectral range and is estimated by excluding the line region and measuring the root-mean-square noise within a maximum range of 1 GHz on either side of the fitted line. In cases where two line candidates have spectral overlap of >=85% (e.g. originating from the same broad line), we retain only the candidate with the higher integrated flux SNR (integrated flux divided by integrated noise).

To assess the reliability of detected features, we repeat the entire procedure on inverted spectra (i.e., multiplied by -1) to identify negative line candidates. These negative detections are then used to estimate the false detection rate (FDR) associated with our line search (since no absorption lines are expected). The FDR is calculated by comparing the number of positive line candidates (identified in the original spectra) to the number of negative candidates (identified in the inverted spectra) as a function of SNR. This approach provides an empirical estimate of the likelihood that a given detection is spurious, which depends on its SNR. We combine the SNR values and corresponding FDR estimates for all line candidates identified across all re-binned spectra. From this distribution, we determine that a SNR threshold of 3.1 corresponds to FDR of approximately 50%, while SNR of 4.0 provides FDR of just 10%. These values are used to select robust and tentative line detections. 12 lines in 12 LAEs meet or exceed the 3.1σ SNR thresholds. For these selected candidates, we re-extract the spectra and re-measure the flux

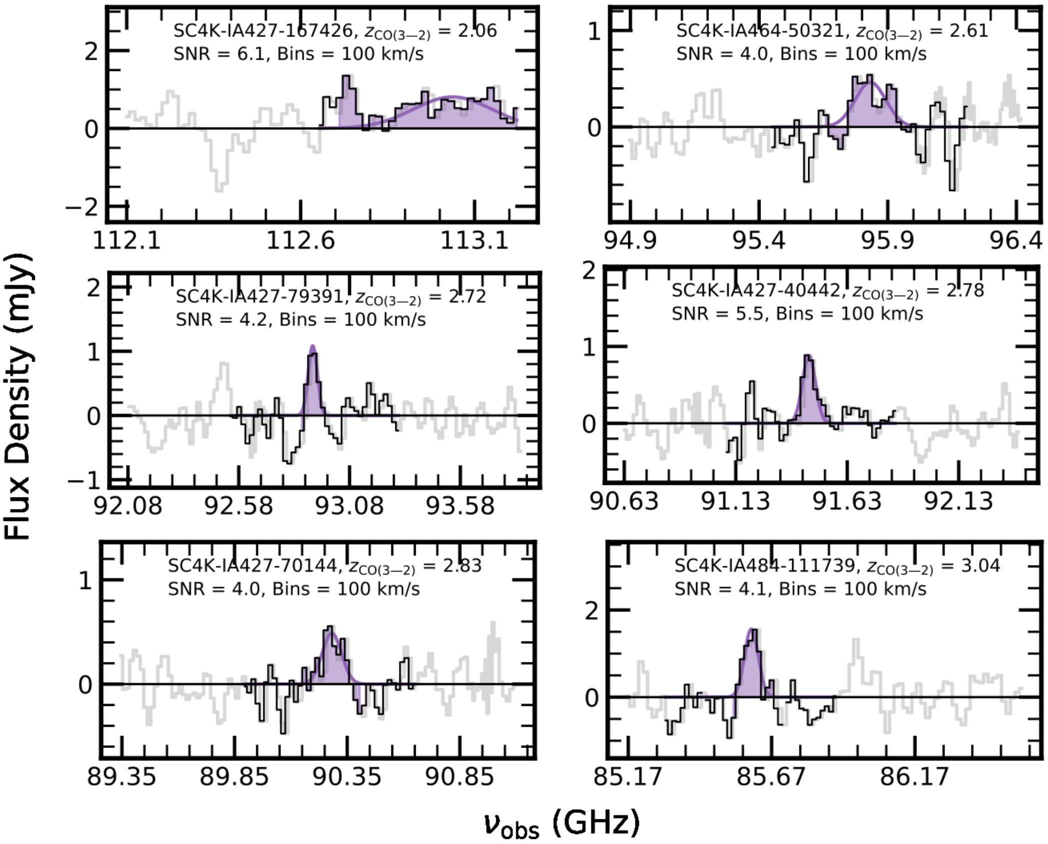

Figure 4.5: Spectral lines and fits for all potential detections with SNR > 3.1 (corresponding to a false detection rate of ≤ 50%). The spectra are extracted and fitted using the primary beam-corrected data cubes. Each plot corresponds to an individual line with shaded regions indicating the 3σ range of the best-fit Gaussian profile. These shaded regions are used for integrated flux and noise estimation. The LAE ID, redshift (derived from the fitted line), signal-to-noise ratio, and bin size (in $\mathrm{km\,s^{-1}}$) are indicated in the legend above each panel. The Gaussian fits are performed using the same bin size in which the line was originally detected with the highest SNR in the non-primary-beam-corrected data. Grey lines show the native binning, while the rebinned spectra are shown in black. Despite high SNR, the CO(3–2) line from LAE SC4K-IA427-167426 is likely a false detection, as it lies near the noisier SPW edge. LAE SC4K-IA484-111739 hosts an AGN.

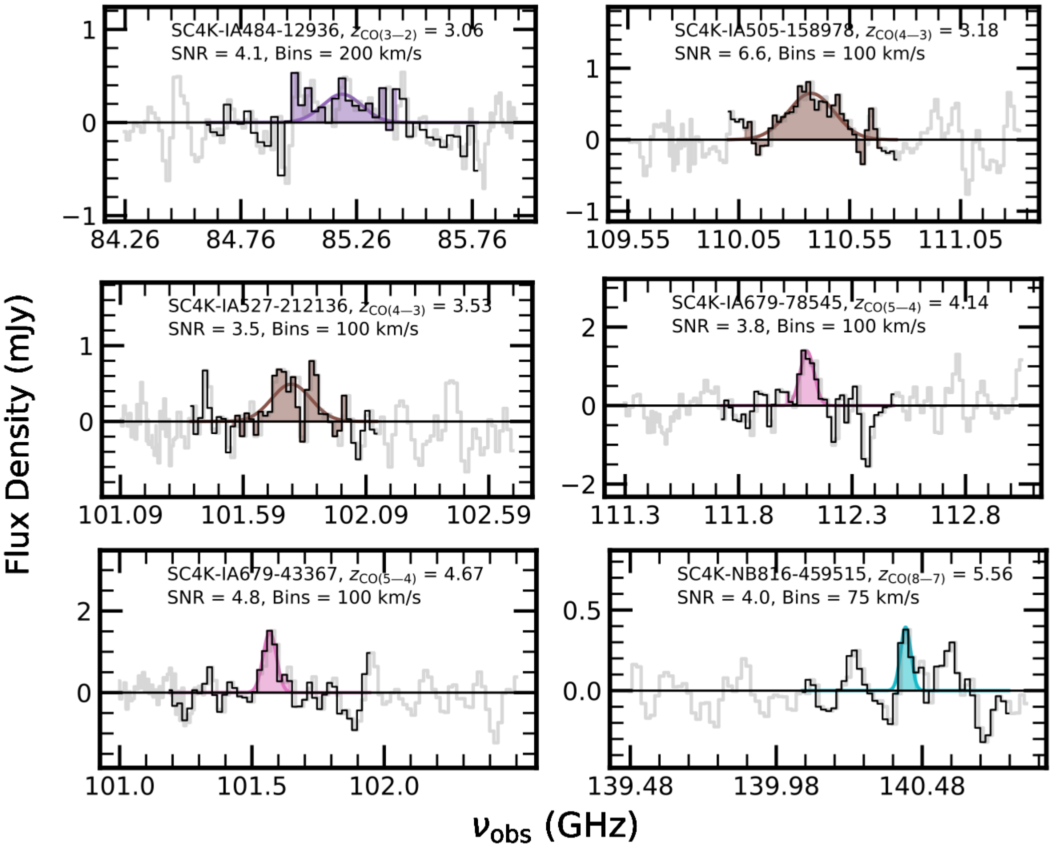

Continued from Figure 4.5. Potential CO(3–2), CO(4–3), CO(5–4), and CO(8–7) line detections. The CO(3–2) line in LAE SC4K-IA484-12936 shows a broad FWHM, which is unusual for low-mass galaxy like LAE. The CO(4–3) line in LAE SC4K-IA505-158978 also has a broad FWHM; since this LAE hosts an AGN, the broadening is likely influenced by AGN activity. LAEs SC4K-IA505-158978 and SC4K-NB816-459515 are detected in dust continuum emission with ALMA (Chapter 3).

properties using the same method as described above, but this time using the primary beam-corrected data cubes to ensure the accurate flux measurements. These 12 fitted lines are presented in Figure 4.5 and the corresponding measured properties are summarized in Table 4.2.

4.2.3.1 Final Sample

Out of 35 ALMA observed emission lines in 34 LAEs, we identify 12 line candidates with SNR>3.1 and a corresponding FDR of $\leq 50\%$ (Figure 4.5). These 12 potential line candidates were not observed as ALMA targets; they are serendipitous detections. For these candidates, we compare their emission-line-based redshifts with their photometric redshifts and corresponding uncertainties that are based on the FWHM of the filters used to detect Lyα emission in the SC4K survey. As shown in Figure 4.6, this redshift comparison allows us to assess the reliability of the lines. Moreover, we perform a visual inspection of each spectrum (Figure 4.5) to compare the noise level relative to the observed line.

Of the 12 SNR $>$ 3.1 lines (Table 4.2), we identify 6 detections (where SNR $\geq$ 3.5 and the line lies within the photometric redshift uncertainty), 2 tentative (where SNR $\geq$ 4 but the line lies outside the photometric redshift uncertainty) and 4 non-detections (where redshift of the observed line lies outside the photometric redshift uncertainty). Two of these 12 sources are detected in the continuum with ALMA (Chapter 3), but none are detected with *Herschel*/SCUBA2 (Chapter 2). The emission line in LAE SC4K-IA427-167426 lies near the edge of a noisy SPW and falls outside the expected frequency range based on photometric redshift uncertainties, so we classify it as a non-detection. Similarly, SC4K-IA427-79391, SC4K-IA679-78545, and SC4K-NB816-459515 have observed frequencies outside the predicted range and show noisy spectra when inspected, leading us to reject them as reliable detections. LAEs SC4K-IA427-40442 and SC4K-IA427-70144 have higher SNRs (≥ 4), corresponding to a lower FDR of 10%, but their observed frequencies also lie beyond the expected range, so we label them as tentative detections. Thus, after applying these checks, our final sample includes six confirmed and two tentative detections (see Table 4.2). For the remaining 27 non-detections with ALMA frequency coverage beyond the

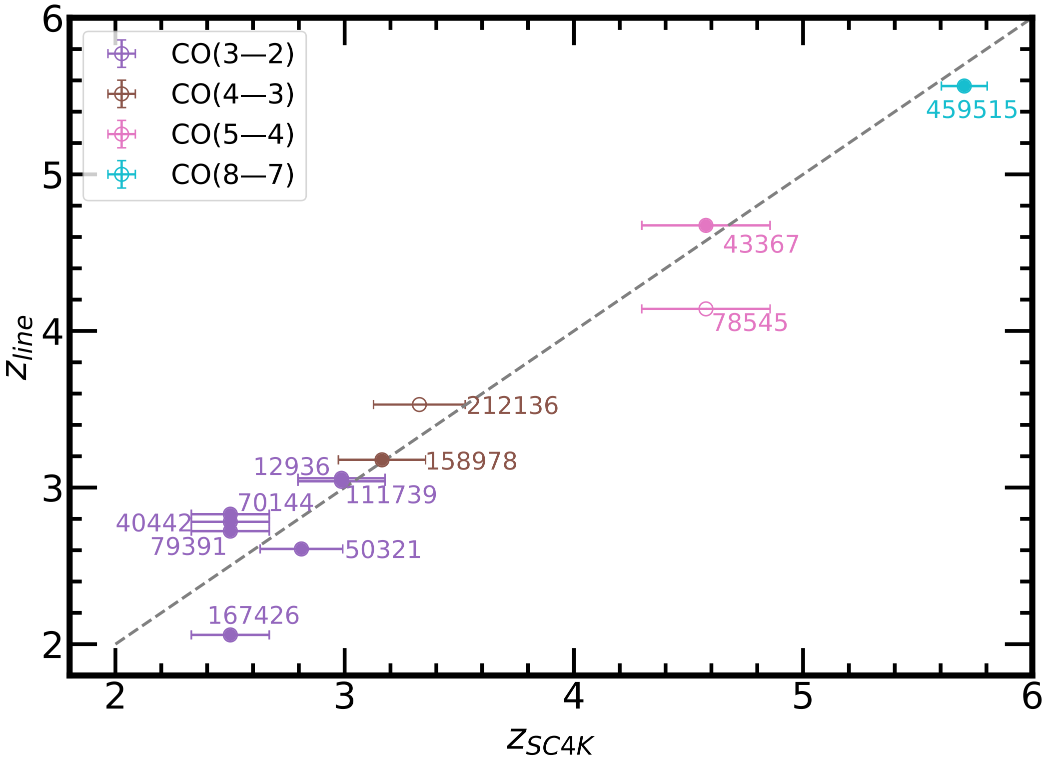

Figure 4.6: Comparison of potential far-infrared emission line redshift with SC4K photometric redshift and their uncertainties for LAEs with possible line detections. All line candidates have SNR > 3.1 and therefore FDR $\leq 50\%$. Filled circles represent higher-confidence detections (SNR ≥ 4 and FDR $\leq 10\%$), while unfilled circles indicate lower SNR < 4. True line should have uncertainties that cross the one-to-one line, corresponding to far-infrared lines having inferred redshifts that are consistent with the Lyα in the narrow or medium band SC4K filters (assuming no velocity offset in Lyα due to resonant scattering). LAEs SC4K-IA427-167426, SC4K-IA427-79391, SC4K-IA679-78545, and SC4K-NB816-459515 have possible lines that are significantly offset from their expected frequencies and further inspection suggests that these are false detections (Section 4.2.3.1). Similarly, SC4K-IA427-40442 and SC4K-IA427-70144 are determined to be only tentative line detections.

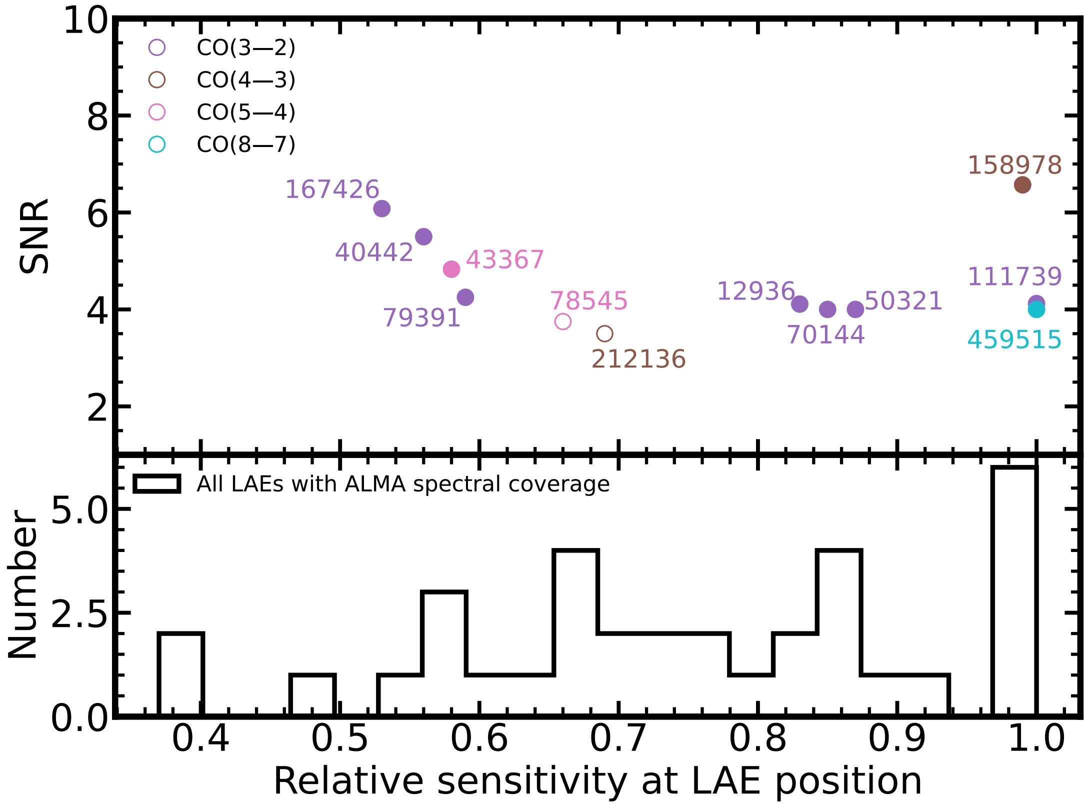

Figure 4.7: The distribution of the primary beam correction factor at the positions of LAEs in the ALMA observations (bottom) and compared to the SNR of the candidate lines (top). Filled circles show line candidates with SNR ≥ 4, while unfilled circles indicate lower SNR < 4 with FDR $\leq 50\%$. LAEs at the centre of an ALMA pointing have a relative sensitivity of 1, with lower values for sources further away from the pointing centre due to the primary beam. All detected lines lie in the $\geq$50% coverage region, likely due to the low sensitivity for sources further away from the pointing centres.

SC4K redshift uncertainty, we determine upper limits on the line flux at the expected observed frequency (based on photometric redshift), assuming a line FWHM of 250 km/s. This value is chosen based on the median FWHM of the 8 potential line candidates.

We also analyse the distribution of the primary beam correction factor in Figure 4.7. All 12 line candidates lie in regions where the primary beam correction factor is greater than 50%. Notably, 4 out of the 6 confirmed detections fall within regions where the primary beam correction is >80%, suggesting that detections are more likely when LAEs are located closer to the ALMA pointing center (high sensitivity). A primary beam correction of 100% (i.e., a factor of 1) corresponds to the centre of the ALMA field of view, where sensitivity is highest and approximately the location of the original observation target.

4.3 Results and Analysis

4.3.1 Constraining molecular gas mass in LAEs

We next, investigate the molecular gas content of LAEs using the ALMA observations of [C I] 609 and various CO lines.

4.3.1.1 CO lines

There are a total of 33 observations of CO line in LAEs (Table 4.1). These observations cover multiple CO transitions, namely CO(3–2), CO(4–3), CO(5–4), CO(6–5), and CO(8–7). Among these, we detect six CO emission lines with high confidence and identify two additional tentative detections (Section 4.2.3.1). All confirmed and tentative detections are found in the mid-J transitions—CO(3–2), CO(4–3), and CO(5–4). To derive the CO line luminosities, we follow the methodology presented by Solomon et al. (1992), using the equation:

$$L'_{\rm line} = 3.25 \times 10^{7} \, \frac{S_{\rm line} \, \Delta v \, D_L^2}{(1+z)^3 \, \nu_{\rm obs}^2} \quad [\mathrm{K\,km\,s^{-1}\,pc^2}] \tag{4.1}$$

where $S_{\rm line}\,\Delta v$ is the integrated line flux in $\rm Jy\,km\,s^{-1}$, D_L is the luminosity distance in Mpc, z is the redshift of the source, and $\nu_{\rm obs}$ is the observed frequency of the CO line in GHz. We derive $L'_{\rm line}$, as well as upper limits in cases of non-detections, using Equation 4.1, based on the measured integrated line fluxes, luminosity distances, and observed frequencies for each LAE. The resulting line luminosities are listed in Table 4.3.

In Figure 4.8, we compare our derived $L'_{\rm line}$ values with results from previous studies of star-forming galaxies at similar redshifts. We include comparisons with the upper limits on CO(2–1) emission in a Lyman-break galaxy (LBG) at $z \sim 5$ from Davies et al. (2010), and with the CO(3–2) detection in a LBG at $z \sim 3$ by Magdis et al. (2017). Our measurements and upper limits are consistent with the constraints from Davies et al. (2010), but lie below the CO(3–2) detection by Magdis et al. (2017). A possible explanation for this discrepancy is the significantly higher stellar mass of the LBG studied by Magdis et al. (2017), which has $\log_{10}(M_\star/{\rm M}_\odot) = 11.28$, compared to the median stellar mass of our LAE sample of $\log_{10}(M_\star/{\rm M}_\odot) = 9.5$. This suggests that the higher CO line luminosity observed in the LBG may be attributed to its greater stellar mass and overall gas content, consistent with expectations for more massive star-forming galaxies. We also compare our results with those of various CO and [C I] 609 lines in submillimeter galaxies (SMGs) at $z \sim 3$–5 and CO lines in star-forming galaxies (SFGs) at $z = 2$–2.7, studied by Birkin et al. (2021) and Boogaard et al. (2020), respectively. LAEs have $L'_{\rm line}$ values that are similar to these populations.

Since we primarily observe mid-J CO lines, we require $L'_{\rm CO(1-0)}$ in order to estimate the total molecular gas mass in LAEs. There are no studies of the CO spectral line energy distribution (SLED) in LAEs, so we convert $L'_{\rm CO(n\rightarrow n-1)}$ (presented in Table 4.3) to the ground-state transition $L'_{\rm CO(1-0)}$ using CO line ratios from Boogaard et al. (2020), which are based on a two-component large velocity gradient (LVG) model calibrated for star-forming galaxies at $z = 2$–2.7. Although the Boogaard et al. (2020) sample has a higher median stellar mass ($\log(M_\star/M_\odot) \sim 10.82$) compared to our ALMA-observed LAEs ($\log(M_\star/M_\odot) \sim 9.5$), both populations are star-forming galaxies at comparable redshifts. Whilst the excitation conditions in our lower-mass LAEs may differ from those in the more massive Boogaard et al. (2020) sample, the LVG-based line ratios adopted

Table 4.3: Physical properties of LAEs based on their potential emission line detections. Non-detections are shown in italics, and we provide 1σ upper limits on their physical properties.

SC4K ID	Line	L'_{CO}[k]	$M_{\mathrm{H_2}}$[l]	$f_{\mathrm{H_2}}$[m]
		($10^{10}\,\mathrm{K\,km\,s^{-1}\,pc^2}$)	($10^{10}\,M_\odot$)	
SC4K-IA427-167426	*CO(3–2)*	*< 0.19*	*< 0.95*	*< 0.54*
SC4K-IA427-79391	*CO(3–2)*	*< 0.13*	*< 0.65*	*< 0.86*
SC4K-IA464-50321	CO(3–2)	0.73±0.19	3.72±1.20	0.95±0.03
SC4K-IA427-40442	CO(3–2)	0.90±0.18	4.59±1.27	0.92±0.03
SC4K-IA427-70144	CO(3–2)	0.65±0.19	3.33±1.14	0.91±0.03
SC4K-IA484-111739	CO(3–2)	1.53±0.36	7.86±2.35	0.58±0.09
SC4K-IA484-12936	CO(3–2)	1.74±0.43	8.91±2.80	0.99±0.01
SC4K-IA505-158978[n]	CO(4–3)	1.30±0.21	8.72±2.43	0.25±0.07
SC4K-IA527-212136	CO(4–3)	0.94±0.25	6.32±2.22	0.92±0.04
SC4K-IA679-78545	*CO(5–4)*	*< 0.21*	*< 1.93*	*< 0.88*
SC4K-IA679-43367	CO(5–4)	0.99±0.19	9.18±3.00	0.98±0.01
SC4K-NB816-459515[n]	*CO(8–7)*	*< 0.04*	*< 1.71*	*< 0.66*

[k] Line luminosity L'_{CO} for the $J = n \rightarrow n-1$ rotational transition, derived using the method from Solomon et al. 1992 (Section 4.3.1.1).

[l] Molecular gas mass derived from the CO line luminosity, assuming $\alpha_{\mathrm{CO}} = 4.1 \pm 0.4\,\mathrm{M_\odot}\,(\mathrm{K\,km\,s^{-1}\,pc^2})^{-1}$ from Dunne et al. 2022 (Section 4.3.1.3).

[m] Molecular gas fraction, defined as $M_{\mathrm{H_2}}/(M_{\mathrm{H_2}} + M_*)$.

[n] LAE also detected in dust continuum emission with ALMA (Chapter 3).

from their study are among the best available constraints for high-redshift star-forming galaxies which are similar to LAEs. We calculate the molecular gas masses (M_{H_2}) and upper limits for LAEs based on their $L'_{\mathrm{CO}(1-0)}$. To convert $L'_{\mathrm{CO}(1-0)}$ into M_{H_2}, we use the CO-to-H$_2$ conversion factor (α_{CO}) from Dunne et al. (2022) including a factor 1.36 to account for He. Dunne et al. (2022) calibrate α_{CO} using a sample of 407 galaxies, ranging from local discs to submillimetre-selected galaxies (SMGs) up to $z \approx 6$. They constrain α_{CO} to be 4.4 ± 0.1 for main sequence galaxies and 3.8 ± 0.1 for SMGs. Since this ratio is not yet constrained for LAEs, we adopt the average value $\alpha_{\mathrm{CO}} = 4.1$, with a systematic uncertainty of ± 0.3, to account for the spread between the two populations. Using the relation

$$M_{\mathrm{H}_2} = \alpha_{\mathrm{CO}} \times L'_{\mathrm{CO}(1-0)} \tag{4.2}$$

where M_{H_2} is in $M_\odot$, $L'_{\mathrm{CO}(1-0)}$ is in units of $\mathrm{K\,km\,s^{-1}\,pc^2}$, and α_{CO} is in $\mathrm{M_\odot\,(K\,km\,s^{-1}\,pc^2)^{-1}}$, we calculate the molecular gas masses presented in Table 4.3. All M_{H_2} values throughout this work include a systematic uncertainty of ± 0.3 in α_{CO}. We also estimate the molecular gas fractions in LAEs and corresponding upper limits. The gas fraction (f_{H_2}) is calculated using the derived molecular gas masses and stellar masses ($M_\star$) of LAEs from the SC4K survey, following the relation:

$$f_{\mathrm{H}_2} = \frac{M_{\mathrm{H}_2}}{M_{\mathrm{H}_2} + M_\star} \tag{4.3}$$

The resulting gas fractions are also presented in Table 4.3.

4.3.1.2 [C I] 609 line

In our sample, we have two [C I] 609 line (hereafter [C I]) observations for two LAEs. In both cases, the line is not detected, and we derive upper limits on $L'_{[\mathrm{C\,I}]}$ using Equation 4.1. These upper limits are shown in Figure 4.8 and are compared with the [C I] measurements in SMGs from Birkin et al. (2021). Our estimated $L'_{[\mathrm{C\,I}]}$ upper limits for the LAEs lie well below the values measured in SMGs from Birkin et al. (2021), suggesting that either the [C I] line is intrinsically weaker in LAEs, or that their molecular gas reservoirs are lower relative to the dust-rich,

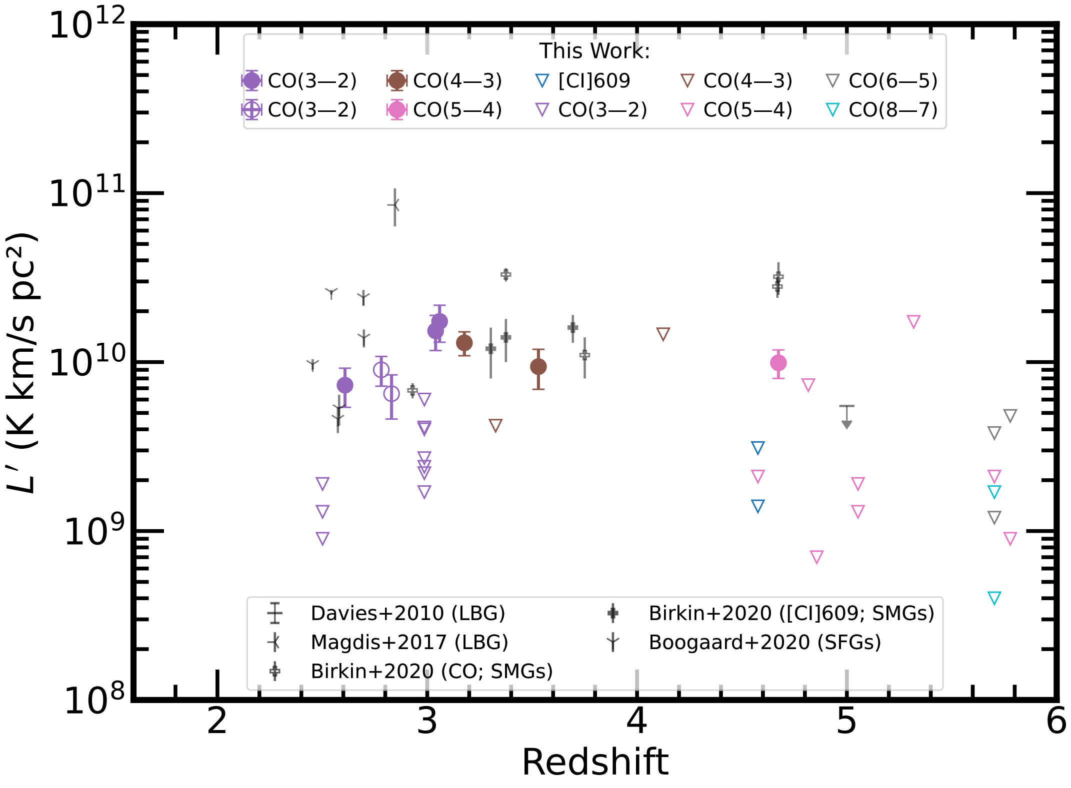

Figure 4.8: Line luminosity as a function of redshift for various CO and [C I] lines in LAEs and compared to other high redshift galaxy populations. Filled circles represent CO detections, unfilled circles denote tentative detections, and unfilled inverted triangles indicate upper limits. Results from other studies are shown in grey: Davies et al. (2010)—CO(2–1), with an upper limit for an LBG; Magdis et al. (2017)—CO(3–2), showing a massive LBG; SMGs from Birkin et al. (2021); and Boogaard et al. (2020)—SFGs observed in various CO lines. CO-detected LAEs at $z \sim$ 2–4 have line luminosities comparable to those of SFGs and SMGs. At higher redshifts, LAEs show fainter emission relative to SMGs, with upper limits consistent with those for CO(2–1) in a LBG from Davies et al. (2010). Overall, the upper limits suggest that LAEs are generally faint in various CO and [C I] lines.

massive SMGs. This is consistent with the expectations, given the lower stellar masses of LAEs. We estimate upper limits on the $M_{\mathrm{H_2}}$ from the $L'_{[\mathrm{C\,I}]}$ upper limits. The conversion is done using equation 4.4:

$$M_{\mathrm{H_2}} = \alpha_{[\mathrm{C\,I}]} \times L'_{[\mathrm{C\,I}]} \tag{4.4}$$

where $M_{\mathrm{H_2}}$ is in $\mathrm{M_\odot}$, $L'_{[\mathrm{C\,I}]}$ is in $\mathrm{K\,km\,s^{-1}\,pc^2}$, and $\alpha_{[\mathrm{C\,I}]}$ is in $\mathrm{M_\odot\,(K\,km\,s^{-1}\,pc^2)^{-1}}$. We adopt the $\alpha_{[\mathrm{C\,I}]}$ value estimated by Dunne et al. (2022). They find $\alpha_{[\mathrm{C\,I}]} = 19.1 \pm 0.6$ for main sequence galaxies and 16.2 ± 0.4 for SMGs. Since $\alpha_{[\mathrm{C\,I}]}$ is not available for LAEs, we use the average value $\alpha_{[\mathrm{C\,I}]} = 17.65$, which includes a factor of 1.36 to account for He. We also include a systematic uncertainty of ± 1.45 in $\alpha_{[\mathrm{C\,I}]}$, which shows the range between the main sequence galaxies and SMG calibrations. This uncertainty is also propagated consistently in all uses of these values throughout the chapter (e.g., Figure 4.9 and 4.10). Using the $M_{\mathrm{H_2}}$ limits estimated from the [C I] line, we also derive upper limits on the $f_{\mathrm{H_2}}$, following Equation 4.3. These values provide constraints on the gas content of LAEs based on atomic carbon.

4.3.1.3 Molecular gas in LAEs

The molecular gas masses and upper limits for LAEs as a function of redshift are presented in Figure 4.9 and are typically $\sim(7\pm2)\times10^{10}\ M_\odot$. Our values are broadly consistent with those found in SFGs from Boogaard et al. (2020) and Wang et al. (2022), while generally lower than those estimated by Scoville et al. (2023) for star-forming galaxies and slightly higher than the starburst galaxies studied by Dessauges-Zavadsky et al. (2025). Wang et al. (2022) use the dust continuum to estimate gas masses in normal SFGs at $z = 0.4$–3.6 with stellar masses above $10^{10}\ M_\odot$. This is more massive than our LAEs (which have a median stellar mass of $\sim 10^{9.5}\ M_\odot$). Despite their different method and stellar mass range, their $M_{\mathrm{H_2}}$ values are similar to the values we find for LAEs. Scoville et al. (2023) also investigate massive SFGs ($10^{10}\ M_\odot$) and also derive molecular gas masses from dust continuum observations but their $M_{\mathrm{H_2}}$ values are systematically higher than the results from Wang et al. (2022), which may be due to different sample selection or survey limits. The starburst galaxy sample from Dessauges-Zavadsky et al. (2025) includes extremely UV-bright galaxies with stellar masses comparable to our LAEs ($\sim 10^9\,M_\odot$), making them more directly comparable to our sample. Dessauges-Zavadsky et al. (2025) use CO line observations and convert the CO line luminosities to $L'_{\rm CO(1-0)}$ utilising line ratios from Boogaard et al. (2020) as we did (Section 4.3.1.1). However, Boogaard et al. (2020) use an CO-to-H_2 conversion factor of $\alpha_{\rm CO} = 1$, for their sample of starburst galaxies, while, we use $\alpha_{\rm CO} = 4.1$, based on the more recent study by Dunne et al. (2022). This difference in $\alpha_{\rm CO}$ leads to $M_{\rm H_2}$ that are a factor of 4.1 lower than we would calculate for the same data. Indeed Dessauges-Zavadsky et al. (2025) find lower $M_{\rm H_2}$ for UV bright galaxies than our LAEs but if we use the same $\alpha_{\rm CO}$ in both works, the $M_{\rm H_2}$ would be similar, indicating that the apparent offset is mainly driven by the choice of $\alpha_{\rm CO}$.

The main uncertainty in our results is from the assumption in the CO SLED and of $\alpha_{\rm CO}$ and $\alpha_{\rm [C\,I]}$, which are not yet directly constrained for LAEs. This highlights the need for the future observations of multiple CO and [C I] transitions in LAEs to directly investigate their excitation conditions, estimate CO line ratios, and refine the conversion factors $\alpha_{\rm CO}$ and $\alpha_{\rm CI}$. These efforts are essential to reduce systematic uncertainties and improve the accuracy of molecular gas mass estimates in these young, star-forming, low-mass galaxies.

4.3.2 Evolution of molecular gas in LAEs

We next investigate the relationship between the molecular gas content in LAEs and their Lyα luminosity (Figure 4.10), redshift (Figure 4.9) and stellar mass (Figure 4.12). Our results, including detections (both confirmed and tentative) and upper limits cover a wide range of molecular gas masses ($\sim 5 \times 10^9$ to $10^{11}\,M_\odot$). Furthermore, all detections and tentative detections correspond to molecular gas masses above $10^{10}\,M_\odot$, while upper limits extend down to $\sim 5 \times 10^9\,M_\odot$. This difference highlights the sensitivity limits of current, mostly serendipitous ALMA observations. LAEs with detected molecular gas contain high gas content, while undetected LAEs may host even lower gas masses than probed by their upper limits. Deeper observations are needed to constrain both gas-rich and gas-poor

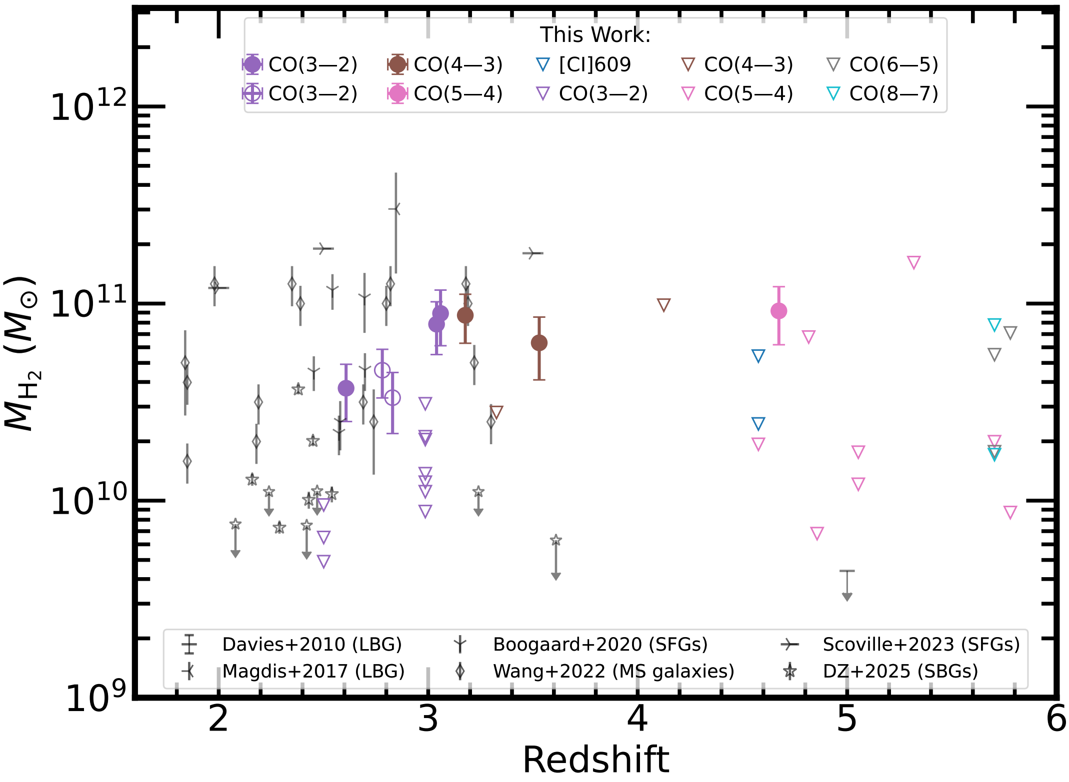

Figure 4.9: Derived molecular hydrogen mass (M_{H_2}) as a function of redshift for LAEs compared with other star-forming galaxies. M_{H_2} results from other studies are also shown including upper limit from Davies et al. (2010) for an LBG using CO(2–1); Magdis et al. (2017) CO(3–2) detection of a massive LBG, SMGs from Birkin et al. (2021) and SFGs from Boogaard et al. (2020) main sequence galaxies from Wang et al. (2013), SFGs from Scoville et al. (2023), and extremely UV-bright starburst galaxies from Dessauges-Zavadsky et al. 2025 (abbreviated as DZ in the plot) are displayed. Dessauges-Zavadsky et al. (2025) use the same method to estimate M_{H_2}, and their sample has a similar stellar mass to ours. However, they use a different CO-to-H$_2$ conversion factor ($\alpha_{\mathrm{CO}} = 1$) compared to our value of 4.1 based on the more recent study from Dunne et al. (2022). CO-detected LAEs at $z \sim 2$–4 have M_{H_2} comparable to those of SFGs and main sequence galaxies. At higher redshifts, M_{H_2} in LAEs are likely to be lower as indicated by upper limits consistent with a LBG from Davies et al. (2010). Our results suggest that LAEs have significant amounts of M_{H_2} as expected.

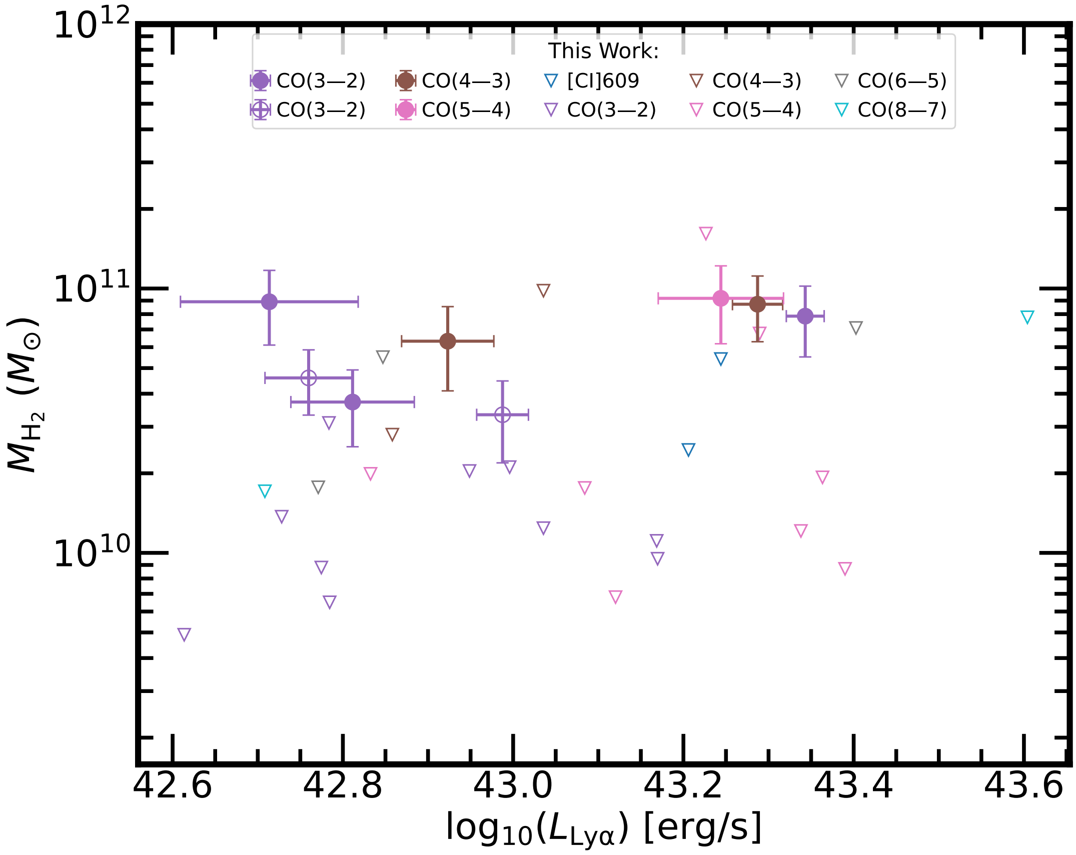

Figure 4.10: Molecular gas mass of LAEs as a function of their Lyα luminosity. Filled circles represent confirmed detections, unfilled circles indicate tentative detections, and inverted unfilled triangles show 1σ upper limits. Detected LAEs indicate a nearly flat trend, with both Lyα bright and faint LAEs showing similar M_{H_2} values. Upper limits on M_{H_2} for non-detections support this trend, suggesting no strong dependence of M_{H_2} on Lyα luminosity.

LAEs. We find that the molecular gas mass remains broadly constant over the observed range of Lyα luminosity, $\log_{10}(L_{\mathrm{Ly}\alpha}/\mathrm{erg\ s}^{-1}) \sim 42.6$ to 43.6 (Figure 4.10). However, our observations do not cover the full range of the parent LAE sample, which covers a wider Lyα luminosity range of $\log_{10}(L_{\mathrm{Ly}\alpha}/\mathrm{erg\ s}^{-1}) \sim 42.06$ to 44.54. Thus, expanding the coverage in Lyα luminosity is required for a complete understanding of how gas content correlates with Lyα luminosity over the full LAE population.

We present the molecular gas fraction of LAEs (calculated using Equation 4.3) as a function of redshift (Figure 4.11) and stellar mass (Figure 4.12) and we compare to previous studies of LBGs and other star-forming galaxies. Our results show the gas fractions in LAEs ranging from 20% to 99%, with most values above 80%. However, LBG detection from Magdis et al. (2017) and the upper limit from Davies et al. (2010) show gas fractions of ∼60%, illustrating an offset. In spite of their lower stellar masses, our LAEs show on average higher gas fractions than star-forming galaxies in Boogaard et al. (2020), suggesting that LAEs are likely in a gas-rich phase of evolution. Our LAEs show higher gas fraction than the median trend from CO-based previous measurements compiled in Dessauges-Zavadsky et al. (2020) and their [C II] 158 based measurements of main-sequence galaxies with similar stellar masses ($\log_{10}(M_*/M_\odot) \sim 9.7$). Notably, our results align more closely with the findings of Dessauges-Zavadsky et al. (2025). They investigate extremely UV-bright starburst galaxies with similar stellar masses as ours. Although their study is also based on CO lines and uses similar line ratios to derive molecular gas masses, however they use α_{CO} conversion factor$=1$, compared to our value of 4.1 from the more recent study by Dunne et al. (2022). If we apply the same α_{CO}, our gas fraction measurements align more closely with their starburst galaxies.

In Figure 4.12 we also compare our gas fraction measurements with those from previous studies, including the same literature sources as in the redshift-based analysis, with the addition of dust-continuum based measurements from Scoville et al. (2023). At the lower stellar mass end, our measurements are consistently higher than the upper limits derived for LBG by Davies et al. (2010) and the [C II]-based estimates from Dessauges-Zavadsky et al. (2020). Our values are also slightly higher than those measured for UV-bright starburst galax-

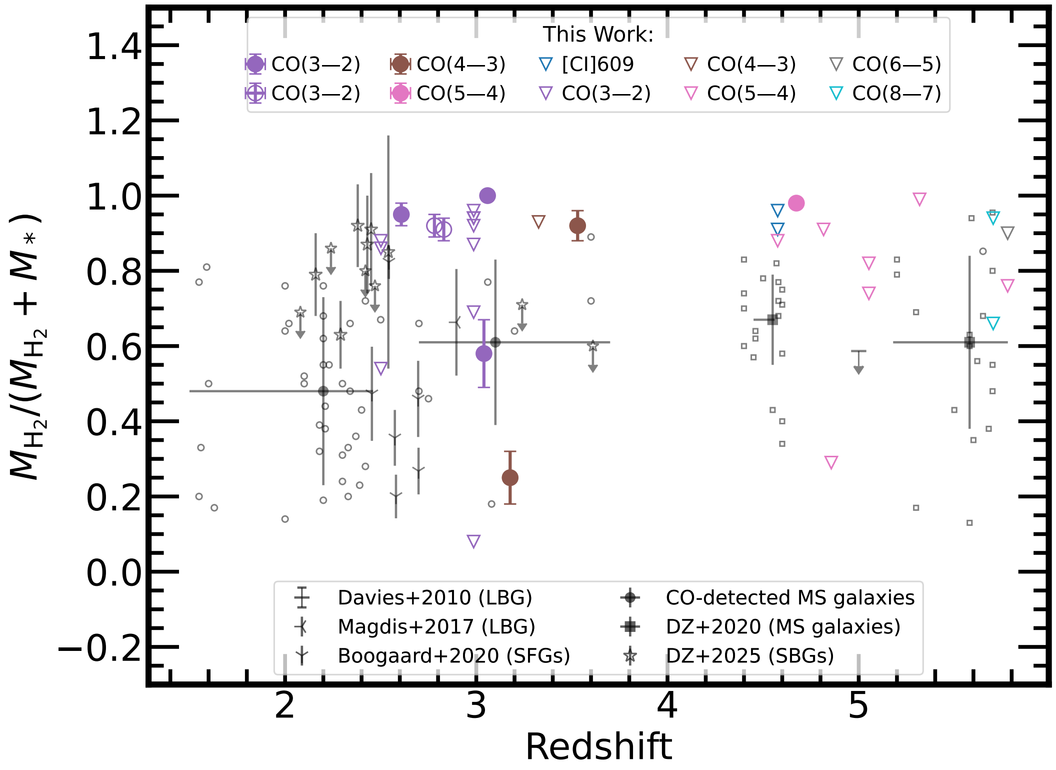

Figure 4.11: Molecular gas fraction of LAEs as a function of redshift. Filled circles represent detections, unfilled circles represent tentative detections, and unfilled inverted triangles show 1σ upper limits. LAEs show consistently high M_{H_2} fractions compared to typical star-forming galaxies at similar redshifts. At the lower-redshift end, their gas fractions are comparable to those of starburst galaxies, with some scatter, and are higher than the massive LBG from Magdis et al. (2017). At higher redshifts, LAEs maintain systematically elevated gas fractions relative to normal star-forming galaxies. Upper limits are also higher, though with scatter. These trends suggest that LAEs are likely gas-rich galaxies across cosmic time.

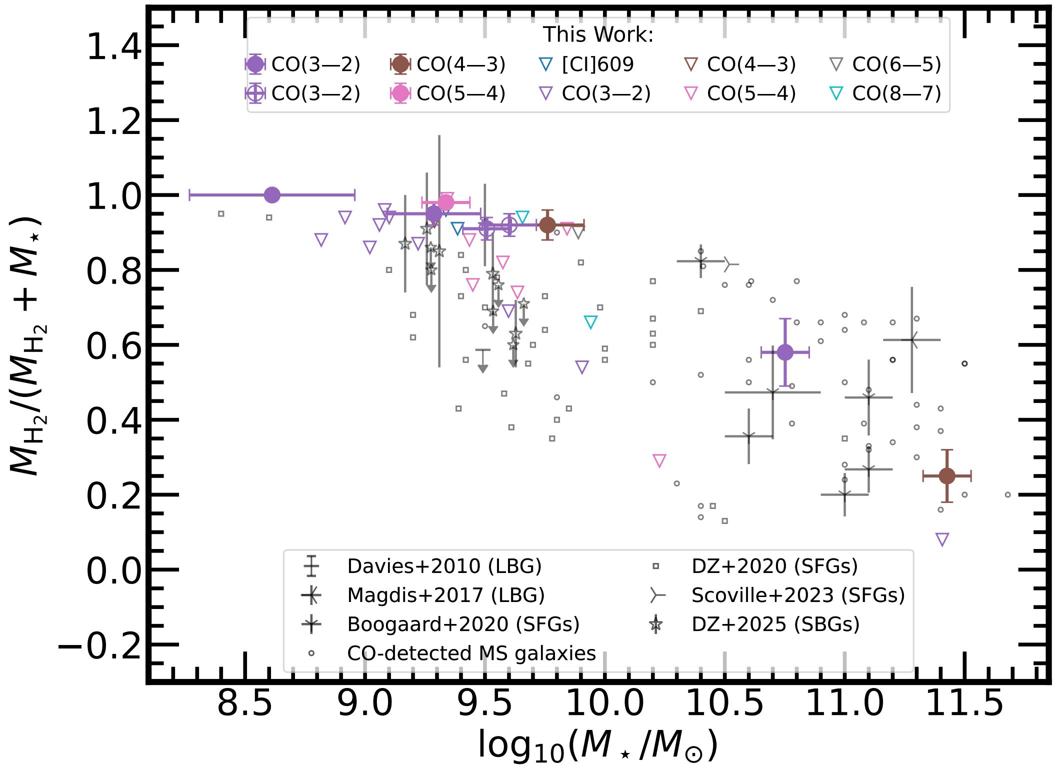

Figure 4.12: Molecular gas fraction of LAEs as a function of stellar mass. The LAE symbols and colour scheme follow the same convention as in Figure 4.11. LAEs show a declining gas fraction with increasing stellar mass, following a trend similar to star-forming galaxies. However, at the low-mass end, LAEs show significantly higher gas fractions exceeding even those of starburst galaxies, while at higher masses, their gas fractions converge with those of star-forming galaxies. This suggests that LAEs may evolve into typical star-forming galaxies as they grow.

ies by Dessauges-Zavadsky et al. (2025), who use the same CO line ratios but utilise a lower value of α_{CO}. At the higher stellar mass end, our molecular gas fractions are slightly lower than the values measured by Magdis et al. (2017) and Scoville et al. (2023), however they remain broadly consistent with those of Boogaard et al. (2020), the [C II]-based measurements of star-forming galaxies in Dessauges-Zavadsky et al. (2020), and the CO-detected main-sequence galaxies compiled by the same study. These results are consistent with the hypothesis that LAEs are young star-forming galaxies. As their stellar mass increases and gas is consumed, they likely evolve into more massive main-sequence galaxies seen at lower redshifts. However, our conclusions have limitations: the CO line ratios adopted from Boogaard et al. (2020), are based on more massive galaxies, not LAEs and key parameters like α_{CO} and α_{CI} are not yet empirically constrained for LAEs. Future work focusing on obtaining deeper, multi-transition CO and [C I] observations targeting LAEs covering a wide mass and redshift range are needed. Such observations would be crucial to directly constrain excitation conditions and conversion factors, refining estimates of molecular gas and enhancing our understanding of star formation in the early Universe.

In summary, LAEs are likely to be highly gas-rich systems, with molecular gas fractions which remain roughly constant between $z = 2$ to $z = 6$, and values more consistent with starburst galaxies than with typical star-forming galaxies.

4.4 Conclusions

We have measured the molecular gas content in LAEs using archival ALMA observations of CO and [C I] emission lines. In this analysis, we started with a parent sample of ∼4000 LAEs in the COSMOS field covering a redshift range of $z = 2$–6. The key findings and conclusions of our analysis are as follows:

1. We identified 349 LAEs with spatial ALMA coverage, covering a total of 364 spectral lines within the ALMA archival data. However, only 35 observations have spectral tunings corresponding to emission lines at the LAE redshifts. 33 CO and two [C I] lines were observed in 34 LAEs leading to 12 potential line candidates with SNR > 3.1 and FDR below 50%. Of these

six CO lines were detected along with two additional tentative detections, corresponding to CO(3–2), CO(4–3), and CO(5–4) transitions.

2. The detections have median line luminosities of $(0.96 \pm 0.36) \times 10^{10}$ ($\mathrm{K\,km\,s^{-1}\,pc^{2}}$). Non-detections L'_{line} 1σ upper limits cover a range $(0.04-16) \times 10^{10}$ ($\mathrm{K\,km\,s^{-1}\,pc^{2}}$), suggesting the need for deeper, targeted observations to probe fainter emission lines in LAEs.

3. We measured the molecular gas mass for our detected and tentatively detected sources which have a median value of $(7 \pm 2) \times 10^{10}\,M_{\odot}$, while for non-detected sources, the 1σ upper limits range from $\sim 5 \times 10^{9}$ to $\sim 2 \times 10^{11}$ $M_{\odot}$. The molecular gas fraction for the detections and tentative detections have a median of 0.92 ± 0.25. For the non-detections, the upper limits cover a broader range, from 0.04 to 0.99.

4. LAEs appear to host molecular masses comparable to other star-forming galaxies at similar redshifts. Their gas masses remains broadly constant between $z = 2$–6 and within the Lyα luminosity range of our sample. Our findings also suggest that gas fraction in LAEs decreases with increasing stellar mass, though deeper data on low mass LAEs are required to confirm this apparent trend. This trend suggests that LAEs are likely to evolve into typical star-forming systems as they grow in stellar mass.

5. Deeper data and future observations constraining the CO SLED, α_{CO} and α_{CI} in LAEs are required to further constrain the molecular gas content in LAEs.

Chapter 5

Conclusions

In this thesis, we utilized a sample of $\sim$4000 LAEs at $z = 2.2$–6 from the SC4K survey within the COSMOS field to investigate the presence and properties of dust and gas in these galaxies. We analysed the dust properties by combining far-infrared data from *Herschel* (PEP and SPIRE) and JCMT (S2COSMOS) single-dish observations (Chapter 2). To probe deeper, we used ALMA data from the A^{3}COSMOS survey, which have smaller field of view but better sensitivity compared to single-dish observations (Chapter 3). We also constrained the molecular gas content in LAEs by examining archival ALMA data covering these sources (Chapter 4).

In Chapter 2, we examined the dust emission and far-infrared properties of 3,674 SC4K LAEs. We used publicly available *Herschel* PACS and SPIRE data at 100–500 μm (Lutz et al., 2011; Oliver et al., 2012; Shirley et al., 2021), along with SCUBA-2 850 μm observations from the S2COSMOS survey (Simpson et al., 2019). We identified five LAEs that were individually detected at 850 μm, all of which host radio and/or X-ray AGN and have high Lyα luminosities, suggesting that AGN may contribute to their Lyα, UV, and far-infrared emission. For the remaining LAEs, we performed stacking in bins of redshift, Lyα luminosity, stellar mass and AGN presence, detecting average dust emission from the stacks of all AGN, X-ray and radio AGN, and the most massive LAEs ($\mathrm{M}_* = 10^{10-12}\,M_\odot$). Importantly, even when excluding AGN, the stack of massive LAEs still showed detectable dust emission, indicating that dust emission is driven by both stellar mass and AGN activity. We also examined IRX–β_{UV} relations and estimated the $f_{\mathrm{esc}}(\mathrm{Ly}\alpha)$, finding values of 1–7% for the individually detected sources and $f_{\mathrm{esc}}(\mathrm{Ly}\alpha) = 4$–5% for the detected stacks, consistent with previous studies and the global evolution of $f_{\mathrm{esc}}(\mathrm{Ly}\alpha)$. For undetected stacks, such as the stack of the entire LAE population, the inferred $f_{\mathrm{esc}}(\mathrm{Ly}\alpha)$ was strongly dependent on the assumed SED shape; Sd-like templates yielded high limits ($f_{\mathrm{esc}}(\mathrm{Ly}\alpha) \geq 33\%$ at 3σ), while M82-like templates gave values more consistent with global trends (e.g. Hayes et al., 2011), suggesting LAEs may host warmer dust than local Sd galaxies. The detected LAEs and stacks also showed redder UV slopes (β_{UV}) and higher IRX values than undetected ones, with trends broadly consistent with the Calzetti et al. (2000) dust law. These results indicate that LAEs likely feature clumpy or inhomogeneous dust distributions.

Building upon the single-dish measurements in Chapter 2, Chapter 3 focussed on the far-infrared properties of SC4K LAEs using deeper archival ALMA data from the A^{3}COSMOS survey. We examined 627 ALMA observations covering 375 LAEs, including 119 AGN, and identified 15 robust detections (SNR ≥ 4.35) of dust continuum emission. These detections predominantly fell within the high-sensitivity regions of the ALMA primary beam and were mostly observed in Bands 6 and 7, corresponding to rest-frame wavelengths of 300–700 μm, consistent with the expected peak of dust emission for LAEs in this redshift range. We modelled the far-infrared SEDs of these LAEs using a modified blackbody with parameters $\alpha = 2$, $\beta_{\mathrm{dust}} = 1.96$, and $T_{\mathrm{dust}} = 40\,\mathrm{K}$ to estimate the far-infrared luminosity (L_{IR}) and derive corresponding infrared-based star-formation rates ($\mathrm{SFR}_{\mathrm{IR}}$). The detected LAEs, including 12 hosting AGN, showed L_{IR} values of $10^{11.1}$–$10^{12.6}\,L_{\odot}$ and $\mathrm{SFR}_{\mathrm{IR}}$ ranging from 12 to 456 $M_{\odot}\,\mathrm{yr}^{-1}$. We estimated the $f_{\mathrm{esc}}(\mathrm{Ly}\alpha)$, for both detected and non-detected sources. These estimates ranged from 2 to 54% and were consistent with previous studies using both similar and alternative methods. However, significant uncertainties remain due to limited ALMA photometric coverage, which limits constraints on the far-infrared SED shape. We also derived IRX values (0.6 to 65) and examined their relation to β_{UV}, finding consistency with a range of dust attenuation curves, including the Calzetti et al. (2000), Meurer et al. (1999), and SMC-like laws (Gordon et al., 2003), reflecting the diversity in metallicity and stellar populations among LAEs. Our results agreed with earlier findings from Kusakabe et al. (2015) and Chapter 2. We also investigated the SFR–M_* relation for dust-detected LAEs aligned with the main sequence of star-forming galaxies at similar redshifts. However, the $\mathrm{SFR_{IR}}$–M_* relation appeared steeper than the $\mathrm{SFR_{Ly\alpha}}$–M_* relation, mainly for massive LAEs, highlighting the importance of dust-obscured star formation that would be missed in UV-only studies. This suggests that Lyα-based SFR estimates may underestimate true star-formation by up to ∼2 dex in some cases. We also found a tentative correlation between $f_{\mathrm{esc}}(\mathrm{Ly}\alpha)$ and stellar mass, supporting the idea that dust in LAEs is patchily distributed.

In Chapter 4, we investigated the molecular gas content of SC4K LAEs using archival ALMA observations of CO and [C I] emission lines. We identified 349 LAEs with spatial ALMA coverage. Among these, only 35 observations have spectral coverage for LAEs, resulting in 33 CO and two [C I] lines in 34 LAEs. From this subset, we identified 12 potential line candidates with SNR>3.1 and false detection rates below 50%, including six confirmed CO detections and two tentative ones corresponding to CO(3–2), CO(4–3), and CO(5–4) transitions. These detections have median line luminosities of $(0.96 \pm 0.36) \times 10^{10}\,\mathrm{K\,km\,s^{-1}\,pc^2}$, while non-detections cover a broader upper limit range of $(0.04 - 16) \times 10^{10}\,\mathrm{K\,km\,s^{-1}\,pc^2}$, highlighting the need for deeper, targeted observations to uncover fainter emission in the LAE population. We estimated molecular gas masses with a median of $(7 \pm 2) \times 10^{10}\,M_\odot$ for detections and tentative detections. For non-detections, upper limits on molecular gas masses range from $\sim 5 \times 10^9$ to $\sim 2 \times 10^{11}\,M_\odot$. The molecular gas fractions for detected sources have a median of 0.92 ± 0.25, whereas upper limits for the undetected sample cover a wider range from 0.04 to 0.99. These results suggest that LAEs have substantial gas reservoirs, comparable to other star-forming galaxies at similar redshifts. We also found that molecular gas masses appear to remain constant across redshifts $z = 2$–6 and within the Lyα luminosity range of our sample. However, we observed a decline in gas fraction with increasing stellar mass, suggesting that LAEs may evolve into typical star-forming galaxies as they grow. Confirming this trend requires deeper observations, particularly for low-mass LAEs. Furthermore, high-sensitivity observations are required to constrain the CO SLED, as well as the CO-to-$\mathrm{H_2}$ (α_{CO})

and CI-to-H$_2$ (α_{CI}) conversion factors, to robustly characterise the molecular gas content of LAEs across cosmic time.

5.1 Future Work

As discussed throughout this thesis, LAEs are generally young and low-mass galaxies, and they are expected to contain relatively small amounts of dust. This makes detecting their far-infrared emissions such as dust continuum and far-infrared lines challenging. Consequently, various far-infrared properties of LAEs still remain poorly constrained and require further investigation. Current far-infrared studies of LAEs rely on assumptions about dust temperature, SED shape, gas excitation, and attenuation laws. These assumptions introduce significant systematic uncertainties. To address these limitations, current and upcoming observational facilities will play an important role. High-resolution and deeper follow-up observations with the ALMA and deep single-dish surveys from upcoming instruments such as the Atacama Large Aperture Submillimeter Telescope (AtLAST; Klaassen et al., 2020; Ramasawmy et al., 2022), can enhance our sensitivity to faint far-infrared emissions from LAEs.

5.1.1 Dust continuum SEDs in LAEs

Our dust detections, discussed in Chapters 2 and 3 suggest bias towards the most massive and AGN host LAEs, limiting our understanding of dust in typical or low-mass LAEs. It appears likely that dust in LAEs is mainly linked to AGN activity and stellar mass, but deeper observations are required to probe the low mass end. Programs like the SCUBA-2 Ultra Deep Imaging EAO Survey (STUDIES; Gao et al. 2024) are beginning to probe deeper at ∼450 μm, but are still too shallow for individual detections. Stacking analysis of such single-dish far-infrared data can statistically estimate dust content in faint LAEs, however confusion noise remains a significant limitation. By increasing sample sizes and pushing to lower mass limits, these observations will refine the individual and average dust content estimates and its dependence on mass and the presence of

AGN. The proposed 50-m single-dish telescope AtLAST (Klaassen et al., 2020; Ramasawmy et al., 2022) would be a major step forward for addressing these limitations. With its large dish, AtLAST would offer better sensitivity and resolution than current single-dish telescopes like the JCMT and it is planned to offer simultaneous multiwavelength photometry. It is expected to provide an angular resolution of $\sim 1.8''$ at 450 μm and will cover a large field of view of about 2 square degrees. This means it would be able to observe larger areas of the sky and detect faint LAEs at multiple wavelengths to measure the far-infrared SED shape. Its resolution would also help reduce confusion noise. Thus, AtLAST would be able to detect dust continuum in LAEs that are too faint for current telescopes. It would also complement ALMA data by covering significantly wider areas (hence more LAEs) than interferometric observations. This would lead to more accurate estimates of obscured star formation rates and help us understand the complete picture of galaxy evolution in the early Universe.

ALMA provides a relatively small field of view but unmatched sensitivity and resolution for observing dust continuum emission in distant galaxies, including LAEs. Its archival data, mainly at longer wavelengths (e.g., Bands 6 and 7), already include valuable observations of LAEs, as discussed in Chapters 3 and 4. These observations trace the Rayleigh–Jeans side of the dust SED, but there is a lack of the shorter-wavelength data required to fully constrain dust temperatures and the SED peak. By combining these longer-wavelength measurements with follow-up observations at shorter wavelengths (e.g., Bands 8 and 9), we can refine the shape of the SED even before facilities like AtLAST are available. These Bands probe closer to the rest-frame far-infrared peak ($\sim$100μm) of dust emission for galaxies at $z \sim 2$– 6 (e.g., Casey, 2012; Oteo et al., 2012; Ward et al., 2024). Thus, these observations would allow for tighter constraints on dust temperature and SED shape, which are crucial for accurately estimating the total infrared luminosity ($L_{\rm IR}$). More accurate $L_{\rm IR}$ measurements will allow for better estimates of the infrared excess (IRX) and help to refine the IRX–$\beta_{\rm UV}$ relation. Improving this relation is important for studies of distant LAEs (as discussed in Safarzadeh et al., 2017; Narayanan et al., 2018; Liang et al., 2021), where direct far-infrared measurements are often not available, and UV-based methods are the primary tools for estimating star formation rates. Therefore, combining ALMA's archival and follow-up multi-band data not only enhances our understanding of dust properties in LAEs but also improves our ability to infer total star formation activity from UV/optical observations alone.

5.1.2 Constraining $f_{\rm esc}$(Lyα) using radio continuum

Understanding the $f_{\rm esc}$(Lyα) is important for investigating the epoch of reionization and calculating the SFR in distant galaxies, as Lyα photons are sensitive to the ionization state of the ISM, CGM, and IGM. However direct measurement of $f_{\rm esc}$(Lyα) at $z > 6$ is complicated as the IGM contains a higher fraction of neutral hydrogen that blocks Lyα photons, while at $z < 6$, the IGM is mostly ionized, making it transparent for Lyα photons (Becker et al., 2001). This makes measurement of $f_{\rm esc}$(Lyα) easier. By constraining the $f_{\rm esc}$(Lyα) at these lower redshifts, we can use that knowledge to better understand Lyα observations at higher redshifts, where JWST is already providing unprecedented insights. An alternative method to dust continuum is to compare SFR$_{{\rm Ly}\alpha}$ with star formation rate estimated using radio continuum observation (e.g., Calhau et al., 2020). This method allows us to estimate the $f_{\rm esc}$(Lyα) by comparing the observed Lyα emission to the intrinsic SFR, as traced by radio continuum emission. Current radio telescopes such as GMRT and VLA are already capable of supporting these studies at intermediate redshifts, and future facilities like the Square Kilometre Array (SKA; Dewdney et al., 2009; Prandoni & Seymour, 2015) will improve sensitivity and redshift coverage. However, there is an important limitation to this method. Radio emissions can sometimes come from AGN instead of star formation, which can result in overestimation of the star formation rate (Delvecchio et al., 2017; Smolčić et al., 2017; Azadi et al., 2023). In spite of such challenges, the combined use of Lyα and new sensitive radio observations can provide an alternative way to estimate $f_{\rm esc}$(Lyα) from these galaxies.

5.1.3 Characterizing the ISM conditions in LAEs via spectral line energy distributions

Detailed studies of the CO spectral line energy distributions (SLEDs; Carilli & Walter, 2013; Hodge & da Cunha, 2020) in LAEs have not yet been conducted due to the previously expected faintness of the lines. We have now shown that it is possible to detect CO from LAEs, but we had to rely on assumptions about line ratios to estimate their molecular hydrogen (e.g. Chapter 4), which is the fuel for star formation. Focusing on LAEs at intermediate redshifts ($z \sim 2$–3) will provide a valuable opportunity to address this problem. By targeting these LAEs with ALMA, it becomes possible to observe multiple CO emission lines, which can help us to build the CO SLED. This will help us to understand the molecular gas content and excitation conditions in LAEs at these intermediate redshifts. This approach will provide an alternative to using UV/optical lines to probe the ISM properties of LAEs and offers valuable insights into their colder regions that have not been explored. Thus, targeting LAEs with the ALMA can help us to fill the gaps in our knowledge of galaxy evolution.

References

Abel T., Bryan G. L., Norman M. L., 2002, Science, 295, 93

Adscheid S., et al., 2024, A&A, 685, A1

Ahmadi A., Hacar A., 2023, ALminer: ALMA archive mining and visualization toolkit, Astrophysics Source Code Library, record ascl:2306.025

Álvarez-Márquez J., et al., 2016, A&A, 587, A122

Arshutkin L. N., 1980, Astrometriia i Astrofizika, 41, 29

Asano R. S., Takeuchi T. T., Hirashita H., Inoue A. K., 2013a, Earth, Planets and Space, 65, 213

Asano R. S., Takeuchi T. T., Hirashita H., Nozawa T., 2013b, MNRAS, 432, 637

Atek H., Kunth D., Hayes M., Östlin G., Mas-Hesse J. M., 2008, A&A, 488, 491

Atek H., et al., 2023, MNRAS, 519, 1201

Azadi M., et al., 2023, ApJ, 945, 145

Baker J. G., Menzel D. H., 1938, ApJ, 88, 52

Baldwin J. A., Phillips M. M., Terlevich R., 1981, PASP, 93, 5

Balog Z., et al., 2014, Experimental Astronomy, 37, 129

Barisic I., et al., 2017, ApJ, 845, 41

Baugh C. M., Cole S., Frenk C. S., 1996, MNRAS, 283, 1361

Becker R. H., et al., 2001, AJ, 122, 2850

Beeston R. A., Gomez H. L., Dunne L., Maddox S., Eales S. A., Smith M. W. L., 2024, MNRAS, 535, 3162

Benson A. J., Sugiyama N., Nusser A., Lacey C. G., 2006, MNRAS, 369, 1055

Biggs A. D., et al., 2011, MNRAS, 413, 2314

Birkin J. E., et al., 2021, MNRAS, 501, 3926

Blumenthal G. R., Faber S. M., Primack J. R., Rees M. J., 1984, Nature, 311, 517

Bolatto A. D., Wolfire M., Leroy A. K., 2013, ARA&A, 51, 207

Bollo V., et al., 2025, A&A, 695, A163

Boogaard L. A., et al., 2020, ApJ, 902, 109

Bothwell M. S., Kennicutt R. C., Lee J. C., 2009, MNRAS, 400, 154

Bourne N., Dunne L., Ivison R. J., Maddox S. J., Dickinson M., Frayer D. T., 2011, MNRAS, 410, 1155

Bouwens R. J., et al., 2016, ApJ, 833, 72

Bowler R. A. A., Bourne N., Dunlop J. S., McLure R. J., McLeod D. J., 2018, MNRAS, 481, 1631

Brandt W. N., Alexander D. M., 2015, AAPR, 23, 1

Brinchmann J., Charlot S., White S. D. M., Tremonti C., Kauffmann G., Heckman T., Brinkmann J., 2004, MNRAS, 351, 1151

Bromm V., 2004, PASP, 116, 103

Bromm V., Coppi P. S., Larson R. B., 2002, ApJ, 564, 23

Bruce V. A., et al., 2014, MNRAS, 444, 1001

Bunker A., Stanway E., Ellis R., Lacy M., McMahon R., Eyles L., Stark D., Chiu K., 2008. p. 73 (`arXiv:0909.1565`), doi:10.48550/arXiv.0909.1565

Bunker A. J., et al., 2023, A&A, 677, A88

Burke J. R., Hollenbach D. J., 1983, ApJ, 265, 223

Cain C., D'Aloisio A., Gangolli N., Becker G. D., 2021, ApJL, 917, L37

Calhau J., et al., 2020, MNRAS, 493, 3341

Calzetti D., Armus L., Bohlin R. C., Kinney A. L., Koornneef J., Storchi-Bergmann T., 2000, ApJ, 533, 682

Capak P., et al., 2007, ApJS, 172, 99

Capak P. L., et al., 2015, Nature, 522, 455

Carilli C. L., Walter F., 2013, ARA&A, 51, 105

Carniani S., et al., 2020, MNRAS, 499, 5136

Carniani S., et al., 2024, Nature, 633, 318

Carroll B. W., Ostlie D. A., 2017, An introduction to modern astrophysics, Second Edition

Casey C. M., 2012, MNRAS, 425, 3094

Casey C. M., Narayanan D., Cooray A., 2014a, Physics Reports, 541, 45

Casey C. M., et al., 2014b, ApJ, 796, 95

Castellano M., et al., 2022, ApJL, 938, L15

Chabrier G., 2003, PASP, 115, 763

Chandrasekhar S., 1931, ApJ, 74, 81

Chapman S. C., Blain A. W., Ivison R. J., Smail I. R., 2003, Nature, 422, 695

Clark P. C., Glover S. C. O., Klessen R. S., Bromm V., 2011, ApJ, 727, 110

Conley A., et al., 2011, ApJL, 732, L35

Coogan R. T., et al., 2019, MNRAS, 485, 2092

Cooke E. A., et al., 2018, ApJ, 861, 100

Cornish T., 2023, PhD thesis, Lancaster University, doi:10.17635/lancaster/thesis/2194

Cristello N., 2024, in American Astronomical Society Meeting Abstracts. p. 347.02

Cui Y., Xiang Y., Rong K., Feris R., Cao L., 2014,] 10.1109/WACV.2014.6836098, pp 213–219

Curtis-Lake E., et al., 2012, MNRAS, 422, 1425

Curtis-Lake E., et al., 2023, Nature Astronomy, 7, 622

DESI Collaboration et al., 2024, AJ, 168, 58

Daddi E., et al., 2007, ApJ, 670, 156

Davies L. J. M., Bremer M. N., Stanway E. R., Birkinshaw M., Lehnert M. D., 2010, MNRAS, 408, L31

Dawson S., et al., 2004, ApJ, 617, 707

Decarli R., et al., 2016, ApJ, 833, 69

Dekel A., et al., 2009, Nature, 457, 451

Delhaize J., et al., 2017, A&A, 602, A4

Delvecchio I., et al., 2017, A&A, 602, A3

Dessauges-Zavadsky M., et al., 2020, A&A, 643, A5

Dessauges-Zavadsky M., Marques-Chaves R., Schaerer D., Xiao M. Y., Colina L., Alvarez-Marquez J., Pérez-Fournon I., 2025, A&A, 693, A17

Dewdney P. E., Hall P. J., Schilizzi R. T., Lazio T. J. L. W., 2009, IEEE Proceedings, 97, 1482

Dijkstra M., Westra E., 2010, MNRAS, 401, 2343

Dijkstra M., Haiman Z., Spaans M., 2006, ApJ, 649, 14

Dijkstra M., Lidz A., Wyithe J. S. B., 2007, MNRAS, 377, 1175

Djorgovski S., Davis M., 1987, ApJ, 313, 59

Draine B. T., 2006, ApJ, 636, 1114

Draine B. T., 2011, Physics of the Interstellar and Intergalactic Medium

Draine B. T., Li A., 2007, ApJ, 657, 810

Drew P. M., Casey C. M., 2022, ApJ, 930, 142

Dunne L., Eales S., Ivison R., Morgan H., Edmunds M., 2003, Nature, 424, 285

Dunne L., Maddox S. J., Papadopoulos P. P., Ivison R. J., Gomez H. L., 2022, MNRAS, 517, 962

Duval F., Schaerer D., Östlin G., Laursen P., 2014, A&A, 562, A52

Dwek E., et al., 1997, ApJ, 475, 565

Eales S., et al., 2012, ApJ, 761, 168

Einasto M., Einasto J., 1987, MNRAS, 226, 543

Einstein A., 1916, Annalen der Physik, 354, 769

Eisenstein D. J., et al., 2005, ApJ, 633, 560

Elbaz D., et al., 2007, A&A, 468, 33

Erb D. K., Berg D. A., Auger M. W., Kaplan D. L., Brammer G., Pettini M., 2019, ApJ, 884, 7

Fabian A. C., 2012, ARA&A, 50, 455

Finkelstein S. L., Malhotra S., Rhoads J. E., Hathi N. P., Pirzkal N., 2009, MNRAS, 393, 1174

Fite W. L., Brackmann R. T., 1958, Physical Review, 112, 1151

Fite W. L., Stebbings R. F., Brackmann R. T., 1959, Physical Review, 116, 356

Frayer D. T., et al., 2009, AJ, 138, 1261

Friedmann A., 1922, Zeitschrift fur Physik, 10, 377

Frieman J., Turner M., Huterer D., 2008, Ann. Rev. Astron. Astrophys., 46, 385

Fudamoto Y., et al., 2020, MNRAS, 491, 4724

Fudamoto Y., et al., 2025, arXiv e-prints, p. arXiv:2504.03831

Gao Z.-K., et al., 2024, ApJ, 971, 117

Garn T., Best P. N., 2010, MNRAS, 409, 421

Garratt T. K., et al., 2021, ApJ, 912, 62

Genzel R., Eisenhauer F., Gillessen S., 2010, Reviews of Modern Physics, 82, 3121

Glover S. C. O., Clark P. C., 2012, MNRAS, 421, 9

Gobat R., Magdis G., D'Eugenio C., Valentino F., 2020, A&A, 644, L7

Gordon K. D., Clayton G. C., Misselt K. A., Landolt A. U., Wolff M. J., 2003, ApJ, 594, 279

Griffin M. J., et al., 2010, A&A, 518, L3

Gunn J. E., Peterson B. A., 1965, ApJ, 142, 1633

Gurung-López S., Orsi Á. A., Bonoli S., Padilla N., Lacey C. G., Baugh C. M., 2020, MNRAS, 491, 3266

Habouzit M., et al., 2021, MNRAS, 503, 1940

Haiman Z., Spaans M., 1999, ApJ, 518, 138

Hansen M., Oh S. P., 2006, MNRAS, 367, 979

Harikane Y., et al., 2018, ApJ, 859, 84

Harikane Y., et al., 2020, ApJ, 896, 93

Hasegawa K., Umemura M., Susa H., 2009, MNRAS, 395, 1280

Hasinger G., et al., 2018, ApJ, 858, 77

Hayes M., Schaerer D., Östlin G., Mas-Hesse J. M., Atek H., Kunth D., 2011, ApJ, 730, 8

Heger A., Woosley S. E., 2010, ApJ, 724, 341

Hester J. J., Desch S. J., 2005,] 10.48550/arXiv.astro-ph/0506190, 341, 107

Hinshaw G., et al., 2013, ApJS, 208, 19

Hirashita H., Ferrara A., Dayal P., Ouchi M., 2015, 499, 67

Hirashita H., Burgarella D., Bouwens R. J., 2017, MNRAS, 472, 4587

Hodge P., 1986, PASP, 98, 1095

Hodge J. A., da Cunha E., 2020, Royal Society Open Science, 7, 200556

Holland W. S., et al., 2013, MNRAS, 430, 2513

Hopkins A. M., Beacom J. F., 2006, ApJ, 651, 142

Hopkins P. F., Hernquist L., Cox T. J., Kereš D., 2008, ApJS, 175, 356

Hu W., et al., 2019, ApJ, 886, 90

Huang Y., Lee K.-S., Shi K., Malavasi N., Xue R., Dey A., 2021, ApJ, 921, 4

Hubble E. P., 1926, ApJ, 64, 321

Hubble E., 1929, pp 168–173, doi:10.1073/pnas.15.3.168

Hummer D. G., Storey P. J., 1987, MNRAS, 224, 801

Hunt L. K., et al., 2017, A&A, 606, A99

Inoue A. K., 2011, Earth, Planets and Space, 63, 1027

Ishibashi W., Fabian A. C., 2012, MNRAS, 427, 2998

Ivison R. J., et al., 2008, MNRAS, 390, 1117

Izotov Y. I., Thuan T. X., Guseva N. G., Schaerer D., Worseck G., Verhamme A., 2024, MNRAS, 527, 281

Jappsen A. K., Glover S. C. O., Klessen R. S., Mac Low M. M., 2007, ApJ, 660, 1332

Jeeson-Daniel A., Ciardi B., Maio U., Pierleoni M., Dijkstra M., Maselli A., 2012, MNRAS, 424, 2193

Jin S., et al., 2018, ApJ, 864, 56

Jog C. J., 2013, MNRAS, 434, L56

Jogee S., et al., 2009, ApJ, 697, 1971

Karakas A. I., Lattanzio J. C., 2014, PASA, 31, e030

Kauffmann G., et al., 2003, MNRAS, 346, 1055

Kemper F., 2013, Earth, Planets and Space, 65, 223

Kennicutt Jr. R. C., 1983, ApJ, 272, 54

Kennicutt Robert C. J., 1998a, ARA&A, 36, 189

Kennicutt Robert C. J., 1998b, ApJ, 498, 541

Kennicutt Jr. R. C., Tamblyn P., Congdon C. E., 1994, ApJ, 435, 22

Kewley L. J., Dopita M. A., 2002, ApJS, 142, 35

Kirkpatrick A., Pope A., Sajina A., Roebuck E., Yan L., Armus L., Díaz-Santos T., Stierwalt S., 2015, ApJ, 814, 9

Klaassen P. D., et al., 2020, in Marshall H. K., Spyromilio J., Usuda T., eds, Society of Photo-Optical Instrumentation Engineers (SPIE) Conference Series Vol. 11445, Ground-based and Airborne Telescopes VIII. p. 114452F (`arXiv:2011.07974`), doi:10.1117/12.2561315

Klessen R. S., Glover S. C. O., 2023, ARA&A, 61, 65

Kolupuri S., et al., 2025, A&A, 695, A201

Konno A., et al., 2014, ApJ, 797, 16

Konno A., Ouchi M., Nakajima K., Duval F., Kusakabe H., Ono Y., Shimasaku K., 2016, ApJ, 823, 20

Koprowski M. P., et al., 2018, MNRAS, 479, 4355

Kormendy J., Richstone D., 1995, ARA&A, 33, 581

Kormendy J., Fisher D. B., Cornell M. E., Bender R., 2009, ApJS, 182, 216

Kroupa P., 2001, MNRAS, 322, 231

Kusakabe H., Shimasaku K., Nakajima K., Ouchi M., 2015, ApJL, 800, L29

Laigle C., et al., 2016, ApJS, 224, 24

Laporte N., et al., 2019, MNRAS, 487, L81

Lawrence A., et al., 2007, MNRAS, 379, 1599

Lee N., et al., 2010, ApJ, 717, 175

Lee M. M., et al., 2019, ApJL, 883, L29

Lemaître G., 1927, Annales de la Société Scientifique de Bruxelles, 47, 49

Leroy A. K., et al., 2011, ApJ, 737, 12

Lewis J. S. W., Ocvirk P., Dubois Y., Aubert D., Chardin J., Gillet N., Thélie É., 2023, MNRAS, 519, 5987

Li A., Draine B. T., 2001, ApJ, 554, 778

Li Q., et al., 2019, ApJ, 875, 130

Liang L., Feldmann R., Hayward C. C., Narayanan D., Çatmabacak O., Kereš D., Faucher-Giguère C.-A., Hopkins P. F., 2021, MNRAS, 502, 3210

Liu W., Jiang L., 2023, ApJ, 958, 187

Liu C., Gan Z.-M., Xie F.-G., 2013, RAA, 13, 899

Liu D., et al., 2019, ApJS, 244, 40

Loeb A., Barkana R., 2001, ARA&A, 39, 19

Lu N., et al., 2018, ApJ, 864, 38

Lutz D., et al., 2011, A&A, 532

MacTavish C. J., et al., 2006, ApJ, 647, 799

Madau P., Dickinson M., 2014, ARA&A, 52, 415

Maeda F., Ohta K., Seko A., 2017, ApJ, 835, 120

Magdis G. E., et al., 2012, ApJ, 760, 6

Magdis G. E., et al., 2017, A&A, 603, A93

Magnelli B., et al., 2014, A&A, 561, A86

Magnelli B., et al., 2020, ApJ, 892, 66

Magorrian J., et al., 1998, AJ, 115, 2285

Maiolino R., et al., 2005, A&A, 440, L51

Mallory K., Calzetti D., Lin Z., 2022, ApJ, 933, 156

Matthee J., Sobral D., Santos S., Röttgering H., Darvish B., Mobasher B., 2015, MNRAS, 451, 400

Matthee J., Sobral D., Oteo I., Best P., Smail I., Röttgering H., Paulino-Afonso A., 2016, MNRAS, 458, 449

Matthee J., et al., 2021, MNRAS, 505, 1382

McGaugh S. S., de Blok W. J. G., 1997, ApJ, 481, 689

McGreer I. D., Mesinger A., D'Odorico V., 2015, MNRAS, 447, 499

McKinnon R., Torrey P., Vogelsberger M., Hayward C. C., Marinacci F., 2017, MNRAS, 468, 1505

Melinder J., et al., 2023, ApJS, 266, 15

Mesinger A., 2010, MNRAS, 407, 1328

Mesinger A., Aykutalp A., Vanzella E., Pentericci L., Ferrara A., Dijkstra M., 2015, MNRAS, 446, 566

Meurer G. R., Heckman T. M., Calzetti D., 1999, ApJ, 521, 64

Miley G., De Breuck C., 2008, AAPR, 15, 67

Miralda-Escudé J., 2003, Science, 300, 1904

Molnár D. C., et al., 2018, MNRAS, 475, 827

Mondal C., Saha K., 2024, ApJ, 970, 80

Montier L. A., Giard M., 2004, A&A, 417, 401

Moore B., Katz N., Lake G., Dressler A., Oemler A., 1996, Nature, 379, 613

Morgan W. W., Keenan P. C., 1973, ARA&A, 11, 29

Mori M., Umemura M., 2006, Nature, 440, 644

Mountrichas G., Ruiz A., Georgantopoulos I., Pouliasis E., Akylas A., Drigga E., 2024, A&A, 688, A79

Moustakas J., Kennicutt Jr. R. C., Tremonti C. A., 2006, ApJ, 642, 775

Moustakas J., Kennicutt Jr. R. C., Tremonti C. A., Dale D. A., Smith J.-D. T., Calzetti D., 2010, ApJS, 190, 233

Muñoz J. B., Qin Y., Mesinger A., Murray S. G., Greig B., Mason C., 2022, MNRAS, 511, 3657

Muzzin A., et al., 2013, ApJ, 777, 18

Narayanan D., Krumholz M. R., Ostriker E. C., Hernquist L., 2012, MNRAS, 421, 3127

Narayanan D., Davé R., Johnson B. D., Thompson R., Conroy C., Geach J., 2018, MNRAS, 474, 1718

Navarro J. F., Frenk C. S., White S. D. M., 1997, ApJ, 490, 493

Netzer H., et al., 2007, ApJ, 666, 806

Neufeld D. A., 1991, ApJL, 370, L85

Neugebauer G., Oke J. B., Becklin E. E., Matthews K., 1979, ApJ, 230, 79

Nilsson K. K., et al., 2007, A&A, 471, 71

Ning Y., Cai Z., Jiang L., Lin X., Fu S., Spinoso D., 2023, ApJL, 944, L1

Noeske K. G., et al., 2007, ApJL, 660, L43

Nomoto K., Kobayashi C., Tominaga N., 2013, ARA&A, 51, 457

Oliver S. J., et al., 2012, MNRAS, 424, 1614

Osterbrock D. E., 1989, Astrophysics of gaseous nebulae and active galactic nuclei

Ota K., et al., 2014, ApJ, 792, 34

Ota K., et al., 2017, ApJ, 844, 85

Oteo I., et al., 2012, A&A, 541

Otí-Floranes H., Mas-Hesse J. M., Jiménez-Bailón E., Schaerer D., Hayes M., Östlin G., Atek H., Kunth D., 2012, A&A, 546, A65

Otí-Floranes H., Mas-Hesse J. M., Jiménez-Bailón E., Schaerer D., Hayes M., Östlin G., Atek H., Kunth D., 2014, A&A, 566, A38

Oyarzún G. A., Blanc G. A., González V., Mateo M., Bailey III J. I., 2017, ApJ, 843, 133

Padmanabhan T., 2005, Current Science, 88, 1057

Padovani P., et al., 2017, AAPR, 25, 2

Peebles P. J. E., 1968, ApJ, 153, 1

Peebles P. J. E., 1982, ApJL, 263, L1

Penzias A. A., Wilson R. W., 1965, ApJ, 142, 419

Perlmutter S., et al., 1998, Nature, 391, 51

Pettini M., Kellogg M., Steidel C. C., Dickinson M., Adelberger K. L., Giavalisco M., 1998, ApJ, 508, 539

Planck Collaboration et al., 2020, A&A, 641, A6

Polletta M., et al., 2007, ApJ, 663, 81

Popesso P., et al., 2012, arXiv e-prints, p. arXiv:1211.4257

Popesso P., et al., 2023, MNRAS, 519, 1526

Popping G., Puglisi A., Norman C. A., 2017, MNRAS, 472, 2315

Prandoni I., Seymour N., 2015,] 10.22323/1.215.0067, p. 67

Ramasawmy J., et al., 2022, in Zmuidzinas J., Gao J.-R., eds, Society of Photo-Optical Instrumentation Engineers (SPIE) Conference Series Vol. 12190, Millimeter, Submillimeter, and Far-Infrared Detectors and Instrumentation for Astronomy XI. p. 1219007 (`arXiv:2207.03914`), doi:10.1117/12.2627505

Reddy N. A., et al., 2015, ApJ, 806, 259

Reddy N. A., et al., 2018, ApJ, 853, 56

Rees M. J., 1999, in Holt S., Smith E., eds, American Institute of Physics Conference Series Vol. 470, After the Dark Ages: When Galaxies were Young (the Universe at 2 ¡ Z ¡ 5). AIP, pp 13–23, doi:10.1063/1.58643

Rhoads J. E., et al., 2004, ApJ, 611, 59

Riechers D. A., et al., 2013, Nature, 496, 329

Riess A. G., et al., 1998, AJ, 116, 1009

Riguccini L., et al., 2011, A&A, 534, A81

Roy N., et al., 2023, ApJL, 952, L14

Safarzadeh M., Hayward C. C., Ferguson H. C., 2017, ApJ, 840, 15

Saintonge A., Catinella B., 2022, ARA&A, 60, 319

Salpeter E. E., 1955, ApJ, 121, 161

Sanders D. B., et al., 2007, ApJS, 172, 86

Santini P., et al., 2014, A&A, 562, A30

Santos S., Sobral D., Matthee J., 2016, MNRAS, 463, 1678

Santos S., et al., 2020, MNRAS, 493, 141

Saxena A., et al., 2023, A&A, 678, A68

Scarlata C., et al., 2009, ApJL, 704, L98

Schawinski K., Thomas D., Sarzi M., Maraston C., Kaviraj S., Joo S.-J., Yi S. K., Silk J., 2007, MNRAS, 382, 1415

Schaye J., et al., 2010, MNRAS, 402, 1536

Schiminovich D., et al., 2007, ApJS, 173, 315

Scoville N., et al., 2007, ApJS, 172, 38

Scoville N., et al., 2014, ApJ, 783, 84

Scoville N., et al., 2016, ApJ, 820, 83

Scoville N., et al., 2023, ApJ, 943, 82

Shetty R., Kauffmann J., Schnee S., Goodman A. A., 2009, ApJ, 696, 676

Shibuya T., Kashikawa N., Ota K., Iye M., Ouchi M., Furusawa H., Shimasaku K., Hattori T., 2012, ApJ, 752, 114

Shirley R., et al., 2021, MNRAS, 507, 129

Silva L., Granato G. L., Bressan A., Danese L., 1998, ApJ, 509, 103

Silverman J. D., et al., 2015, ApJL, 812, L23

Simpson J. M., et al., 2019, ApJ, 880, 43

Slipher V. M., 1917, Proceedings of the American Philosophical Society, 56, 403

Smith A., et al., 2022, MNRAS, 517, 1

Smolčić V., et al., 2017, A&A, 602, A1

Sobral D., Matthee J., 2019, A&A, 623, A157

Sobral D., Santos S., Matthee J., Paulino-Afonso A., Ribeiro B., Calhau J., Khostovan A. A., 2018, MNRAS, 476, 4725

Solomon P. M., Vanden Bout P. A., 2005, ARA&A, 43, 677

Solomon P. M., Downes D., Radford S. J. E., 1992, ApJL, 398, L29

Speagle J. S., Steinhardt C. L., Capak P. L., Silverman J. D., 2014, ApJS, 214, 15

Springel V., et al., 2005, Nature, 435, 629

Stachniewicz S., Kutschera M., 2005, MNRAS, 362, 89

Stacy A., Bromm V., Lee A. T., 2016, MNRAS, 462, 1307

Strandet M. L., et al., 2017, ApJL, 842, L15

Sugimura K., Ricotti M., Park J., Garcia F. A. B., Yajima H., 2024, ApJ, 970, 14

Swinbank A. M., et al., 2005, MNRAS, 359, 401

Tacconi L. J., et al., 2010, Nature, 463, 781

Tacconi L. J., Genzel R., Sternberg A., 2020, ARA&A, 58, 157

Taniguchi Y., et al., 2015, PASJ, 67, 104

Tapken C., Appenzeller I., Noll S., Richling S., Heidt J., Meinköhn E., Mehlert D., 2007, A&A, 467, 63

Tegmark M., et al., 2004, PhysRevD, 69, 103501

Thielemann F.-K., Nomoto K., Hashimoto M.-A., 1996, ApJ, 460, 408

Tilvi V., et al., 2010, ApJ, 721, 1853

Toomre A., 1977, p. 401

Trainor R. F., Strom A. L., Steidel C. C., Rudie G. C., 2016, ApJ, 832, 171

Tremonti C. A., et al., 2004, ApJ, 613, 898

Umeda H., Ouchi M., Kageura Y., Harikane Y., Nakane M., Thai T. T., Nakajima K., 2025, arXiv e-prints, p. arXiv:2504.04683

Vale Asari N., et al., 2020, MNRAS, 498, 4205

Verhamme A., Orlitová I., Schaerer D., Izotov Y., Worseck G., Thuan T. X., Guseva N., 2017, A&A, 597, A13

Vogelsberger M., McKinnon R., O'Neil S., Marinacci F., Torrey P., Kannan R., 2019, MNRAS, 487, 4870

Wang S. X., et al., 2013, ApJ, 778

Wang T.-M., et al., 2022, A&A, 660, A142

Ward B. A., Eales S. A., Ivison R. J., Arumugam V., 2024, MNRAS, 530, 4887

Wardlow J. L., et al., 2014, ApJ, 787

Wardlow J. L., et al., 2018, MNRAS, 479, 3879

Watson D., Christensen L., Knudsen K. K., Richard J., Gallazzi A., Michałowski M. J., 2015, Nature, 519, 327

Weiss L. H., et al., 2021, ApJ, 912, 100

Werle A., et al., 2024, A&A, 682, A162

Whalen D., Hueckstaedt R. M., McConkie T. O., 2010, ApJ, 712, 101

White S. D. M., Rees M. J., 1978, MNRAS, 183, 341

White M., Scott D., Silk J., 1994, ARA&A, 32, 319

Wild V., et al., 2011, MNRAS, 410, 1593

Williams R. J., et al., 2014, MNRAS, 439, 2096

Williams C. C., et al., 2021, ApJ, 908, 54

Wilson T. L., Elbaz D., eds 2006, arXiv e-prints, pp astro–ph/0609311

Wise J. H., 2019, Contemporary Physics, 60, 145

Witstok J., et al., 2025, Nature, 639, 897

Wold I. G. B., et al., 2022, ApJ, 927, 36

Wolfire M. G., Hollenbach D., McKee C. F., 2010, ApJ, 716, 1191

Woosley S. E., Weaver T. A., 1995, ApJS, 101, 181

Woosley S. E., Heger A., Weaver T. A., 2002, Reviews of Modern Physics, 74, 1015

Wuyts S., et al., 2011, ApJ, 742, 96

Young J. S., Scoville N. Z., 1991, ARA&A, 29, 581

Zabludoff A. I., Franx M., 1993, AJ, 106, 1314

Zavagno A., et al., 2010, A&A, 518, L101

Zhang Z., Shi Y., Rieke G. H., Xia X., Wang Y., Sun B., Wan L., 2016, ApJL, 819, L27

Zhao R. J., Furlanetto S. R., 2024, JCAP, 2024, 018

Zhukovska S., Henning T., 2013, A&A, 555, A99

Zubovas K., Nayakshin S., King A., Wilkinson M., 2013, MNRAS, 433, 3079

da Cunha E., Charlot S., Elbaz D., 2008, MNRAS, 388, 1595